PURE SCIENCES
International Journal of Kerbala

Ministry of Higher Education
and Scientific Research
University of Kerbala
College of Education for Pure Sciences

Pure Sciences International Journal of Kerbala

PSIJK

Year:2025
Volume : 2
ISSUE : 8

ISSN: 2789-6188 Print
3005 -2394 Online

PURE
SCIENCES
International Journal of Kerbala

Pure Sciences International Journal of Kerbala

(PSIJK) is published in four issues annually

A quarterly peer-reviewed scientific journal issued by the College of Education for Pure Sciences at the University of Kerbala, specializing in pure sciences, accredited for the purposes of scientific promotion Pursuant to Ministerial Resolution No. **B.T 7575** Dated **14 /9 /2023**

Licensed by

Ministry of Higher Education
and Scientific Research and Scientific Research

Issued by

University of Kerbala
College of Education for Pure Sciences

2025 , Volume 2 , Issue 8
31 December 2025

Ministry of Higher Education and Scientific Research

College of Education for Pure Sciences

University of Kerbala

Print ISSN: 6188-2789

Online ISSN: 3005 -2394

Consignment Number in the Housebook and Iraqi

Documents: 2515, 2021

Postal Code: 56001

Mailbox: 232

Mobile: +964 7769920165

https://journals.uokerbala.edu.iq

Iraq - Holy Karbala

Workflow by OJS/PKP

About the Journal

The "Pure Sciences International Journal of Kerbala", published quarterly and distributed internationally by the College of Education for Pure Sciences provides a forum for publication of significant science advancements and developments in chemistry, biology, computer, physics, mathematics and interdisciplinary areas of science. All prospective authors are invited to submit their original contributions on new theoretical and applied aspects of growing research. All manuscripts submitted, including symposium papers, will be peer reviewed by qualified scholars assigned by the editorial board.

You are cordially encouraged to use this journal as a means of dissemination of information on the various facets of science and technical problems; and to impart specialized knowledge, quality and excellence to strengthen the perception of technological resources and needs of the world. The PSIJK is looking forward to receiving your assistance to working together to develop a worthwhile, high quality journal.

Aims and Scope

Pure Sciences International Journal of Kerbala is an open-access, interdisciplinary, single-blind peer-reviewed journal that consolidates research activities in the experimental and theoretical aspects of modern sciences. The journal aims to make significant contributions to applied research and knowledge globally through the publication of original high-quality research papers and review articles on recent advances and frontier achievements in Biology, Mathematics, Chemistry, Physics, and Computer Science, as well as their related and subfields.

Scope of Research

The journal encompasses both fundamental and applied investigations across a wide range of interdisciplinary topics. Articles of an interdisciplinary nature are particularly welcome. Any paper reporting scientifically accurate and valuable research that adheres to accepted ethical and scientific publishing standards will be considered for publication.

Publication Ethics

Pure Sciences International Journal of Kerbala is committed to upholding the highest standards of publication ethics. We adhere to the principles and policies outlined by the Committee on Publication Ethics (COPE).

Duties of Editors

- Editors have full authority to reject or accept manuscripts.
- Editors maintain the confidentiality of submitted manuscripts under review until they are published.
- Editors preserve the anonymity of reviewers.
- Editors disclose and try to avoid any conflict of interest.
- Editors comment on ethical questions and possible misconduct raised by submissions.

Duties of Reviewers

- Reviewers assist the editorial board in making editorial decisions.
- Reviews should be conducted objectively, and observations should be formulated clearly with supporting arguments.
- Reviewers should not consider manuscripts in which they have conflicts of interest.
- Reviewers should treat the manuscript as a confidential document.

Duties of Authors

- The submitted manuscript should not be submitted to more than one journal for simultaneous consideration.
- The submitted work should be original and should not have been published elsewhere.
- Authors should adhere to discipline-specific rules for acquiring, selecting, and processing data.
- Authors should properly cite all content referenced from other materials.

Research Involving Humans, Animals, and Plants

- Research involving humans must be conducted in accordance with the Declaration of Helsinki.
- Research involving animals must adhere to international, national, and institutional guidelines for the humane treatment of animals.
- Studies on plants must be carried out within the guidelines provided by the authors› institution and national or international regulations.

Consent for Publication

- Written informed consent must be obtained from individuals who are featured in the manuscript.
- The consent form must state that the details/images will be freely available on the internet.

Fundamental Errors in Published Works

- Authors are obligated to promptly notify the journal editor of any significant errors or inaccuracies in the published work.

Plagiarism

- Plagiarism in any form constitutes a serious violation of publication ethics and is not acceptable.
- All submitted manuscripts are checked for plagiarism using professional plagiarism-checking software.

Complaints/Appeals

- All complaints, concerns, or appeals regarding authorship issues or the peer-review process should be addressed to the Editor-in-Chief.

Conflicts of Interest/Competing Interests

- Authors must disclose any conflicts of interest they may have with the publication of the manuscript.

Confidentiality

- A submitted manuscript is a confidential material.
- The journal will not disclose submitted manuscripts to anyone except individuals who partake in the processing and preparation of the manuscript for publication.

Misconduct

- Misconduct constitutes a violation of this editorial policy, journal policies, publication ethics, or any applicable guidelines/policies specified by COPE, WAME, and ICMJE.

Correction and Retraction of Articles

- Corrections may be made to a published article with the authorization of the editor of the journal.
- When necessary, the retraction of articles will be done according to COPE retraction guidelines.

Acknowledgment

- Individuals who participated in the development of a manuscript but do not qualify as an author should be acknowledged.
- Organizations that provided support in terms of funding and/or other resources should also be acknowledged.

Editorial board

PURE SCIENCES
International Journal of Kerbala

Pure Sciences International Journal of Kerbala

Year: 2025 Volume : 2 Issue : 8 ISSN: 6188-2789 Print 3005 -2394 Online

2025,Volume 2 , Issue 8 , PSIJK (10-15)

Pure Sciences International Journal of Kerbala

Natural Radioactivity Levels in Tap and Bottled Water Samples for Some Primary Schools of Karbala Governorate, Iraq

Hayder J. Musa [a]*, Adil J. Najim [a], Abbas J. Al-Saadi [a]

[a] *Department of Physics, College of Education for Pure Sciences, University of Kerbala, Karbala, Iraq*

P A P E R I N F O

Received: 12.09.2025
Accepted: 16.11.2025
Published: 31.12.2025

Keywords:
Natural radioactivity, Activity concentration, Radiological hazards, Gamma spectrometry, tap water, primary schools.

A b s t r a c t

Natural radioactivity levels of ^{226}Ra, ^{232}Th, and ^{40}K were assessed in 10 tap water samples collected from different schools in Karbala govenorate, as well as 5 commercial bottled drinking water samples. The activity concentrations were measured using gamma spectrometry with a NaI(Tl) 3"×3" detector equipped with a specially designed shield. In tap water samples, the activity concentrations of ^{226}Ra, ^{232}Th, and ^{40}K ranged from <0.063 to 0.817, <0.067 to 0.493, and <0.117 to 9.896 Bq·L^{-1}, respectively. For bottled water, ^{226}Ra and ^{232}Th concentrations were below the Minimum Detectable Actictivity (MDA), while ^{40}K ranged from <0.117 to 8.180 Bq·L^{-1}. Overall, tap water samples exhibited higher concentrations than bottled water. The measured values for tap water were within the ranges reported in the literature for other countries. Health implications were estimated by calculating the annual effective dose received by school-age children due to ingestion of radionuclides. The average values of annual effective dose in tap and bottled water were 85.05 and 36.40 μSv·y^{-1} respectively. All calculated doses were below the global mean level of 100 μSv·y^{-1}, as reported by World Health Organization (WHO). It is therefore concluded that both tap water and bottled water consumed in schools of Karbala Governorate are radiologically safe and pose no significant health hazard to the public.

DOI: 10.53851/psijk.v2i8.10-15

1. INTRODUCTION

Both natural and man-made radionuclides can be found in drinking water. Because of natural processes (like soil absorption) or technological activities involving naturally occurring radioactive materials (like mineral sand mining and phosphate fertilizer production), water may contain natural radionuclides like potassium-40 and those from the thorium and uranium decay series. Water from a variety of sources, including those produced and used in industrial or medical settings, may contain anthropogenic radionuclides (WHO, 2008). Radium is known to cause cancer. High levels of radium exposure can raise the risk of breast, liver, and bone cancer. Because of their similar behavior to that of calcium, an element commonly deposited in bones, radium isotopes (^{226}Ra) have a long half-life (~1600 years) and they are the most radiotoxic and dangerous elements when consumed. The natural radioactive decay series of thorium is initiated by ^{232}Th ($T_{1/2} = 1.4 \times 10^{10}$ y), which is found in the Earth's crust. Although they come from different sources, both radionuclides (^{226}Ra and ^{232}Th) are present in terrestrial materials. They are taken out of rocks, soils, and water by leaching or erosion. With a half-life of 1.25×10^{9} y, potassium-40 (^{40}K) is a radioactive isotope of potassium. About 0.012% (120 ppm) of the total potassium found in nature is made up of it. Like other potassium isotopes, the potassium radioisotope ^{40}K has a similar physiological effect. Humans require potassium to sustain biological

*Corresponding Author Institutional Email:
hayder.jasim@uokerbala.edu.iq (Hayder J. Musa)

processes, and most of it (including ^{40}K) is absorbed almost completely when consumed, moving quickly from the stomach into the blood. All organs and tissues quickly absorb the ^{40}K that enters the bloodstream after ingestion or inhalation (Brenner et al., 2003) (Tolstykh et al., 2016) (Altıkulaç et al., 2015). Radiation has a long-lasting effect on the environment, possibly changing the genetic makeup of animals and humans, leading to cellular death and genetic defects that appear in subsequent generations. Radiation's most direct effect on cells is especially dangerous when it causes the death of the body's irreplaceable cells. The foundation of radiation protection is the idea that all radiation exposures carry some level of risk. Long-term exposure, such as consuming drinking water contaminated with radionuclides for extended periods of time, has been linked to an increased risk of cancer in humans at doses greater than 100 mSv (Brenner et al., 2003) (ICRP, 1996). Therefore, radioactive material surveillance is essential for human safety and has been studied in various parts of the world (Abbasi & Bashiry, 2016) (Kinahan et al., 2020) (Al-Shammari et al., 2025) (Qwasmeh & Saleh, 2023). The purpose of this study is to assess the levels of natural radioactivity and the corresponding yearly effective dose of tap and bottled drinking water in a few Karbala Governorate schools. The dearth of information on Karbala's drinking water's radioactivity, which is necessary to guarantee that the annual effective dose and specific activity for drinking water stay within advised bounds, makes this study noteworthy.

2. MATERIALS AND METHODS

2.1. STUDY AREA

Approximately 100 kilometers southwest of Baghdad, in central-southern Iraq, the Karbala Governorate borders the Anbar, Najaf, and Babil governorates. It is situated at roughly 32°27′N, 43°48′E, and is around 30 meters above sea level. Three districts—Karbala Center, Al-Hindiyah, and Ain Al-Tamur—make up the administrative division of the Karbala Governorate. The governorate was estimated to have 1,316,750 residents in 2021, with about 880,400 of them residing in urban areas, according to the Iraqi Central Statistical Organization (CSO).

2.2. SAMPLE COLLECTION AND PREPARATION

The study included 10 tap water samples, sourced from local municipal networks, which were collected in May 2023 from schools distributed across the districts of Karbala Governorate, namely the Karbala district center, Ain Al-Tamur, and Al-Hindiya. We also collected five samples of commercially bottled drinking water. The water samples were used in measurement standard (1L) polyethylene Marinelli beakers. Before using them, the containers were washed with dilute hydrochloric acid and rinsed with distilled water. Each drinking water sample was hermetically sealed and stored for a minimum of four weeks to ensure that secular radioactive equilibrium was reached between ^{226}Ra with ^{222}Rn and its progeny (IAEA, 2003) (Sabbarese et al., 2021). Table (1) shows the coordinates of the schools from which tap water samples were collected, while Table (2) presents the locations of the water bottling plants that were chosen.

2.3. EXPERIMENTAL SETUP

Natural radioactivity measurements and sample preparation were carried out at the University of Kerbala's Nuclear Laboratory, Department of Physics, College of Education for Pure Sciences. A gamma-ray spectrometer fitted with a NaI(Tl) 3"×3" detector contained in a specially made lead shield to reduce background radiation was used to analyze each sample. The detector's energy resolution at the 1.33 MeV gamma line of ^{60}Co was 63 keV (FWHM). Lead that was more than 10 cm thick and lined inside with 1.5 mm of cadmium and 2.5 mm of copper made up the shielding system. Standard radionuclides (^{22}Na, ^{152}Eu, ^{137}Cs, and ^{60}Co) were used to calibrate detector efficiency for each photopeak energy. Maestro software (EG&G ORTEC) was used to analyze the spectra. Figure 1 displays the efficiency curve as a function of gamma-ray energy. An exponential fit is represented by the solid line, which has a correlation coefficient of $R^2 = 0.972$.

Table 1. School name, sample number and coordinate for tap water samples.

School name and location	Sample number	Coordinates	
		Latitude (N)	Longitude (E)
Zahrat Al-Furat, Karbala district center	TW1	32°36'22.9"	43°59'06.8"
Amerli, Karbala district center	TW2	32°33'24.0"	44°04'28.4"
Al-Makasib, Karbala district center	TW3	32°36'42.6"	44°00'39.5"
Al-Riahi, Karbala district center	TW4	32°39'05.0"	43°58'33.9"
Saif Al- Haq, Karbala district center	TW5	32°41'25.9"	44°06'51.8"
Al AJyal, Karbala district center	TW6	32°40'41.5"	44°04'35.1"
AL Waha Algathra, Ain Al-Tamur	TW7	32°45'54.0"	43°23'20.4"
Al-Rashad, Ain Al-Tamur	TW8	32°35'28.0"	43°29'29.9"
Al-Furat, Al-Hindiya	TW9	32°32'52.6"	44°13'08.0"
Almaearif, Al-Hindiya	TW10	32°32'48.7"	44°14'04.8"

Table 2. Plant name, sample number and water bottling plants location.

Plant name	Sample number	Coordinates	
		Latitude (N)	Longitude (E)
Alkafeel	BW1	32°36'15.4"	44°07'16.3"
Nawar	BW2	32°36'31.9"	44°06'59.7"
Loloa	BW3	32°35'31.2"	44°02'47.8"
Seha	BW4	32°32'23.6"	44°30'40.9"
Barakat Alwareth	BW5	32°32'21.3"	44°05'41.5"

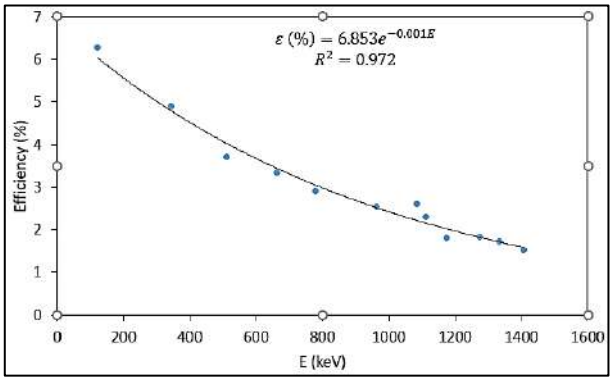

Figure 1. Detection efficiency of NaI(Tl) Gamma spectrometry system.

2.4. THE ACTIVITY CONCENTRATION

The net counts were derived by estimating the photopeak regions in the spectra and adjusting for background counts post-measurement. The subsequent formula was employed to determine the activity concentration (A) of the radionuclides [12,13]:

$$A\left(\frac{Bq}{L}\right) = \frac{C_N}{\varepsilon(E\gamma)\,.\,I\gamma(E\gamma).V.T_c} \quad \ldots\ldots\ldots(1)$$

where: C_N is the is the net counts in a given peak area, I_γ (E_γ) is the emission probability of the measuring γ-rays with the given energy; ε (E_γ) is the full-energy peak efficiency; V is the volume of water sample and; T_c is the counting time. Activity concentrations of ^{226}Ra and ^{232}Th were determined using the gamma-ray peak at 1764.49 keV from ^{214}Bi and that at 2614.53 keV from ^{208}Tl, respectively. Direct determination of the activity concentration of ^{40}K was made using the 1460.7 keV gamma emission line (Parhoudeh et al., 2019) (Currie, 1968). Every sample had a counting time of 21,600 seconds.

When measuring low-level activity, the Minimum Detectable Activity (MDA) is a crucial parameter. The following formula (Abdel-Rahman & El-Mongy, 2017) (Currie, 1968) was used to determine the MDA of the gamma-ray measurements:

$$MDA\left(\frac{Bq}{L}\right) = \frac{\text{LLD}}{\varepsilon(E\gamma)\,.\,I\gamma(E\gamma).V.Tc} \quad \ldots\ldots\ldots(2)$$

where LLD is the lower limit of detection, as defined below (Currie, 1968) (Abdel-Rahman & El-Mongy, 2017):

$$LLD(count) = 2.71 + 4.65\sqrt{B} \quad \ldots\ldots\ldots(3)$$

where B is the number of counts for the background spectrum. Under identical circumstances, including counting time and measurement geometry, the MDA of every radionuclide was computed from the background spectrum. ^{226}Ra, ^{232}Th, and ^{40}K were found to have MDA values of 0.063, 0.067, and 0.117 Bq·L^{-1}, respectively.

2.5. RADIATION DOSE FOR DRINKING WATER

The rate at which food and water are consumed, as well as the concentrations of radionuclides in these media, determine the ingestion dose. To assess the possible radiological risks to the general public, especially children, the Annual Effective Dose from Drinking Water (AED) was calculated. The following formula (ICRP, 1996) (UNSCEAR, 2000)was used to determine the AED (Sv·y^{-1}) using the radionuclide activity concentrations, dose conversion coefficients, and annual water consumption:

$$AED\ (Sv.y^{-1}) = A \times DCF \times CR_W \quad \ldots\ldots\ldots(4)$$

where A (Bq·L^{-1}) is the activity concentration of the radionuclides (^{226}Ra, ^{232}Th and ^{40}K), DCF is the dose conversion factors 2.8 × 10^{-7}, 2.2 ×10^{-7} and 2.1× 10^{-8} Sv·Bq^{-1} for ^{226}Ra, ^{232}Th and ^{40}K respectively. CR_w is the annual consumption rate of drinking water 350 L·y^{-1} for children aged 10 years.

3. RESULTS AND DISCUSSION

3.1. RADIONUCLIDES ACTIVITY CONCENTRATION

Table 3 displays the activity concentrations of ^{226}Ra, ^{232}Th, and ^{40}K that were determined in the drinking water samples. It is evident that the MDA value (0.063 Bq·L^{-1}) was exceeded by the concentration of ^{226}Ra in four tap water samples (TW3, TW6, TW9, and TW10). They generally ranged from <0.063 to 0.817 Bq·L^{-1}. While the concentrations of ^{226}Ra in all bottled water samples were below the MDA. The ^{232}Th concentrations in tap water samples were ranged from <0.067 to 0.493 Bq·L^{-1}. In a similar vein, all bottled water samples had ^{232}Th concentrations below the MDA. The ^{40}K concentrations in tap water samples were ranged fom ~0.117 to 9.896 Bq·L^{-1}. While the concentrations of ^{40}K in bottled water were ranged from

three samples had of which is below the MDA for ^{40}K. The concentrations of ^{40}K in bottled water were ranged from <0.117 to 8.180 Bq·L^{-1}. Additionally, the BW1 sample (Alkafel bottled water) had activity concentrations of ^{226}Ra, ^{232}Th, and ^{40}K that were all below the corresponding MDA values.

Table 3. Activity concentration of natural radionuclides (Bq·L^{-1}) in tap water (TW) samples from schools and commercial bottled water (BW) in Karbala Governorate.

Sample number	Activity Concentration (Bq L^{-1})		
	^{226}Ra	^{232}Th	^{40}K
TW1	0.610	0.493	< MDA
TW2	0.817	0.313	< MDA
TW3	< MDA	< MDA	9.896
TW4	0.729	< MDA	8.643
TW5	0.453	0.253	< MDA
TW6	< MDA	< MDA	7.992
TW7	0.481	0.143	9.194
TW8	0.488	0.387	1.828
TW9	< MDA	0.281	7.545
TW10	< MDA	0.191	1.323
Commercial bottled water(BW)			
BW1	< MDA	< MDA	< MDA
BW2	< MDA	< MDA	7.311
BW3	< MDA	< MDA	1.462
BW4	< MDA	< MDA	8.180
BW5	< MDA	< MDA	7.814

Table 4 summarizes the comparison between the measured activity concentrations of the natural radionuclides and data reported globally. The activity concentrations of ^{226}Ra, ^{232}Th and ^{40}K were significantly lower than the 1, 1 and 10 Bq·L^{-1} WHO guidance levels, respectively (WHO, 2017). The activity concentrations of ^{226}Ra, ^{232}Th and ^{40}K measured in drinking water are generally in line with those reported in Saudi Arabia (Jeddah), Turkey, Kermanshah (Iran), Serbia and Kosovo.

Table 4. Comparison of the activity concentrations and annual effective doses in several countries with our findings in drinking water samples from schools in Karbala Governorate, Iraq.

Countries		Activity Concentration (Bq·L^{-1})			AED (μSv·y^{-1})
		^{226}Ra	^{232}Th	^{40}K	
Saudi Arabia (Jeddah)[b] (Al-Ghamdi, 2017)		0.77	1.3	11.1	400
Turkey[b] (Kabadayi & Gümüş, 2012)		0.78	1.05	2.19	---
Serbia[s] (Tanaskovic et al., 2011)		0.17	---	0.46	
Kermanshah (Iran)[d] (Parhoudeh et al., 2019)		0.57	0.98	6.42	150
Kosovo (Hodolli et al., 2025)		0.65[t] 0.98[w] 0.81[b]	0.55 0.63 0.56	6.68 7.46 5.40	110
This study	Tap water	0.357	0.206	4.642	85.05
	Bottled water	< MDA	< MDA	4.953	36.40

[b]bottled, [s]spring, [w]well, [d]drinking, [t]tap.

3.2. ANNUAL EFFECTIVE DOSE

The Annual Effective Dose (AED) is the amount that is frequently used to calculate population exposure to terrestrial radionuclides. Table 5 lists the annual effective doses that school-age children in Karbala schools receive from drinking water that contains ^{226}Ra, ^{232}Th, and ^{40}K. The total annual effective doses (AED) caused by ^{226}Ra, ^{232}Th, and ^{40}K in tap water varied from 24.43 to 134.96 μSv·y^{-1}, with an average of 85.05 μSv·y^{-1}. As illustrated in Figure 2, the total AED for bottled water samples varied between 10.74 and 60.12 μSv·y^{-1}, with an average of 36.40 μSv·y^{-1}. Compared to bottled water, tap water had a higher total AED. In bottled drinking water, the AEDs from ^{226}Ra and ^{232}Th were below the lowest levels that could be detected. The average ADE in this study is lower than that reported in some countries (Table 4) and falls below the global average of 100 μSv·y^{-1} of drinking water consumption as established by (WHO, 2017)

Table 5. Annual effective doses (μSv/y) due to ingestion of natural radionuclides in tap water samples collected from Karbala schools.

Sample number	Annual effective doses (μSv·y^{-1})			
	^{226}Ra	^{232}Th	^{40}K	Total
TW1	59.78	37.96	---	97.44
TW2	80.06	24.10	---	104.12
TW3	---	---	72.74	72.74
TW4	71.44	---	63.53	134.96
TW5	44.39	19.48	---	63.87
TW6	---	---	58.74	58.74
TW7	47.14	11.01	67.58	125.72
TW8	47.82	29.80	13.44	91.06
TW9	---	21.64	55.46	77.09
TW10	---	11.71	9.72	24.43
Average	35.06	15.87	34.12	85.05
Commercial bottled drinking water (BW)				
BW1	---	---	---	---
BW2	---	---	53.73	53.73
BW3	---	---	10.74	10.74
BW4	---	---	60.12	60.12
BW5	---	---	57.43	57.43
Average	---	---	36.40	36.40

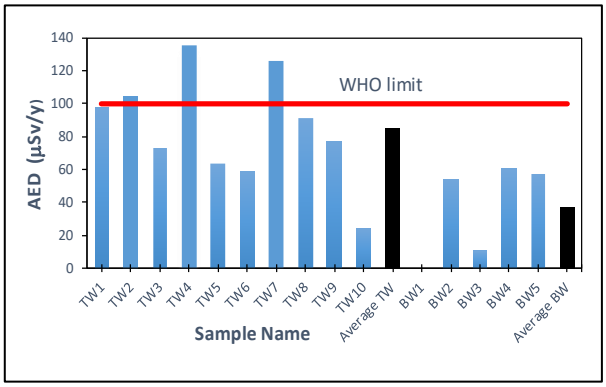

Figure 2. Annual effective doses received by children due to the ingestion of radionuclides ^{226}Ra, ^{232}Th, and ^{40}K in tap water and commercial bottled water samples with standard value reported by WHO.

4. CONCLUSIONS

In Karbala Governorate schools, the levels of radioactivity in drinking water caused by ^{226}Ra, ^{232}Th, and ^{40}K were found to be below WHO guidance levels and within the range of activity concentrations reported globally. Nevertheless, compared to bottled water samples, tap water samples had greater radionuclide concentrations. Additionally, the annual effective doses of these radionuclides received by children in Karbala were lower than the global average level (WHO) 100 $\mu Sv \cdot y^{-1}$ (WHO, 2017). It is determined that there is no substantial risk to the public from either tap or bottled water in Karbala Governorate schools. The baseline radiometric values for tap and bottled drinking water in the Karbala Governorate are provided by the data produced by this study. These values could be used as a guide for future research and help create national standards for natural radionuclides and annual effective doses in drinking water.

REFERENCES

Abbasi, A., & Bashiry, V. (2016). Measurement of radium-226 concentration and dose calculation of drinking water samples in Guilan province of Iran. *International Journal of Radiation Research*, *14*(4), 361–366. http://dx.doi.org/10.18869/acadpub.ijrr.14.4.361

Abdel-Rahman, M. A. E., & El-Mongy, S. A. (2017). Analysis of radioactivity levels and hazard assessment of black sand samples from Rashid area, Egypt. *Nuclear Engineering and Technology*, *49*(8), 1752–1757.https://doi.org/10.1016/j.net.2017.07.020

Al-Ghamdi, A. H. (2017). Activity concentrations in bottled drinking water in Saudi Arabia and consequent dose estimates. *New Trends and Issues Proceedings on Advances in Pure and Applied Sciences*, (9), 30–37. https://doi.org/10.18844/gjapas.v0i9.3014

Al-Shammari, H. F., Al-Jarba, M. A., Al-Shammeri, J. M., Al-Ateeqi, S., Ismaeel, A., & Al-Boloushi, A. (2025). Risk assessment of gross alpha–beta activity concentration in drinking water in Kuwait: Baseline measurements and review. *Environmental Monitoring and Assessment*, *197*(4), 1–12. https://doi.org/10.1007/s10661-025-13847-4

Altıkulaç, A., Turhan, Ş., & Gümüş, H. (2015). The natural and artificial radionuclides in drinking water samples and consequent population doses. *Journal of Radiation Research and Applied Sciences*, *8*(4), 578–582. https://doi.org/10.1016/j.jrras.2015.06.007

Brenner, D. J., Doll, R., Goodhead, D. T., Hall, E. J., Land, C. E., Little, J. B., Lubin, J. H., Preston, D. L., Preston, R. J., & Puskin, J. S. (2003). Cancer risks attributable to low doses of ionizing radiation: Assessing what we really know. *Proceedings of the National Academy of Sciences*, *100*(24), 13761–13766. https://doi.org/10.1073/pnas.2235592100

Currie, L. A. (1968). Limits for qualitative detection and quantitative determination: Application to radiochemistry. *Analytical Chemistry*, *40*(3), 586–593. https://pubs.acs.org/doi/10.1021/ac60259a007

Hodolli, G., Dizman, S., Kadiri, S., Makolli, S., & Kastrati, L. (2025). Natural radionuclides in drinking water and annual effective dose to infant, child, and adult. *Journal of Water and Health*, *23*(3), 373–383. https://doi.org/10.2166/wh.2025.316

International Atomic Energy Agency. (2003). *Collection and preparation of bottom sediment samples for analysis of radionuclides and trace elements*. IAEA.

International Commission on Radiological Protection. (1996). *Age-dependent doses to members of the public from intake of radionuclides: Part 5 compilation of ingestion and inhalation dose coefficients* (ICRP Publication 72). Annals of the ICRP.

Kabadayi, Ö., & Gümüş, H. (2012). Natural activity concentrations in bottled drinking water and consequent doses. *Radiation Protection Dosimetry*, *150*(4), 532–535. https://doi.org/10.1093/rpd/ncr430

Kinahan, A., Hosoda, M., Kelleher, K., Tsujiguchi, T., Akata, N., Tokonami, S., Currivan, L., & León Vintró, L. (2020). Assessment of radiation dose from the consumption of bottled drinking water in Japan. *International Journal of Environmental Research and Public Health*, *17*(14), Article 4992. https://doi.org/10.3390/ijerph17144992

Parhoudeh, M., Khoshgard, K., Zare, M. R., & Ebrahiminia, A. (2019). Natural radioactivity level of 226Ra, 232Th, and 40K radionuclides in drinking water of residential areas in Kermanshah province, Iran using gamma spectroscopy. *Iranian Journal of Medical Physics*, *16*(1), 98–102.

https://doi.org/10.22038/ijmp.2018.30012.1332

Qwasmeh, A. A. H., & Saleh, B. A. A. (2023). Radiation dose and lifetime risk for radiation-induced cancer due to natural radioactivity in tap water from Jordan. *Radiation and Environmental Biophysics*, *62*(2), 279–285. https://doi.org/10.1007/s00411-023-01018-3

Sabbarese, C., Ambrosino, F., D'Onofrio, A., & Roca, V. (2021). Radiological characterization of natural building materials from the Campania region (Southern Italy). *Construction and Building Materials*, *268*, Article 121087. https://doi.org/10.1016/j.conbuildmat.2020.121087

Tanaskovic, I., Eremic Savkovic, M., & Javorina, L. (2011). Radioactivity of spa waters in Serbia. *Proceedings of the XXVI Symposium of Radiation Protection Society of Serbia and Montenegro*, 133–136.

Tolstykh, E. I., Degteva, M. O., Bougrov, N. G., & Napier, B. A. (2016). Body potassium content and radiation dose from 40K for the urals population (Russia). *PLOS ONE*, *11*(4), Article e0154266. https://doi.org/10.1371/journal.pone.0154266

United Nations Scientific Committee on the Effects of Atomic Radiation. (2000). *Sources and effects of ionizing radiation*. United Nations.

World Health Organization. (2008). *Guidelines for drinking-water quality* (3rd ed.). WHO.

World Health Organization. (2017). *Guidelines for drinking-water quality* (4th ed.). WHO.

PURE SCIENCES
International Journal of Kerbala

Pure Sciences International Journal of Kerbala

Year: 2025 Volume : 2 Issue : 8 ISSN: 6188-2789 Print 3005 -2394 Online

2025,Volume 2 , Issue 8 , PSIJK (16-27)

Pure Sciences International Journal of Kerbala

Sensing Aspects of Hybrid SERS Sensors HO-Si Pillars and SiQDs Integrated with Gold Nanoparticles: A Comparative Study

Hind Kh. Abbas [a*], Ali F. Al-Rawaf [a], Alwan M. Alwan [b]

[a] *Department of Physics, College of Education for Pure Science, University of Kerbela, Karbala-Iraq*
[b] *School of Applied Science, University of Technology, Baghdad-Iraq*

P A P E R I N F O

Received: 07.10.2025
Accepted: 27.10.2025
Published: 31.12.2025

Keywords:
SERS sensor, silicon nanostructures, laser induced etching

A b s t r a c t

Two types of hybrid SERS sensors, have been synthesized through integrated Au nanoparticles on horizontal oriented (HO)-Si pillars and Silicon quantum dots (SiQDs) nanostructures substrates . Aggressive Laser-induced etching process ; at high laser intensity of 450, and 550 mW/cm2 and 405 nm wavelength, was used to create the HO-Si pillars and SiQDs substrates respectively . The hybrid SERS sensors have been synthesized with simple, easy – to- work and very low cost dipping technique of HO-Si pillars and SiQDs based-substrates in HAuCl4 solution. The growth mechanism of Au nanoparticles has shown clear depending on the morphology of the based- substrate. In the case of HO-Si pillars, the creation of Au nanoparticles essentially happened at the surface of Si substrate rather than the surface boundaries of HO-Si pillars, whereas with using SiQDs substrate, the deposition of Au nanoparticles mostly occurred around the SiQDs substrate. The better performance of hybrid SERS sensor of higher development factor, with minimum LOD and outstanding reproducibility has been attained for SiQDs sensor rather than that of HO-Si pillars sensor of about (7.46 × 108) , (9*10 -14 M) and (4%), respectively.

DOI: 10.53851/psijk.v2.i8.16-27

1. INTRODUCTION

Silicon nanostructures and their different types (vertical and horizontal silicon pillars , silicon quantum dots and nanowires) are among the basic elements of high importance in the manufactures of different types of hybrid sensors, because of its great specific surface area and extraordinary propensity to react with various kinds of chemical elements (Canham, L. T. 1990, Alwan, A. M. 2008). The plasmonics characteristics of the Au nanoparticles , like the resonance frequency of surface Plasmon and enormous Raman scattering cross section of distinct Au nanoparticles create them as a correct candidates for chemical molecular category through using the SERS process in hybrid structures sensors (Wali, L. A. 2023, Naseef, I. A. 2019), so the creation of hybrid SERS sensors with Au nanostructures has been an vigorous research capacity owing to their exceptional optical properties, which intensely count on dimensions, form and composition (Cheng, X. Y. 2015, Rashid, R. B. 2022, Chalhoub, A. E. 2011, Alwan, M. A. 2007, Ershov, I. A. 2020). Silicon nanostructures were synthesized by a different wet etching process , like laser ablation in liquid , metal boosted chemical etching pathway , laser pyrolysis and Laser-induced etching process (Jubair, D. S. 2021). The latter preparation method is characterized by its simplicity , low cost and the ability to control the specifications of the resulting nanostructures layer by

*Corresponding Author Institutional Email:
hind.khab@uokerbala.edu.iq (Hind Khudheyer Abbas)

controlling the intensity of the laser beam in addition to the irradiation period of the laser beam (Dheyab, A. B. 2019, Kumar, V. 2013, Alwan, A. M. 2018, He, Y. 2019, Ali, W. H. 2020, Zhang, Y. 2005). An aggressive Si etching path with assisting laser beam is a tedious process to dissolve Si happen in high laser intensity at temperatures above ambient temperatures. In this etching path, two phenomenon happen, the first one is to remove the Si nanoparticles layer formed by surface etched to form colloidal nanostructures. While , the second process is that increase the temperature to an active degree leads to a decrease in the surface tension of etching solution (Alwan, A. M. 2017). This results in the removed Si nanostructures layer reverting back to the precipitate on the etched zone (Liu, L. R. 2019). In basic idea , the route of aggressive engraving is very close for laser pyrolysis pathway in terms of using a pulsed or continuous laser beam, as a heating source, to precipitate many elements (Wail, H. A. 2018). High laser intensity and focusing ability of the laser beam is embodied in the efficient tuning of variable dimensions of nanostructures (Liu, Y. N. 2018). This technology is based on high temperature substrate, where heat buildup helps the nanostructures to be deposited (Alwan, A. M. 2018). The use of the enhanced etching technique with a high-intensity laser beam accompanied by a high temperature in the production of unique nanostructures such as SiQDs and Ho si pillar as a function of the laser beam intensity and temperature was studied extensively (Hamoudi, W. K. 2020). And they reached distinguished results, where there was a fundamental change in the morphology and structural properties of the resulting nanostructures with increasing the intensity of the laser beam. For Giorgis et al , they fabricate and explore the characteristics of various types of hybrid structures sensors through integrating different noble metals, like Pt, Ag, and Au on vertically aligned Si nano-wires (VO-Si NWs) (Giorgis, F. 2008). Naseef et al, they synthesized (VO-Si NWs) via metal-boosted chemical etching pathway through employing silver nanoparticles as a catalyst and the VO-Si NWs layer was used as room temperature gas sensors (Naseef, I. A. 2017). In the current study , the role of the Silicon nanostructures type (HO-Si pillars and SiQDs) which is on the formation and performance of HO-Si pillars and SiQDs / Au nanoparticle hybrid SERS sensors have been studied based on the plasmonics features of the Au nanoparticles which is synthesized via gold ions reduction process. The main objective of this study is develop an efficient hybrid SERS sensor with higher development factor, with minimum LOD and reproducibility.

2 .EXPERIMENTAL WORK

2.1 Preparation of Si HO-Si pillars and SiQDs nanostructures substrates .

To obtain HO-Si pillars and SiQDs nanostructures substrates, a resistivity (100 Ω.cm), mono-crystalline (100), n-type Si wafer, was employed as substrate for an aggressive Laser-induced etching process. The etching condition involving a solution consist of a mixtutre of HF and high purity ethanol with a mixing ratio of (1 HF 48% :4 C2H5OH 99.99%), 19 min etching time, 55mA/cm2 etching current density and the temperatures varies with the laser illumination intensity . The aggressive Laser-induced etching process, involving using high laser intensity of 450, and 550 mW/cm2 of 405 nm wavelength, to create the HO-Si pillars and SiQDs nanostructures substrates respectively.

A schematic illustration of the etching process is shown in Fig. 1. The temperature at the irradiated area as a result of laser-substrate interaction process is measured using digital laser probe thermometer type (Lutron250). Later the etching process, the HO-Si pillars and SiQDs substrates was stored in high purity 99.9% methanol in order to prevent the occurrence of SiO2 layer over the synthesized nanostructures.

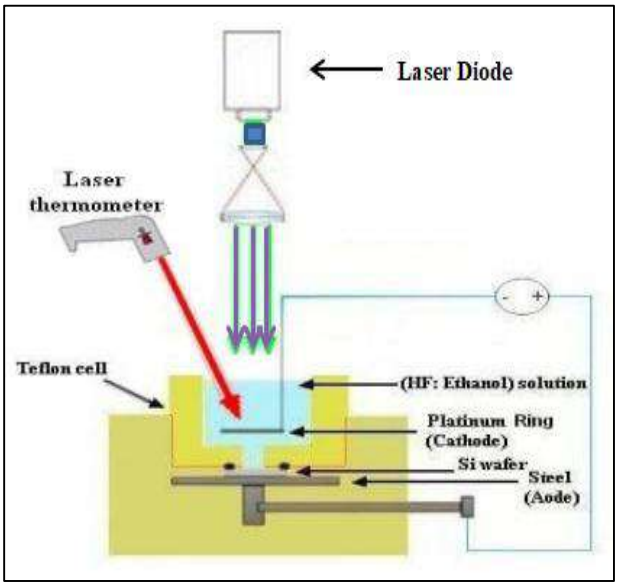

Figure 1. Schematic illustration of aggressive Laser-induced etching process

2.2 Production of hybrid SERS sensors.

In order to synthesis of HO-Si pillars and SiQDs / Au nanoparticle hybrid SERS sensors , a dilute solution of $6x10^{-3}$ M of high purity 99.9% salt was used by dissolving a specific weight of this salt in deionized distilled water. The HO-Si pillars and SiQDs based- nanostructures substrates were immersed for 2 minutes at room temperature, in the prepared $HAuCl_4$ solution which contains the Au-ions. The formation of Au nanoparticle above the HO-Si pillars and SiQDs nanostructures and hence the formation of hybrid SERS sensors was carried out through Au-ion reduction by Si–H dangling bonds on the surfaces and boundaries of Si nanostructures as presented in the formula (1) (Pohl, U. W. 2018).

Depending on the morphological nature of the Si nanostructures layer, the density of Si–H dangling bonds varied

$$Au^{+3} + 3e^{-} \rightarrow Au_{Nanoparticles} \quad (1)$$

The schematic representation of dipping technique of HO-Si pillars and SiQDs based-layers in HAuCl4 solution to synthesis the hybrid SERS sensors is illustrated in Figure 2.

The R6G solution with different concentrations ranging from 1.0×10^{-6} to1.0×10^{-12} M were used to identify the hybrid SERS sensors. While HO-Si pillars and SiQDs based- nanostructures substrate were tested at higher concentrations of about 1.0×10^{-4} .Every SERS sensor and based- nanostructures substrate were immersed into 25 mL of R6G solution for 5min to guarantee R6G adsorption on the nanostructures surface.

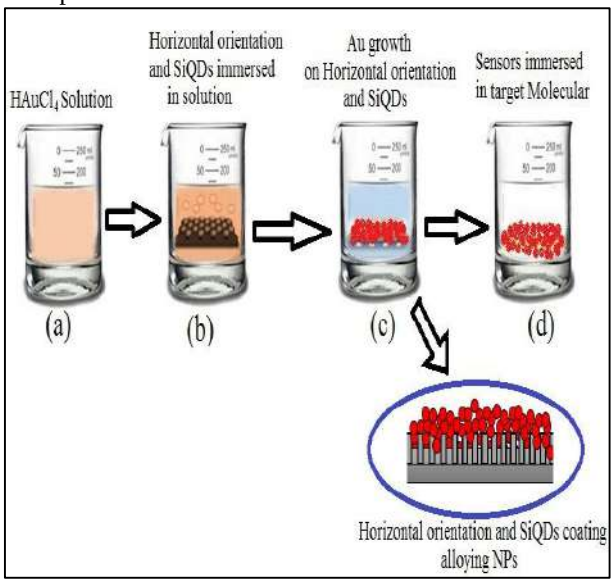

Figure 2. Schematic representation of formation **Au** nanoparticles by dipping technique.

2.3 Characteristic Techniques

The Structural, morphological characteristic of HO-Si pillars and SiQDs based-substrate and hybrid SERS sensors with plasmonics Au nanoparticles layer were analyzed using FE–SEM (FE–SEM; VEGA/TESCAN, XRD (XRD – 6000, Shemadzu power diffraction system with CuKα X–ray tube (λ=0.154056 nm),. Room temperature photoluminescence PL spectra were measured by system type (PL; Cary Eclipse FL 0912M014) with He Cd excitation laser wavelength of 320 nm. The Raman spectra of the of R6G dye deposited on HO-Si pillars and SiQDs based-substrate and hybrid SERS sensors were inspected with the dispersive Raman microscope (Senterra 2009, Bruker, Germany) with 785 nm and50 mW laser wavelength and power respectively . For each spectrum, the integration time was set as 10 s. To calculate the size distribution , surface density of SiQDs ,HO-Si pillars , and Au nanoparticles ,the dimensions of hotspot regions among Au nanoparticles from the FE-SEM a image special Image J software was used .

1. RESULTS AND DISCUSSIONS

3.1 Morphological aspects of HO-Si pillars and SiQDs nanostructures substrate and hybrid SERS sensors.

Figure 3a,d, display the FE-SEM images of HO-Si pillars and SiQDs based- nanostructures substrate .The morphological aspects of these type of nanostructures signifies a very significant factor in the growth and development of Au nanoparticles , where the nucleation sites (Si–Hx) dangling bonds are changed according to the morphology of the nanostructures substrate. The dangling bonds in the porous silicon layer play a fundamental role in the morphological properties of the nanomaterial layer deposited on it. The higher the density of the dangling bonds, the higher the reduction rate of the nanomaterial ions, and thus the growth rate of the nanoparticles increases and their size decreases (Wang, X. 2022). These different types of nanostructures substrate have been synthesized via various laser intensity. According to analysis of FE-SEM images, there were two specific forms of nanostructures morphologies:

1. The synthesis of non-connected HO-Si pillars nanostructures with a uniform cylindrical shape at different sizes deposited in random way over the etched zone ; Figure 3a. The cross-section form of the HO-Si pillars were almost spherical with diameters ranging from 30 to 70 nm, and lengths of the cylinder ranging from 80 to 350 nm. The surface density of this nanostructures was around $9x10^{8}$ Pillars.cm^{-2}. This

specific forms of nanostructures was synthesized on the Silicon surface at 450 mW/cm^2 laser intensity.

2. The synthesis of non-connected SiQDs nanostructures with orderly regular shape (approximately spherical form) and noteworthy low spam sizes; fig 3b. The surface density of SiQDs was around 3*10^{10} QDs.cm^{-2} with sizes ranging from 38 to 85 nm, and a highest distributed sizes located at 68 nm. This type of nanostructures was synthesized on the Silicon surface at 550 mW/cm^2 laser intensity.

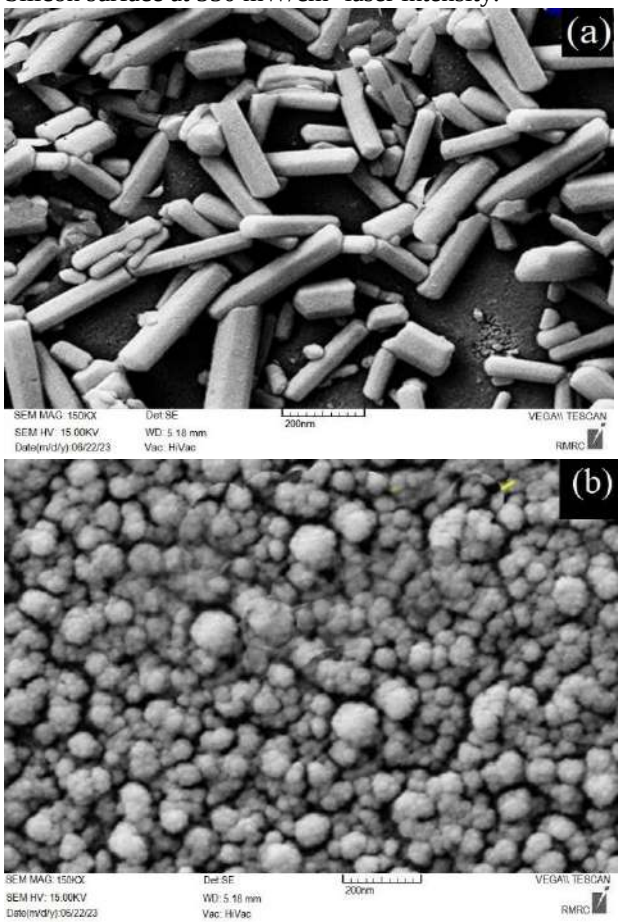

Figure 3. FE-SEM images of a) HO-Si pillars and b) SiQDs based- nanostructures substrate.

The Morphological aspects of the created Si nanostructures substrate can be understood as a distinctive imprint of the specification laser beam used in the aggressive etching process; particularly the intensity of the laser beam $\mathbf{p_{in_p}}$. An increase of the irradiating laser intensity can alter the photocurrent I_{photo} and therefore; the Si dissolution manner. The aggressive etching way be determined by the value of I_{photo} which is known via formula (2) (Alwan, A. M. 2014).

$$I_{Photo} = (1 - R_{Si\ Nano})P_{inp} \times \eta \times q/h_{\upsilon_o} \quad (2)$$

Where $R_{Si\ Nano}$ and η signifies the reflectivity and quantum efficiency of the Si nanostructures substrate respectively. While, $\mathbf{p_{in_p}}$ and υ_o presents the etching laser power and frequency of incident beam. Whereas h and q refer to Planck's constant and q is the electron charge respectively. The formation of HO-Si pillars and SiQDs nanostructures definitely be contingent on the Si dissolution manner as a result of the existence of positive holes at the Si nanostructures. These h^+ are formed both optically through the absorption of the laser photons and thermally through growing the temperature of the Si wafer in the course of the etching process (Abed, H. R. 2019). Consistent with K. Cheah hypothesis (Ko, F. H. 2015), the etching rate in the course of the aggressive Laser-induced etching path happens in 3-D directions x, y, and z. x and y signify the plane etching rate at the superficial upper layer, whereas z signifies the perpendicular etching rate on the wafer. The thermally-induced etching happens in 3-D directions but more rapidly in the illuminated zone, consequently, this etching will remove the synthesized Si nanostructures layer at the etched zone. The thermally and optically induced etching rates are ruled by means of the diffusion rate and the drift velocity of h+ to the illuminated zone (Wali, L. A. 2020). A particular quantity of the incident laser power will convert into heat P_{hea} inside the Si nanostructures and will lead to increase the temperature ΔT_r as exposed in formula (3) (Wali, L. A. 2020).:

$$\Delta T_r = P_{hea}/mcv \quad (3)$$

Where; $\Delta \boldsymbol{T}_r$ is the temperature rise and P_{hea} presents the portion of incident input laser power which is concerts to heat in substrate in the course of the etching path. The P_{hea} is connected to η via the following formula (4).

$$P_{hea} = (1 - \eta) \times (\text{laser power}) \quad (4)$$

Therefore, increasing the power of the laser beam falling on the substrate during etching will lead to an accelerated rise in temperatures in the substrate and in the liquid layer adjacent to it. Practically, increasing the power from 450 to 550 mW led to an increase in the temperature from 44 to 68 C^o. This sharp rise in the temperature of the substrate and the zone adjacent to it is mainly caused by the small wavelength of the laser beam used , which is 405 nm , as the smaller wavelength , the shorter the absorption depth (Alwan, A. M. 2011). So, the depth of absorption of the laser beam will be superficial and does not occur deep in the substrate, and therefore the temperature rise will be high

within the etching area, especially the surface layer. One of the results of this high temperature, in addition to the low value of thermal conductivity of the silicon nanostructures, is the acceleration of the removal of the silicon nanostructures resulting from etching and the formation of a colloidal solution in the etching space (Chang, C. C. 2012, Jabbar, A. A. 2020, Hou, X. 2011, Khalaf, A. A. 2021).

The thermal conductivity of silicon nanostructures is a function of the sizes of nanostructures, as the size was decreased, the thermal conductivity will decrease. For silicon nanostructures with a size of 60 to 200 nm, the value of thermal conductivity is round 0.74 W/m/K (Alwan, A. M. 2015), while the thermal conductivity of silicon is 160 W/m/K (Sychugov, I. 2005). This, in turn, will increase the possibility of removing nanostructures due to the increased thermal etching rate.

This, in turn, will also increase the possibility of fragmentation of silicon nanostructures of HO-Si pillars and SiQDs . Therefore, the aggressive etching process at high laser intensities and high temperature will modify the morphological aspects of nanostructures. According to the heating effect in the laser – substrate interaction and the superficial zone of solution (wealthy with colloidal suspension nanostructures), the proposed mechanism of HO-Si pillars and SiQDs structures growth overhead the etched substrate happened via the deposition of colloidal nanostructures in a path very near to laser pyrolysis method (Sulaiman, D. 2022, Xu, S. H. 2003, Alwan, A. M. 2020, Xu, S. H. 2003).

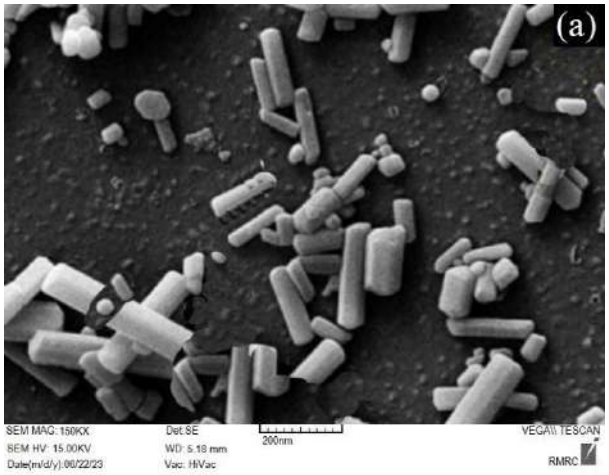

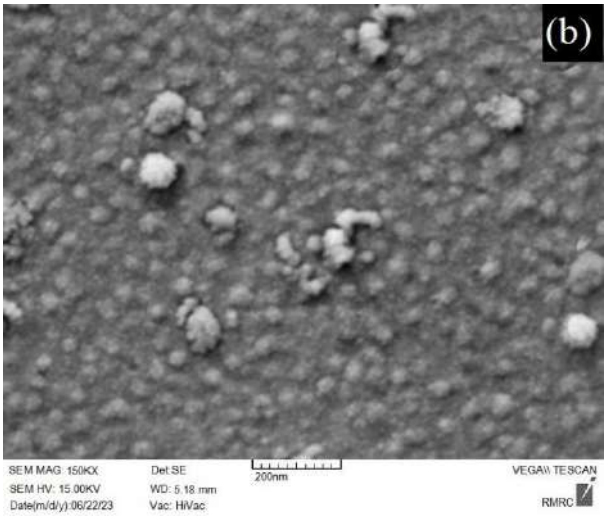

Figure 4. FE-SEM images of a) HO-Si pillars and b) SiQDs based- nanostructures substrates.

Fig 4a,b, shows the FE-SEM images of HO-Si pillars and SiQDs nanostructures later integrating the Au nanoparticles (hybrid SERS sensors). Since the amount of nucleation sites ($Si–H_x$) dangling bonds which is changed reliant on the morphology of the synthesized Si nanostructures layer. The Au nanoparticle were deposited in based on the Weber-Vomer mechanism, in which the formation of Au nanoparticle essentially happened at the lower etched Silicon layer owing to the immediate development of Au nanoparticle through Au ion reduction by dangling bonds on the faces of Si nanostructures . This deposition manner of nanoparticles have a large tendency to bury the lower etched silicon region and leads to remove some of HO-Si pillars and SiQDs nanostructures from the created layer.

The EDX spectra of Au nanoparticle deposited on HO-Si pillars and SiQDs nanostructures are exposed in fig 5a, b where the development of Au nanoparticle and the presence of Si materials is revealed. From this figure, it is obvious that the amount of Au nanoparticles differs with the type of nanostructures of layer. The amount of Au nanoparticle in the SiQDs substrate was greater than that of the HO-Si pillars substrate; as a result of the higher gold ion reduction centers in the SiQDs.

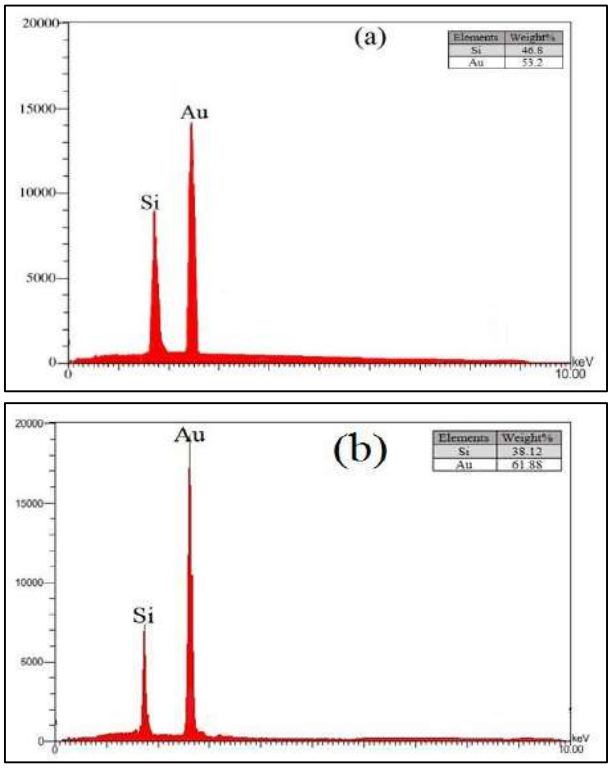

Figure 5. The EDX pattern of hybrid SERS sensors a) HO-Si pillars and b) SiQDs.

The XRD patterns of the Au nanoparticle/ HO-Si pillars and Au nanoparticle / SiQDs, hybrid SERS sensors correspondingly, are demonstrated in Fig. 6(a,b) ,which displays that for both of HO-Si pillars and SiQDs hybrid SERS sensors just a one specific diffraction peak seemed at 2θ about of 32.9° which is allocated to the (100) plane of crystalline Si consistent with the standards (JCPDS). Also , this Figure , shows two particular peaks located at 2θ around of 38.3° and 44.38° for the Au nanoparticle / HO-Si pillars and at 2θ about of 38.38° and 44.37° for the Au nanoparticle / SiQDs, hybrid which are allocated to the (111) and (200) crystal planes of Au, correspondingly. These diffraction peaks are in good match to pure Au element with face centered cubic symmetry (FCC). These diffraction peaks is clearly widened as related with bulk Au, signifying the creation of Au nanoparticle. From this diffraction pattern, it is obvious that the Au deposition process indications to the reducing in the diffraction peaks of the (100) plane of Si, this is recognized to the covering of the nanostructures surfaces by the Au nanoparticle. The sizes of the Au nanoparticle (D) are computed via Scherrer's equation (5) (Rashid, R. B. 2022) as follows:

$$D = \frac{0.9\lambda}{\beta \cos\theta} \quad (5)$$

Where, θ, β are diffraction angle (degree) and full width at half maximum (radians) respectively , while λ presents the wavelength in nm of employed radiation .

The Specific surface area of metallic nanoparticles (S) in hybrid structures is a very important parameter that indicates the efficiency of the hybrid SERS sensor. The efficiency of the hybrid sensor increases with the increase in its surface area . The (S) of the sensor is calculated depending on the size (D) and the density ρ_{Au} of of metal nanoparticle with the following relation (6) (Rashid, R. B. 2022).

$$S = \frac{6000}{\rho D} \quad (6)$$

For the (111) crystal plane, the value of D and S of Au nanoparticle are 7.26 nm and 35.41 m^2 /g, correspondingly, for Au nanoparticle / HO-Si pillars and 4.3 nm and 51.1 m^2 /g for Au nanoparticle / SiQDs, hybrid SERS sensor , correspondingly. As the FE–SEM images specify the agglomerated Au nanoparticle sizes, of the hybrid SERS sensor which were assessed from the XRD pattern are lower than that of attained from the FE–SEM images. The greater nanoparticles is strongly related with the propensity of the Au nanoparticle to conglomerate as a result of their excessive surface energy and surface tension among the ultrafine nanoparticles (Rashid, R. B. 2022).

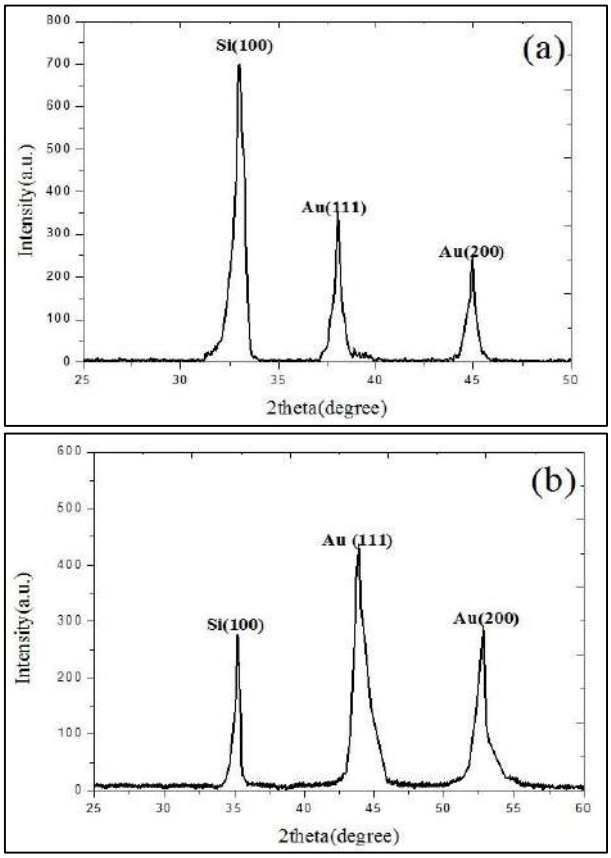

Figure 6. The XRD patterns of hybrid SERS sensors a) HO-Si pillars and b) SiQDs.

The photoluminescence spectra (PL) of HO-Si pillars and SiQDs based- nanostructures substrate and hybrid SERS sensors are presented in fig 7 a,b. The emission PL patterns be influenced by the morphology of the based- nanostructures substrate, the amount of Si nanostructures species , the amount of nucleation sites ($Si–H_x$) dangling bonds and the morphology of the Au nanoparticle on the hybrid SERS layer. The wavelengths and intensity of the emission PL, in addition to energy gap, and the enhancement factor of PL intensity were tabulated in table 1. As of this table, earlier integrating Au nanoparticle, shortest PL emission wavelength, i.e greater energy gap (Eg) was attained for SiQDs nanostructures, whereas longest PL emission wavelength, i.e lesser energy gap was recognized with HO-Si pillars nanostructures. Also; for SiQDs hybrid SERS sensor, exposed a higher peak intensity compared their comparative based- nanostructures substrate. This manners took place via the Si nanostructures involved with Au nanoparticle; due to the cancelling the effects of the (Si–Hx) dangling bonds ,which essentially act as nonradiative recombination sites which works to reduce the emission intensity resulting from the Si nanostructures . Furthermore, the FWHM of the PL emission from Si nanostructures was reduced with blue shifting in PL emission wavelength later integrating the Au nanoparticles. The hybrid SERS sensor of SiQDs, has a much higher intensity compared with the hybrid SERS sensor HO-Si pillars due to higher surface density of SiQDs in sensing area. The enhancement factor (e.f) in the intensity of PL emission after the integrating of Au nanoparticle is a strong evidence to investigate the activity of the hybrid SERS sensors. As the enhancement factor increases, the efficiency of the sensor increases. The concentration of gold ions is an important factor in determining the morphology of the gold nanoparticle layer deposited on the porous silicon surface. Increasing the concentration of gold ions leads to an increase in the surface density of gold nanoparticles, which in turn enhances the SERS-based sensing process. This in turn leads to an increase in the Raman signal intensity, and consequently, an increase in the Raman enhancement factor (E.f.). The value of e.f was around 2.1, and 0.45 for hybrid SERS sensor of Au nanoparticle / SiQDs and Au nanoparticle / HO-Si pillars, respectively. The increasing PL intensity is mainly depended on the amount of nanocrystallites' luminescence in the synthesized substrate owing to the rise of electron-hole recombination rate substrate [10]. The reliance of energy gap (Eg) of Si nanostructures on its dimensions was in good agreement with the suggested model by Suemune et al as shown in formula (7) (Alwan, A. M. 2020).

$$Eg = (Si) + (h\ 2\pi\ 2k)/ (2mr^{*}L\ 2) \quad (7)$$

Where; mr* is the reduced effective mass, k is a constant equals 2 for a pillar and 3 for SiQDs, whereas L is the dimension of nanostructures

Table 1: wavelength, intensity of PL , Eg, and e.f of hybrid SERS sensors

Sensor type	PL intensity (a.u.)	Peak emission (nm)	Energy gap(eV)	E.F
Hybrid HO-Pillars	1420	599	2.07	0.45
Based HO-Pillars	639	548	2.26	----
Hybrid SiQDs	1260	580	2.1	----
Based SiQDs	600	645	1.92	2.1

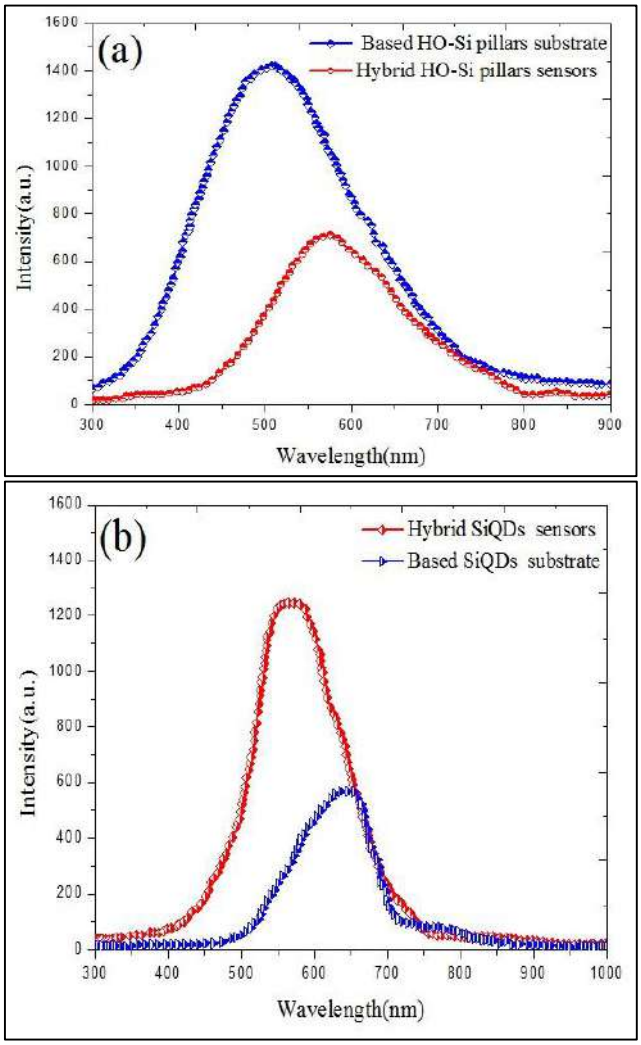

Figure 7. The PL emission of HO-Si pillars and SiQDs based- nanostructures substrate and its related hybrid SERS sensors.

3.2 Raman studies of hybrid SERS sensors

Figure 8a,b displays the Raman spectra of R6G molecules adsorbed on based HO-Si pillars and SiQDs nanostructures and its related hybrid SERS sensors of HO-Si pillars and SiQDs substrates which is excited at 532 nm . In spite of this higher concentrations of R6G molecules of about 10^{-4} M concentration ,the substrates of based HO-Si pillars and SiQDs ,show a low level of Raman signal due to the low value of Raman cross section area (Sulaiman, D. 2022). Also , this figure , display the SERS spectra of R6G dye at different concentrations ranging from 1.0×10^{-6} to1.0×10^{-12} M adsorbed on hybrid SERS sensor of Au nanoparticle / SiQDs and Au nanoparticle / HO-Si pillars . The peaks appearing at 650, 1190, 1328, 1282, and 1382 cm^{-1} are the normal Raman peaks of R6G molecules

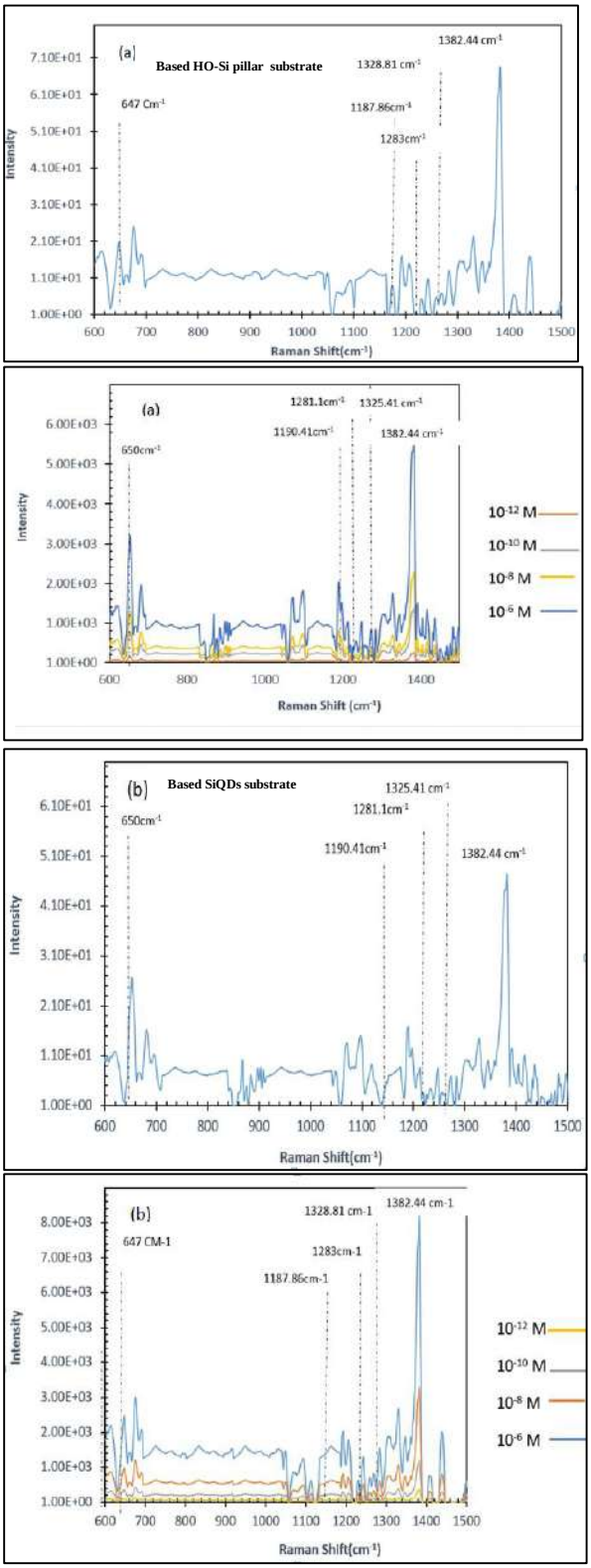

Figure 8. Raman spectra and SERS of a) HO-Si pillars and b) SiQDs.

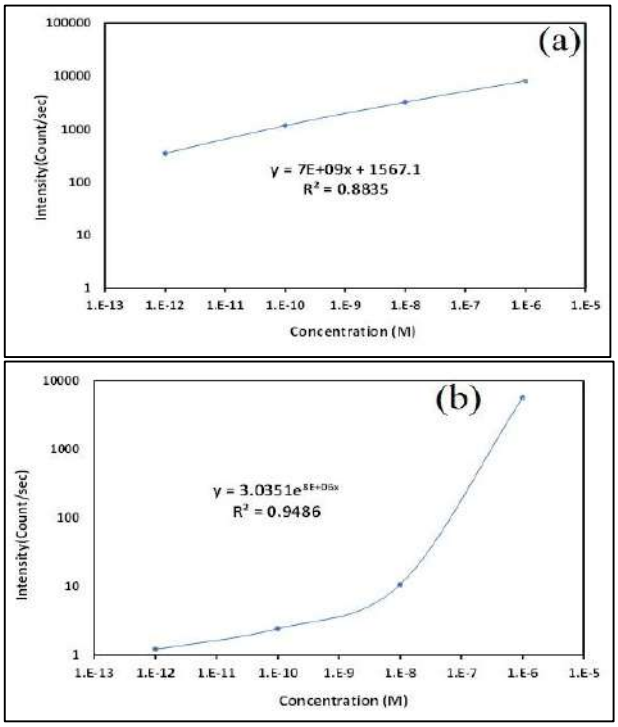

Figure 9: Relation between SERS intensity of the main Raman peak of about 1382.44 cm^{-1} and concentration for a) HO-Si pillars and b) SiQDs.

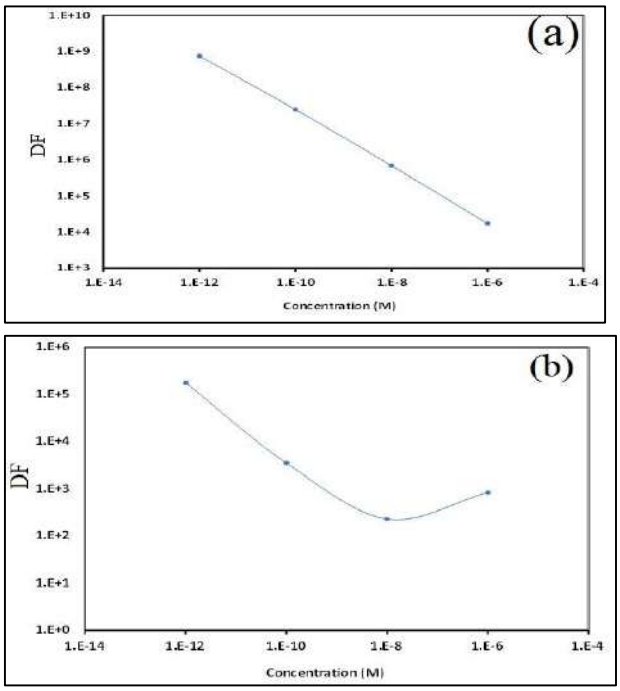

Figure 10: present the development factor of the main Raman peak of about 1382.44 cm^{-1} for a) HO-Si pillars and b) SiQDs.

To perform a quantitative analysis of the of hybrid SERS sensor of Au nanoparticle / SiQDs and Au nanoparticle / HO-Si pillars, a relationship between the characterized peak intensity 1382.44 cm^{-1} and the concentrations of R6G molecules was shown in Fig. 9a and b . The figure 9b , shows an exponential behavior of relationship of SERS signal intensity with the R6G molecules concentration from 1.0×10^{-6} to1.0×10^{-12} M as follows in equation(8)

$$\mathbf{Y=3.0351\ e^{8E+6x}\ \ with\ \ R^2=0.9486} \qquad \mathbf{(8)}$$

This type of relationship offers very high Raman output and arises due to the excitation of localized Plasmon's in Au nanoparticles when illuminated by light. The plasmonics field created by the nanoparticles strongly interacts with the adsorbed of R6G molecules, in an enhanced Raman scattering signal. The magnitude of the electromagnetic enhancement is directly proportional to the incident light intensity, which is often constant during the experiment. Therefore, the SERS signal intensity is expected to increase exponentially with R6G molecules concentration, reflecting the increased numbers of dye molecules contributing to enhance Raman scattering. For Fig. 9a, the shape of the relationship between the concentration of R6G molecules and the intensity of Raman peak of the hybrid sensor employing HO-Si pillars is linear with a low slope, which indicates inefficient response to the sensor. The linearity equation is described by the following formula (9).

$$Y=7E^{+9x}+1567.1 \quad \text{with } R^2=0.8\,835 \qquad (9)$$

This linearity arises from the fact that the SERS enhancement process is proportional with the number of molecules participating in the scattering process. As the concentration increases, more molecules are available for interaction with the surface Plasmon's of Au nanoparticles, leading to proportional increase in the SERS signal intensity. The Raman signal intensity, can also exhibit linear behavior with the surface area (S) of the hybrid sensor. A large surface area provide more sites (hot spot regions) for the adsorption of analyte molecules and increases the probability of interaction with the enhanced electromagnetic field. Consequently, the SERS signal intensity increases linearly with the surface area. The achieved results of the hybrid SERS sensor which involves Au nanoparticle / SiQDs provide excellent opportunity for target molecules analysis. The chief cause for this distinguished behavior is due to the high density of hot spots regions among the gold nanoparticles; furthermore to the high surface of gold nanoparticles deposited on the SiQDs as well as the high surface density of SiQDs compared to the HO-Si

pillars substrate in which the surface area of the gold nanoparticles is less and its surface density is much lower. As the process of energy transfer from gold nanoparticles that are in the plasmonics state to the target molecules that are detected will increase with the increase in the density of the nanoparticles and with increase in the density of hot spots regions.

The furthermost significant factor for evaluating the activity of the hybrid SERS sensors, is the development factor (DF) of the characterized peak intensity 1382.44 cm^{-1} after integrating Au nanoparticle. The DF was computed by using equation 10 (Khalaf, A. A. 2021).

$$DF = (I_{SERS} \times C_R)/(I_R \times C_{SERS}) \quad (10)$$

Where, I_{SERS}, I_R are the signal intensities of the SERS and Raman, at the R6G concentration of C_{SERS} and C_R respectively. Figure (10 a,b) shows the DF versus the concentrations of R6G dye, adsorbed on the surface of the hybrid SERS sensor of HO-Si pillars and SiQDs, respectively. This figure, confirm that the DF increase with the decreasing of the R6G dye concentration. The highest DFs of R6G (7.46×10^8) and (1.77×10^5) at 10^{-12} M ultra-low concentration are obtained for Au nanoparticle / SiQDs hybrid sensor and for the Au nanoparticle / HO-Si pillars hybrid sensor, respectively. The R6G dye detection process is at ultra-low concentration with a higher value of DF (7.46×10^8), due to the high density of hot spots regions among the gold nanoparticles; furthermore to the high surface of gold nanoparticles deposited on the SiQDs as well as the high surface density of SiQDs compared to the HO-Si pillars.

For the synthesized hybrid sensor, based on the sensitivity relationship figure 9a,b , which signify the relation between the characterized peak intensity 1382.44 cm^{-1} and dye concentrations, the sensing limit of detection of the hybrid sensors can be calculated via using the equation (11) (Sychugov, I. 2005).

$$LOD = \frac{3S_e}{d} \quad (11)$$

Where Se is the standard deviation of characterized peak intensity Au nanoparticle / SiQDs hybrid sensor and for the Au nanoparticle / HO-Si pillars hybrid sensor, and d represents the slope of the linear portion of the sensitivity curve. The minimum achieved value of LOD is obtained from the Au nanoparticle / SiQDs hybrid sensor of about , 9*10 -14 M , whereas for Au nanoparticle / HO-Si pillars hybrid sensor the value of LOD is greater than that of SiQDs hybrid sensor by about two order of magnitude of around 1*10 -13 M.

Figure 11, displays the reproducibility of the synthesized SERS hybrid sensors. The best one is the sensor that offers the lowest difference in Raman signal. The SERS hybrid sensors, synthesized with Au nanoparticle / SiQDs, display lowest variation in Raman signal with 10 various testing positions. This excellent behavior of the hybrid sensor is connected with the homogeneity of the gold nanoparticles layer of Au nanoparticle / SiQDs. The variation of Au nanoparticle / SiQDs hybrid sensor and for the Au nanoparticle / HO-Si pillars hybrid sensor are about 4%, and 11% respectively.

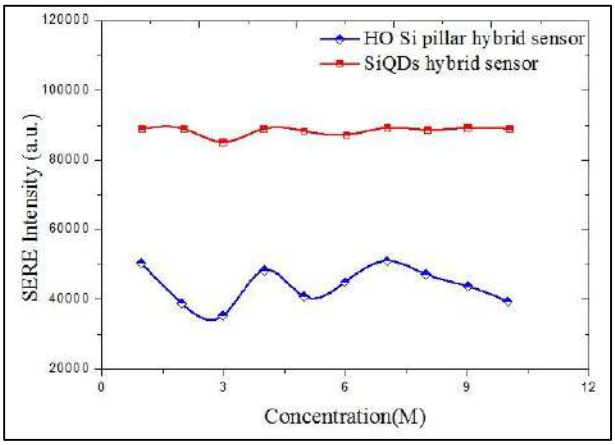

Figure 11. The reproducibility of the main Raman peak of about 1382.44 cm^{-1} for HO-Si pillars and SiQDs

2. CONCLUSIONS

In the present study, two types of hybrid SERS sensors, have been synthesized through employing integrating Au nanoparticles on HO-Si pillars and SiQDs nanostructures substrate . Uppermost Raman signal is attained for Au nanoparticle / SiQDs hybrid sensor comparing with Au nanoparticle / HO-Si pillars hybrid sensor by around two orders of magnitude was recorded. The efficiency of hybrid sensor is strongly linked with the high density of hot spots regions among the gold nanoparticles in addition to the high surface of gold nanoparticles deposited on the SiQDs as well as the high surface density of SiQDs compared to the HO-Si pillars substrate. Higher development factor, with minimum LOD and outstanding reproducibility was realized later integrating gold nanoparticles on SiQDs substrate by simple, easy –to- work and very low cost dipping technique. The results obtained from this study are of distinguished value in fabricating hybrid SERS sensors.

REFERENCES

Abed, H. R., Alwan, A. M., Yousif, A. A., & Zayer, M. Q. (2019). Efficient SnO_2/CuO/porous silicon nanocomposites structure for NH_3 gas sensing by incorporating CuO nanoparticles. *Optical and Quantum Electronics*, *51*(10), Article 333. https://doi.org/10.1007/s11082-019-2076-2

Ali, W. H., Dheyab, A. B., Alwan, M. A., & Abber, Z. S. (2020). Study the role of mud-like porous silicon morphologies on the performance of AuNPs SERS sensor for efficient detection of amoxicillin. *AIP Conference Proceedings*, *2290*, Article 050061. https://doi.org/10.1063/5.0027318

Alwan, A. M., & Ahmed, Z. S. (2014). The opto-electronic characteristics of multi-porosity silicon system. *Engineering and Technology Journal*, *32*, 811–817.

Alwan, A. M., & Ali, S. M. (2015). Gradient-porosity porous silicon (GPSi) as anti-reflection coating in solar cells applications. *Engineering and Technology Journal*, *33*(B1), 152–159.

Alwan, A. M., Dheyab, A. B., & Allaa, A. J. (2017). Study of the influence of incorporation of gold nanoparticles on the modified porous silicon sensor for petroleum gas detection. *Engineering and Technology Journal*, *35*(8A), 811–815.

Alwan, A. M., & Jabbar, A. A. (2011). Design and fabrication of nanostructures silicon photodiode. *Modern Applied Science*, *5*(1), 106–112. https://doi.org/10.5539/mas.v5n1p106

Alwan, A. M., Naseef, I. A., & Dheyab, A. B. (2018). Well controlling of plasmonic features of gold nanoparticles on macro porous silicon substrate by HF acid concentration. *Plasmonics*, *13*(6), 2037–2045. https://doi.org/10.1007/s11468-017-0667-5

Alwan, A. M., Rashid, R. B., & Dheyab, A. B. (2018). Morphological and electrical properties of gold nanoparticles/macro porous silicon for CO_2 gas. *Engineering and Technology Journal*, *59*(1A), 57–66.

Alwan, A. M., Zayer, M. Q., Jabbar, A. A., & others. (2020). Optimizing the performance of extended-gate field-effect transistor (EGFET) pH sensor by regulating the structural properties of the nanostructured porous silicon layer. *Journal of Theoretical and Applied Physics*, *14*(Suppl 1), 61–70. https://doi.org/10.1007/s40094-020-00404-7

Alwan, M. A. (2007). Calculation of energy band gap of porous silicon based on the carrier transport mechanisms. *Engineering and Technology Journal*, *25*(10), 1143–1148.

Alwan, A. M., & Abdulrazaq, O. A. (2008). Aging effect on the photosynthesized porous silicon. *International Journal of Modern Physics B*, *22*(3), 417–422. https://doi.org/10.1142/S0217979208050042

Brenner, D. J., Doll, R., Goodhead, D. T., Hall, E. J., Land, C. E., Little, J. B., Lubin, J. H., Preston, D. L., Preston, R. J., & Puskin, J. S. (2003). Cancer risks attributable to low doses of ionizing radiation: Assessing what we really know. *Proceedings of the National Academy of Sciences*, *100*(24), 13761–13766. https://doi.org/10.1073/pnas.2235592100

Canham, L. T. (1990). Silicon quantum wire array fabrication by electrochemical and chemical dissolution of wafers. *Applied Physics Letters*, *57*(10), 1046–1048. https://doi.org/10.1063/1.103561

Chalhoub, A. E., Semmar, N., Coudron, L., Gautier, G., & Boulmer-Leborgne, C. (2011). Thermal conductivity measurement of porous silicon by the pulsed-photothermal method. *Journal of Physics D: Applied Physics*, *44*(1), Article 015402. https://doi.org/10.1088/0022-3727/44/1/015402

Chang, C. C., Kuang-Hsuan, Y., Yu-Chuan, L., & Ting-Chu, H. (2012). New pathway to prepare gold nanoparticles and their applications in catalysis and surface-enhanced Raman scattering. *Colloids and Surfaces B: Biointerfaces*, *93*, 169–173. https://doi.org/10.1016/j.colsurfb.2011.12.031

Cheng, X. Y., Hinde, E., Owen, D. M., Lowe, S. B., Reece, P. J., Gaus, K., & Gooding, J. J. (2015). Enhancing quantum dots for bioimaging using advanced surface chemistry and advanced optical microscopy: Application to silicon quantum dots (SiQDs). *Advanced Materials*, *27*(36), 6144–6150. https://doi.org/10.1002/adma.201502281

Dheyab, A. B., Alwan, A. M., & Zayer, M. Q. (2019). Optimizing of gold nanoparticles on porous silicon morphologies for a sensitive carbon monoxide gas sensor device. *Plasmonics*, *14*(2), 501–509. https://doi.org/10.1007/s11468-018-0803-1

Ershov, I. A., Iskhakova, L. D., Krasovskii, V. I., Milovich, F. O., Rasmagin, S. I., & Pustovoi, V. I. (2020). Synthesis of silicon-carbide nanoparticles by the laser pyrolysis of a mixture of monosilane and acetylene. *Semiconductors*, *54*(11), 1467–1471. https://doi.org/10.1134/S1063782620110033

Giorgis, F., Descrovi, E., Chiodoni, A., Froner, E., Scarpa, M., Venturello, A., & Geobaldo, F. (2008). Porous silicon as efficient surface enhanced Raman scattering (SERS) substrate. *Applied Surface Science*, *254*(22), 7494–7497. https://doi.org/10.1016/j.apsusc.2008.05.323

Hamoudi, W. K., Alwan, M. A., & Sulaiman, D. (2020). Controllable formation of plasmonic gold nanoparticles by pulsed laser–induced etching.

Optical and Quantum Electronics, *52*, Article 351. https://doi.org/10.1007/s11082-020-02466-w

He, Y., Xiao, S., Dong, T., & Nie, P. (2019). Gold nanoparticles with different particle sizes for the quantitative determination of chlorpyrifos residues in soil by SERS. *International Journal of Molecular Sciences*, *20*(11), 2817. https://doi.org/10.3390/ijms20112817

Hou, X., Zhang, X., Chen, S., Fang, Y., Li, N., Zhai, X., & Liu, Y. (2011). Size-controlled synthesis of Au nanoparticles and nanowires and their application as SERS substrates. *Colloids and Surfaces A: Physicochemical and Engineering Aspects*, *384*(1–3), 345–351. https://doi.org/10.1016/j.colsurfa.2011.04.018

Jabbar, A. A., Alwan, M. A., Zayer, M. Q., & Azhar, J. (2020). Efficient single cell monitoring of pathogenic bacteria using bimetallic nanostructures embedded in gradient porous silicon. *Materials Chemistry and Physics*, *241*, Article 122359. https://doi.org/10.1016/j.matchemphys.2019.122359

Jubair, D. S., Alwan, M. A., & Hamoudi, W. K. (2021). Sensing performance of mono and bimetallic nano photonics surface enhanced Raman scattering (SERS) devices. *Engineering and Technology Journal*, *39*(7), 1174–1184.

Khalaf, A. A., Alwan, A. M., Attallah, A. H., & Dheyab, A. B. (2021). Influence of magnetic field on the characteristics of n-type porous silicon prepared by photo-electro-chemical etching process. *Journal of Physics: Conference Series*, *1963*, Article 012015. https://doi.org/10.1088/1742-6596/1963/1/012015

Ko, F. H., Tai, M. R., Liu, F. K., & Chang, Y. C. (2015). Au–Ag core–shell nanoparticles with controllable shell thicknesses for the detection of adenosine by surface enhanced Raman scattering. *Sensors and Actuators B: Chemical*, *211*, 283–289. https://doi.org/10.1016/j.snb.2015.01.052

Kumar, V., Saxena, K., & Shukla, A. K. (2013). Size-dependent photoluminescence in silicon nanostructures: Quantum confinement effect. *Micro & Nano Letters*, *8*(6), 311–314. https://doi.org/10.1049/mnl.2013.0086

Liu, L. R., Zhu, G. B., Zeng, W., Yi, Y. H., Lv, B. H., Qian, J. J., & Zhang, D. P. (2019). Silicon quantum dot-coated onto gold nanoparticles as an optical probe for colorimetric and fluorometric determination of cysteine. *Microchimica Acta*, *186*(2), Article 98. https://doi.org/10.1007/s00604-018-3162-1

Liu, Y. N., Wang, Q. Z., Guo, S. W., Jia, P., Shui, Y. H., Yao, S. Y., Huang, C., Zhang, M., & Wang, L. (2018). Highly selective and sensitive fluorescence detection of hydroquinone using novel silicon quantum dots. *Sensors and Actuators B: Chemical*, *275*, 415–421. https://doi.org/10.1016/j.snb.2018.08.066

Naseef, I. A., & Alwan, A. M. (2017). Optimization of photoluminescence properties of porous silicon by adding gold nanoparticles. *Iraqi Journal of Science*, *58*(1A), 53–62.

Naseef, I. A., Dheyab, A. B., Wali, L. A., & Alwan, A. M. (2019). Perfect incorporation of AuNPs on the p-n+ porous silicon for highly-efficient solar cells. *Optik*, *198*, Article 163317. https://doi.org/10.1016/j.ijleo.2019.163317

Pohl, U. W. (2018). Low-dimensional semiconductors. In *Springer Handbook of Materials Data* (pp. 1081–1104). Springer. https://doi.org/10.1007/978-3-319-38925-7_37

Rashid, R. B., Alwan, M. A., & Mohammed, M. S. (2022). Improved difenoconazole pesticide detection limit via double-sided porous silicon layers' electrical sensor. *Materials Chemistry and Physics*, *287*, Article 126286. https://doi.org/10.1016/j.matchemphys.2022.126286

Sulaiman, D., Alwan, A. M., & Hamoudi, W. K. (2022). Pesticide detection optimization of plasmonic gold nanoparticles/silicon nano-columns structures by controlling the coupling lasers power density. *Gold Bulletin*, *55*, 19–30. https://doi.org/10.1007/s13404-022-00323-x

Sychugov, I., Juhasz, R., Linnros, J., & Valenta, J. (2005). Luminescence blinking of a Si quantum dot in a SiO_2 shell. *Physical Review B*, *71*(11), Article 115331. https://doi.org/10.1103/PhysRevB.71.115331

Wali, L. A., Dheyab, A. B., & Alwan, A. M. (2023). Study the influence of shell thickness in bimetallic Ag core & Au shell configurations integrated in bare Si PN junction solar cells. *Materials Science in Semiconductor Processing*, *288*, Article 116210. https://doi.org/10.1016/j.mseb.2023.116210

Wali, L. A., Hasan, K. K., & Alwan, A. M. (2020). An investigation of efficient detection of ultra-low concentration of penicillins in milk using AuNPs/PSi hybrid structure. *Plasmonics*, *15*, 1487–1495. https://doi.org/10.1007/s11468-020-01220-0

Wail, H. A., Dheyab, A. B., & Alwan, A. M. (2018). Optimization and synthesis of gold nanoparticles on N-type porous silicon substrates as highly-gas sensitive. *International Journal of Mechanical Engineering and Technology*, *9*(10), 1393–1401.

Wang, X., Zhang, E., Shi, H., Tao, Y., Ren, X., & Zi, J. (2022). Semiconductor-based surface enhanced Raman scattering (SERS): From active materials to performance improvement. *Analyst*, *147*(7), 1257–1272. https://doi.org/10.1039/D1AN02082D

Xu, S. H., Xiong, Z. H., Gu, L. L., Liu, Y., Ding, X. M., Zi, J., & Hou, X. Y. (2003a). Preparation of one-dimensional porous silicon photonic quantum-well structures. *Applied Physics A*, *76*(4), 589–592. https://doi.org/10.1007/s00339-002-1935-2

Xu, S. H., Xiong, Z. H., Gu, L. L., Liu, Y., Ding, X. M., Zi, J., & Hou, X. Y. (2003b). Photon confinement in one-dimensional photonic quantum-well structures of nanoporous silicon. *Solid State Communications*, *126*(2), 125–128. https://doi.org/10.1016/S0038-1098(03)00270-1

Zhang, Y., Gu, C., Schwartzberg, A. M., & Zhang, J. Z. (2005). Surface-enhanced Raman scattering sensor based on D-shaped fiber. *Applied Physics Letters*, *87*(12), Article 123105. https://doi.org/10.1063/1.2048816

PURE SCIENCES
International Journal of Kerbala

Pure Sciences International Journal of Kerbala

Year: 2025 Volume : 2 Issue : 8 ISSN: 6188-2789 Print 3005 -2394 Online

Pure Sciences International Journal of Kerbala

Descriptive Study of the Species Eudiaptomus Vulgaris (Schmeil, 1896) Belong to Genus Eudiaptomus (Kiefer, 1932) , from the Al-Hussainiya River in the Holy Karbala Governorate

Hajir Mohammed Kadhim [a*]

[a] *Department of Biology , College of Education for Pure Sciences, University of Kerbala , Karbala, Iraq*

P A P E R I N F O

Received: 12.09.2025
Accepted: 19.10.2025
Published: 31.12.2025

keywords:
Eudiaptomus vulgaris, Diaptomidae, morphology, taxonomy, ecological observations, Iraq

A b s t r a c t

After determining the date and location of sample collection, this study examined the external morphology of the species. Samples were collected from the Al-Hussainiya River, located north of Karbala Governorate. The genus Eudiaptomus vulgaris is widely distributed across various aquatic systems. Species identification was based on morphological characteristics of the body, including overall shape and specific diagnostic features such as the number and structure of antennae, the arrangement of spines on the basal segment of the antennule, the morphology of the fifth peduncle, and the structure of the caudal branches. This study aims to represent one of the few detailed taxonomic studies on members of the order Calanoida in Iraq, contributing to the enrichment of biodiversity records for freshwater zooplankton. Moreover, the precise description of this species provides a valuable reference for future ecological assessments and water quality monitoring, as such organisms serve as important bio indicators in aquatic ecosystems. Due to the scarcity of detailed taxonomic research on species of the order Calanoida, this study highlights the importance of clarifying their taxonomic status. This was achieved by examining their external morphology, diagnosing and describing their structures, and providing illustrative drawings of their body parts.

DOI: 10.53851/psijk.v2.i8.28-34

Table 1. Abbreviation Table

NOMENCLATURE		NOMENCLATURE	
AbSo	Abdominal Somatic	Enp	Endopod
An So	Anal Somatic	Exp	Exopod
A1	Antenna	FuR	Furcal Rami
A2	Antennule	PrCx	Pre Coxa
Bs	Base	Md	Mandible
GS Seg	Genetic Segment	Mxp	Maxilliped
Ceph	Cephalothorax	Mx	Maxilla
Cx	Coxa	Mxl	Maxillule
Ur	Urosoma	P1	1^{rd}Pereopoda
Se	Seta	P2	2^{rd}Pereopoda
Sp	Spine	P3	3^{rd}Pereopoda
Seg	Segment	P4	4^{th}Pereopoda
So	Somatic	P5	5^{th}Pereopoda
Cl	Claws	Pr	Prosoma
Cx Ep	Coxa Epipodite		

* Corresponding Author Institutional Email:
hajer.m@uokerbala.edu.iq (Hajir Mohammed Kadhim)

1.INTRODUCTION

Arthropods represent one of the largest phyla of the animal kingdom, comprising over 1.5 million described species. They exhibit diverse ecological roles as herbivores and carnivores, supported by physiological and behavioral adaptations that allow them to exploit varied nutritional and environmental resources (Zhang & Liu, 2013; Matthew *et al*., 2013). Among them, crustaceans inhabit aquatic and semi-terrestrial environments, often found under damp stones or in decaying organic matter (Nkwoji, 2016). Although traditionally considered a subphylum, some researchers regard crustaceans as a distinct phylum, given their inclusion of all hexapod lineages (Ji *et al*., 2018). The scientific study of crustaceans is termed Malacostracology (Martín *et al*., 2014) Copepods are minute planktonic crustaceans widely distributed in inland waters such as rivers, lakes, ponds, and groundwater (Kobayashi *et al*., 2018; Sanoamuang & Dabseepai, 2021). Freshwater copepods are classified into three main orders: Cyclopoida, Harpacticoida, and Calanoida, with calanoids dominating pelagic zones of ponds, estuaries, and lakes. Within inland waters, the family Diaptomidae is the most species-rich group of calanoids (Ding *et al*., 2024). Their distribution and diversity are strongly influenced by environmental factors, particularly temperature (Kumar & Krishnan, 2021), salinity (Beaver *et al*., 2019), and pH (Cai *et al*., 2021). Eudiaptomus, a representative genus of Diaptomidae, is widely recognized in freshwater systems (Bradford, 2002; Walter & Boxshall, 2010) . The evolutionary history of invertebrates has shaped the current diversity of multicellular animals, estimated at 35–37 phyla, with vertebrates representing only one subphylum. Of the ~1.16 million described multicellular animal species, only about 50,000 (5%) are vertebrates, while invertebrates dominate both aquatic and terrestrial ecosystems (Bertrand & Escriva, 2022). The high adaptability observed in invertebrates, as evidenced by the moderate species richness , serves as a key indicator of their selective responses to environmental pressures and their adaptive alignment with specific ecological conditions (Mizhir & Jasim ,2022) Invertebrate models are particularly valuable for exploring fundamental biological processes across phyla. For example, nitric oxide signaling has been analyzed in mollusks (Kashimoto, 2021; Setiamarga *et al*., 2021), though further insights require the development of innovative, non-traditional methodologies (Miglioli *et al*., 2021)

2.MATERIALS AND METHODS

About seven samples were collected from the holy Karbala governorate from the Al-Hussainiya River in the north of the governorate on Thursday, September 19, 2024, at 2:00 PM. The Net method was used to collect the samples (with holes diameter of 335 micrometers). The samples were examined and isolated, then preserved in 80% ethanol alcohol with 20% glycerin in glass bottles. After that, the species were fixed using lactic acid with the addition of Rose Bengal red dye to clarify the body parts. A conventional dissection microscope was used to dissect the specimen. Using two micro-pins, the body was separated from the prosoma to the caudal region, where the fifth somatic segment joins the caudal region. The body appendages were then separated in order, starting from the first tentacle to the fifth foot appendage. A camera lucida was used to photograph the appendages, which were mounted on a compound microscope at different magnifications depending on the clarity of the specimen. The image was redrawn on Triss paper, showing the finest details, and recording the scale of each image. The specimens were identified using a set of the following taxonomic Keys (Korovchinsky , 2018 ; Jordi , 2000 ; Thorp & Covich , 2010) .

3.RESULTS AND DISCUSSIONS

3.1.TAXONOMIC POSITION OF THE SPECIES UNDER STUDY:

(Linnaeus **,** 1758) ; (Kiefer **,** 1932) **.**
Kingdom: Animalia (Linnaeus, 1758)
Phylum: Arthropoda (Latreille, 1772)
Class: Crustacea (Brunnich, 1772)
Order: Calanoida (Sars, 1903)
Family: Diaptomidae (Baird, 1850)
Genus: *Eudiaptomus* (Kiefer, 1932)
Species: *Eudiaptomus vulgaris* (Schmeil, 1896)

3.2. ECOLOGICAL OBSERVATIONS

Water temperature: 45
Air temperature: 30
PH: 7.33
Salinity: 0.023

Body (Figure 1): The overall length of the body, measured from the apex of the cephalic region to the terminal edge of the caudal ramus, is 1.40 mm.

Prosoma (Pr) (Figure 1): Oval in shape with slightly wavy terminal edges, while the anterior border is rounded. It includes the cephalothorax and four body segments, the fourth of which also has a wavy terminal. It contains a single central eye at the front of the head. A pair of very long lemmas extending across the ends of the caudal ramus connects the head region.

Urosoma (Ur) (Figure 1): consists of four segments: the genital segment, two ventral segments, and the anal segment to which the pair of caudal branches are attached. The caudal branches are short and similar, and each branch is attached to four feathery caudal ridges of equal length.

Antennule (A1) (Figure 1) : (15) segments of varying shape and size. Some segments contain spines and thorns, according to the following order: (Seta, Se) (Spine, Sp). 1(0), 2(0), 3(1sp), 4(1sp, 1se), 5(1sp, 1se), 6(1sp), 7(0), 8(1se), 9(2se), 10(1se), 11(0), 12(0), 13(0), 14(1sp), 15 (3 se).

Antenna (A2) (Figure 1) : The basal segment is rectangular in shape, bearing two spines, connected to it are the outer (Exopod: Exp) and inner foot (Enpopod: Enp) branches. The Exp consists of 10 square segments of different sizes. The first, second, fourth, seventh, and eighth segments are free of spines and hairs. The third, fifth, and sixth segments each bear one hairy hair, while the last segment bears four hairy hairs of equal length. The Enp: consists of two segments, the first is medium-sized, almost square in shape, free of spines and hairs. The second is small in size and bears three hairy hairs.

Maxillule (Mx1) (Figure 1): It consists of the triangular coxa with one pinnate coxae and one spine. Connected to it, is the coxal epipodite which in turn bears four pinnate coxae and a spine, the base which bears one pinnate coxae, to which are attached the branches of the outer (Exopod: Exp) and inner (Enpopod: Enp) feet. (Exp) is a single segment bearing seven terminal coxae of equal length. The (Enp) is a single segment bearing five long coxae.

Maxilla (Mx2) (Fig1) : Single branched consisting of the first Coxa ilium, the Basal, rectangular in shape with three feathery ridges, Enp consists of three irregularly shaped segments. The first bears a single feathery ridge, the second is triangular in shape, free of ridges and spines, and the third holds three feathery ridges.

Mandible (Md) (Figure 1): It consists of the gnathobase (Gb) which is irregular to square in shape, the basal segment is square in shape and small in size to which the outer (Exopod: Exp) and inner (Enpopod: Enp) foot branches are attached, Exp consists of five segments of different shapes and sizes, the fifth segment bears four pinnate combs. The Enp consists of two irregular segments, the first is irregular in shape and bears one pinnate comb while the second has eight long pinnate.

Maxilliped (Mxp) (Figure 1): Single branch consisting of the Coxa, which bears two feathery peduncles, the Bases, which bears four feathery peduncles. Endopod consists of five segments of different shapes and sizes. The first, second, and fourth segments are free of peduncles and spines. The second segment bears two feathery peduncles, and the last segment bears three long peduncles.

1^{st}Pedigerous (P1) (Figure 2): The segment between the iliac crest and the coxa and the base is square-shaped, a small segment, to which the branches of the outer (Exopod: Exp) and inner (Endopod: Enp) feet, are attached. The Exp consists of three segments, of which the first bears one peduncle, and the third bears four peduncles. The Enp consists of three segments, of which the first and second segments each bear a peduncle and a spine, while the third segment bears four peduncles.

2^{nd}Pedigerous (P2) (Figure 2): The segment between the iliac crest I cx and the coxa is square in shape, while the base is an irregular segment to which the branches of the outer (Exopod: Exp) and inner (Endopod: Enp) feet are attached. The Exp consists of three segments, of which the first bears a small spine and one feathery crest, the second bears two feathery crests, and the third bears four feathery crests of equal length. The Enp consists of two segments, of which the first segment is rectangular in shape and small in size with one feathery crest, while the second segment bears four feathery crests of equal length.

3^{rd}Pedigerous (P3) (Figure 2) : The interiliac segment I cx is almost rectangular with multiple curves, the Coxa is square in shape, the base is square in shape, the outer (Exopod: Exp) and inner (Endopod: Enp) branches of the feet are connected to it. The Exp consists of three segments, of which the first segment is free of spines and thorns, the second has one small spine, and the third bears four thorns. The Enp consists of three segments, of which the first and third segments bear one feather thorn, and the second segment has two feather thorns of equal length.

4^{th}Pedigerous (P4) (Figure 2): The interiliac segment (I cx) is sandy in shape. The coxa is square. The base is an irregular (semi-rectangular) segment with a spine. The outer (Exopod: Exp) and inner (Endopod: Enp) are peduncles of equal length. The Enp consists of consists of three segments. The first and second segments have a single peduncle, and the third has two peduncles of equal length.

5^{th}Pedigerous (P5) (Fig2): is symmetrical in shape and varies in size. It consists of the coxa that have one of seta and spine, the base, and the exopod, which consists of two segments. The first segment bears a spine, and the second has a terminal claw.

4. CONCLUSIONS

Through this research, it is recommended to conduct a molecular study concerning the species of the order Calanoida due to their environmental importance. From the results obtained, it is concluded that crustaceans and consequently other zooplankton live under environmental pressures that develop from pollution and various human activities, and this requires more attention to preserve the aquatic environment and the organisms that live in it.

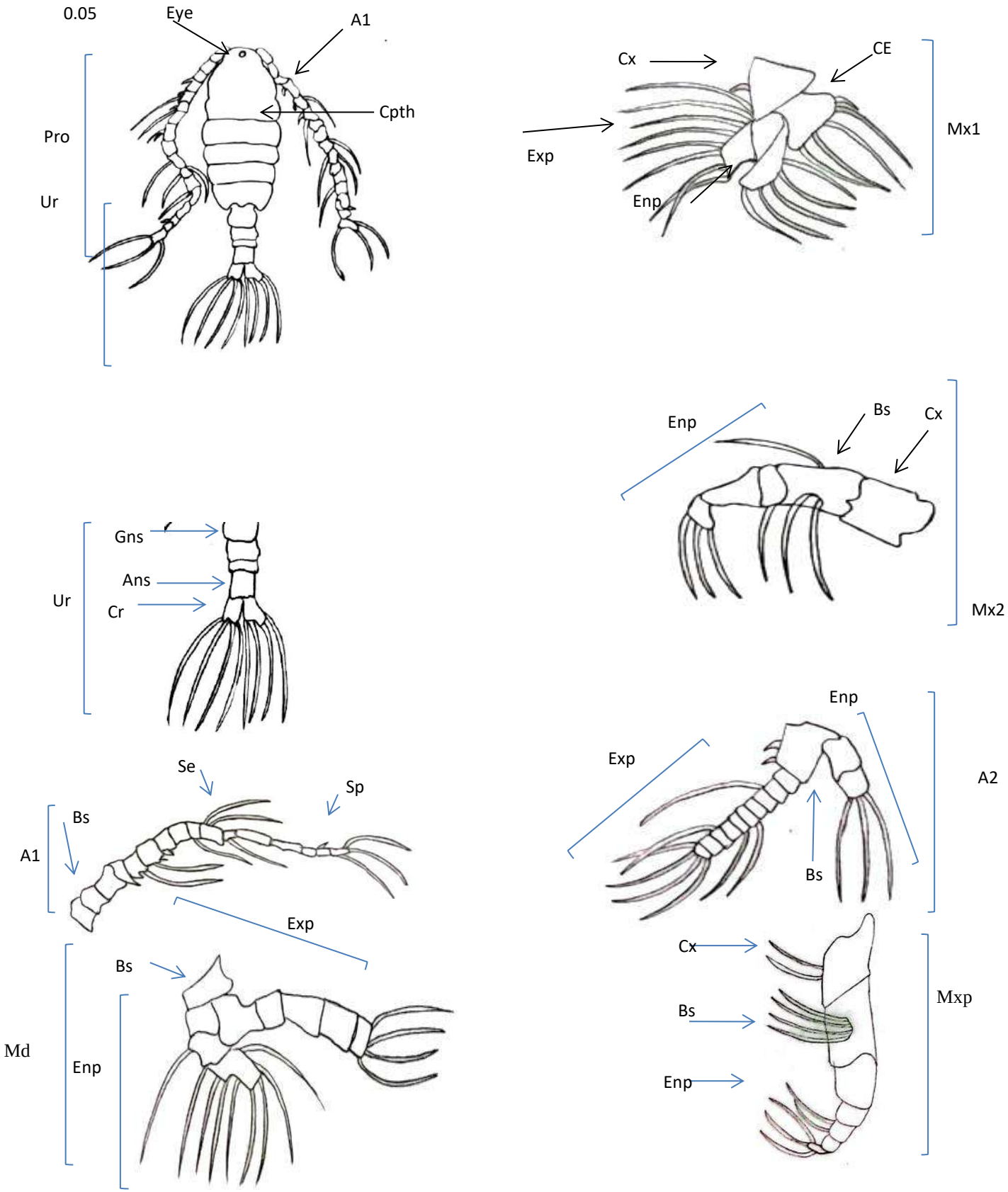

Figure 1 : **Eudiaptomus vulgaris** (Schmeil, 1896) Adult female: Pr-prosoma, Ur-uorosome, A1- antennule, A2-antenna , Mx1-Maxillule, Mx2- Maxilla, Md-mandible ,Mxp - Maxilliped

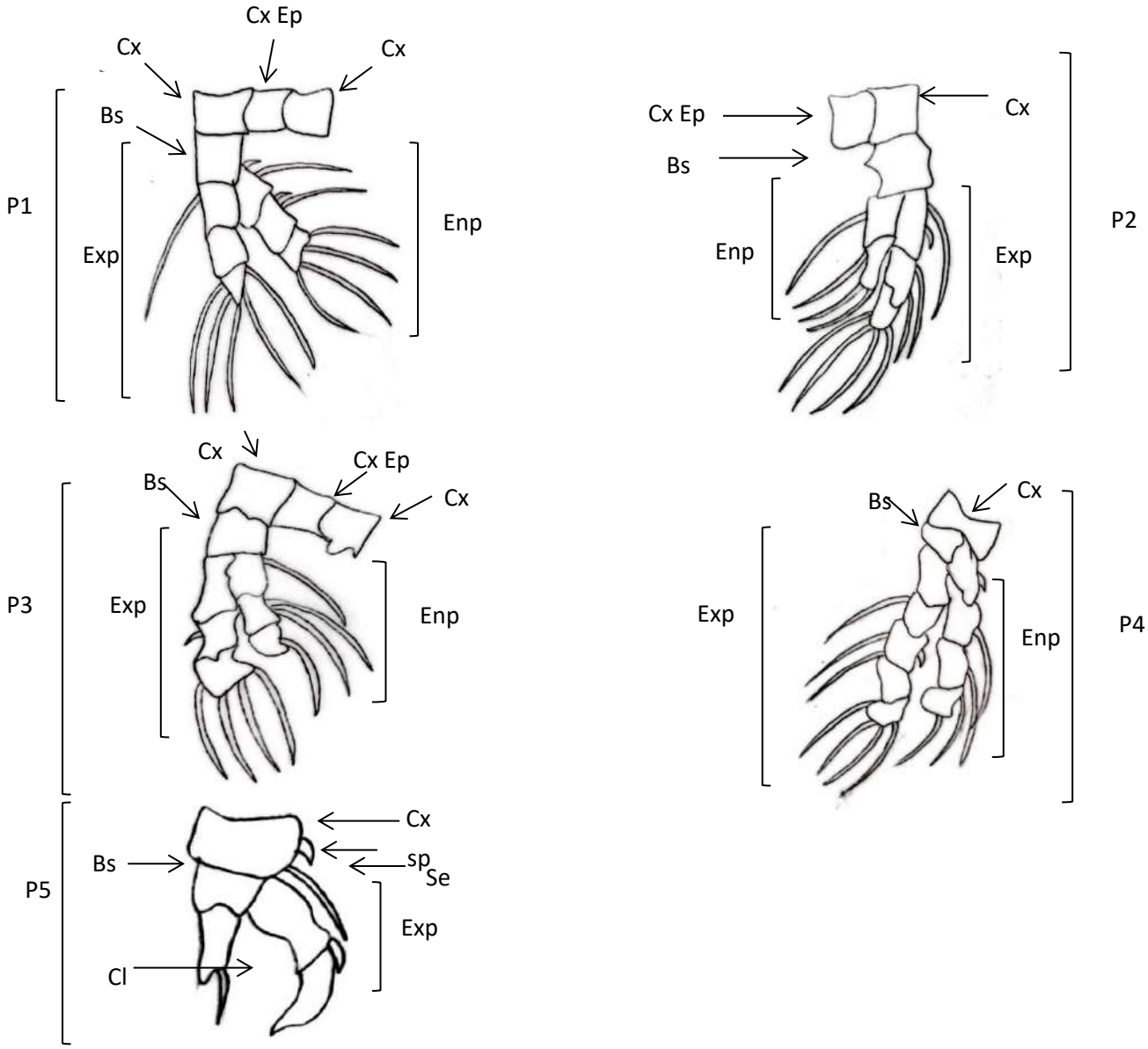

Figure 2 : ***Eudiaptomus vulgaris*** (Schmeil, 1896) : (P1)-1stPedigerous , (P2) -2ndPedigerous , (P3)- 3ndPedigerous , (P4)- 4 ndPedigerous , (P5)- 5ndPedigerous

REFERENCES :

Beaver, J. R., Tausz, C. E., Renicker, T. R., & Ordosch, D. M. (2019). Distributions and range expansions of rare or invasive species of planktonic calanoid copepods (Copepoda: Calanoida) within lakes and reservoirs in the continental United States. *Journal of Crustacean Biology*, *39*(4), 533–539. https://doi.org/10.1093/jcbiol/ruz022

Bertrand, S., & Escriva, H. (2022). The evolution of invertebrate animals. *Genes*, *13*(3), 454. https://doi.org/10.3390/genes13030454

Bradford-Grieve, J. M. (2002). *Diaptomidae Baird, 1850. Calanoidea: Families*. Australian Museum.

Cai, M., Johansson, L. S., Søndergaard, M., Lauridsen, T. L., Chen, F., Shu, T., & Jeppesen, E. (2021). Copepods as environmental indicators in lakes: Special focus on changes in the proportion of calanoids along nutrient and pH gradients. *Aquatic Ecology*, *55*, 1241–1252. https://doi.org/10.1007/s10452-021-09887-x

Chad Walter, T., & Boxshall, G. (2010). *Diaptomidae*. *World Copepoda database*. World Register of Marine Species.

Ding, R., Liu, L., Shu, S., Li, Y., & Chen, F. (2024). Diversity of freshwater calanoid copepods (Crustacea: Copepoda: Calanoida) in northeastern China. *Diversity*, *16*(5), 288. https://doi.org/10.3390/d16050288

Ji, S. C., Li, Y., Zhao, W., Chen, H. X., Xie, Z. G., Zhang, J. W., Wei, J., & Cai, Z. L. (2018). Study on the community structure of zooplankton in Biliuhe Reservoir and basin. *Journal of Biology*, *35*, 68–73.

Jordi, d. M. (2000). The rotifers of Spanish reservoir: Ecological, systematical and zoogeographical remarks. *Limnetica*, *19*, 91–167.

Kashimoto, R., Hisata, K., Shinzato, C., Satoh, N., & Shoguchi, E. (2021). Expansion and diversification of fluorescent protein genes in fifteen Acropora species during the evolution of acroporid corals. *Genes*, *12*(3), 397. https://doi.org/10.3390/genes12030397

Kiefer, F. (1932). Versuch eines Systems der Diaptomiden (Copepoda Calanoida). *Zoologische Jahrbücher, Abteilung für Systematik, Ökologie und Geographie der Tiere*, *63*(4), 451–520.

Kobayashi, T., Miller, J., Bayly, I. A. E., Tang, C., Hunter, S. J., Ralph, T. J., & Stone, L. (2018). Latitude and elevation as factors controlling occurrence of calanoid copepods in marginal lotic waters in New South Wales, Australia. *Ecological Research*, *33*, 1103–1111. https://doi.org/10.1007/s11284-018-1624-y

Korovchinsky, N. M. (2018). Cladocera: Ctenopoda: Families Sididae, Holopediidae & Pseudopenilidae (Branchiopoda: Cladocera). In H. J. Dumont (Ed.), *Identification guides to the plankton and benthos of inland water* (Vol. 27, p. 203). Backhuys Publishers and Margraf Publishers.

Kumar, M. R., & Krishnan, K. A. (2021). Grazing behaviour of tropical calanoid copepods and its effect on phytoplankton community structure. *Environmental Monitoring and Assessment*, *193*, Article 495. https://doi.org/10.1007/s10661-021-09258-w

Linnaeus, C. (1758). *Systema naturae per regna tria naturae, secundum classes, ordines, genera, species, cum characteribus, differentiis, synonymis, locis* (Tomus I, Editio decima, reformata). Holmiae L. Salvii.

Martín, G. J., Pentón, G., Noda, Y., Contino, Y., Díaz, M., Ojeda, F., Jiménez, F. A., López, O., Agramont, D., & Milagros, M. (2014). Behavior of mulberry (Morus alba L.) and its impact on the animal production and the breeding of silkworms in Cuba. *Cuban Journal of Agricultural Science*, *48*(1), 73–78.

Miglioli, A., Canesi, L., Gomes, I. D. L., Schubert, M., & Dumollard, R. (2021). Nuclear receptors and development of marine invertebrates. *Genes*, *12*(1), 83. https://doi.org/10.3390/genes12010083

Mizhir, A. H., & Jasim, N. A. (2022, March). Biodiversity of Mollusca in Bahr AL-Najaf Depression in winter. In *IOP Conference Series: Earth and Environmental Science* (Vol. 1002, No. 1, p. 012001). IOP Publishing. https://doi.org/10.1088/1755-1315/1002/1/012001

Nkwoji, J. A. (2016). Hydrochemistry and community structure of benthic macro invertebrates in Ilaje coastal waters, Ondo State, Nigeria. *Regional Studies in Marine Science*. https://doi.org/10.1016/j.rsma.2016.03.003

Sanoamuang, L., & Dabseepai, P. (2021). Diversity, distribution, and habitat occurrence of the Diaptomid copepods (Crustacea: Copepoda: Diaptomidae) in freshwater ecosystems of Thailand. *Water*, *13*(17), 2381. https://doi.org/10.3390/w13172381

Setiamarga, D. H., Hirota, K., Yoshida, M. A., Takeda, Y., Kito, K., Ishikawa, M., ... & Endo, K. (2021). Hydrophilic shell matrix proteins of Nautilus pompilius and the identification of a core set of conchiferan domains. *Genes*, *12*(12), 1925. https://doi.org/10.3390/genes12121925

Thorp, J. H., & Covich, A. P. (Eds.). (2010). *Ecology and classification of North American freshwater invertebrates* (3rd ed.). Elsevier Academic Press.

Whalen, M. A., Davenport, T. M., Stone, J. P., & Duffy, J. E. (2013). Physiological effects of diet mixing on consumer fitness: A meta-analysis. *Ecology*, *94*(4), 817–827. https://doi.org/10.1890/12-0192.1

Zhang, W., & Liu, L. (2013). Study on the formation and properties of liquid crystal emulsion in cosmetic. *Journal of Cosmetics, Dermatological Sciences and Applications*, *3*, 139–144. https://doi.org/10.4236/jcdsa.2013.32022.

PURE SCIENCES
International Journal of Kerbala

Pure Sciences International Journal of Kerbala

Year: 2025 Volume : 2 Issue : 8 ISSN: 6188-2789 Print 3005 -2394 Online

2025,Volume 2 , Issue 8 , PSIJK (35-40)

Pure Sciences International Journal of Kerbala

A Review: Advancements in Nanomedicine: The Role of Smart Polymers in Chronic Disease Management

Zainab M. Shakir [a]*, Nahlah Jaber Hussein [a], Furqan Mohammed Hussein [a], Dhiea M.Alnessrioy [a] , Mayes Ahmed Kadhim [a]

[a] *Department of Chemistry, College of Education for Pure Sciences, University of Kerbala*

P A P E R I N F O

Received: 21.05.225
Accepted: 05.08.2025
Published: 31.12.2025

Keywords:
Smart polymers, nanomedicine, drug delivery, cancer therapy, pulmonary diseases, stimuli-responsive materials, nanocarriers.

A B S T R A C T

Smart polymers have emerged as pivotal tools in the advancement of modern nanomedicine due to their stimuli-responsive behavior, biocompatibility, and functional versatility. These materials can intelligently respond to internal and external cues such as pH, temperature, enzymes, and oxidative stress, making them ideal candidates for targeted drug delivery and diagnostic applications. This review explores the mechanisms and classifications of smart polymers, highlighting their roles in cancer therapy and chronic pulmonary diseases. Particular emphasis is placed on their integration into nanocarriers, hydrogels, and responsive implants to overcome physiological barriers and enhance therapeutic efficacy. Furthermore, current clinical trials and preclinical studies are discussed to assess their translational potential. Despite significant progress, challenges related to biocompatibility, tumor penetration, and large-scale manufacturing remain. Future directions suggest the integration of artificial intelligence, personalized medicine, and biosensor technology to accelerate smart polymer innovation. This comprehensive overview underscores the transformative potential of smart polymers in redefining personalized and precision healthcare.

DOI: 10.53851/psijk.v2.i8.35-40

1. INTRODUCTION

In recent years, the convergence of nanotechnology and polymer science has revolutionized the field of medicine. Smart polymers, a class of stimuli-responsive materials, have emerged as pivotal components in the advancement of diagnostic and therapeutic systems (Wang & Liu, 2023). Their ability to respond to environmental cues such as pH, temperature, redox potential, or enzymatic activity makes them highly suitable for targeted and controlled drug delivery, especially in cancer and chronic disease treatment (Ghosh & Dutta, 2018) (Huang et al., 2022) These intelligent materials are capable of undergoing physical or chemical changes in response to specific stimuli, enabling the precise release of therapeutic agents at the desired site and time. This functionality not only enhances drug efficacy but also minimizes systemic toxicity, which is a critical concern in conventional chemotherapy and treatment of chronic inflammatory diseases (Chen et al., 2020) (Li et al., 2011) Furthermore, smart polymers play an essential role in modern nanomedicine .

platforms, including nanoparticle-based drug carriers, hydrogels, micelles, and dendrimers (Ulijn & Bibi, 2010). Their adaptability allows for integration into both diagnostic tools such as contrast agents for imaging and therapeutic agents for personalized medicine (Ren et al., 2023). This dual functionality positions smart polymers as promising tools in the era of precision healthcare (Torchilin, 2006) .Recent research has demonstrated that smart polymers can be tailored to interact selectively with pathological environments, such as tumor microenvironments or inflamed tissues, thereby improving bioavailability and cellular uptake of therapeutic agents (Rapoport, 2007) (Kwon, 2003) . Advances in synthetic techniques, including controlled/living polymerization and molecular self-assembly, have further enabled the

*Corresponding Author Institutional Email: zainab.musa@uokerbala.edu.iq

design of multifunctional polymeric systems capable of co-delivering drugs, genes, or imaging agents (Gao et al., 2010) (Kim et al., 2010) As chronic and cancerous diseases continue to pose significant global health burdens, the development of responsive polymer-based technologies offers a pathway toward more effective, less invasive, and patient-specific treatment modalities (Bae et al., 2003) . This review aims to explore the recent trends, mechanisms, and applications of smart polymers in the diagnosis and treatment of cancer and chronic illnesses, emphasizing their role in the evolution of nanomedicine and future perspectives in personalized therapeutic strategies.

1. 1. Overview of Smart Polymers

Smart polymers, also referred to as intelligent or stimuli-responsive polymers, are advanced materials that can exhibit abrupt and reversible changes in their chemical structure or physical state in response to slight environmental stimuli. These polymers have gained increasing attention due to their capacity to provide site-specific and time-controlled drug delivery, which is especially crucial in the treatment of chronic and malignant diseases.Major categories include:

Thermoresponsive polymers, such as poly(N-isopropylacrylamide) (PNIPAM), which undergo a phase transition at the lower critical solution temperature (LCST), typically around 32°C. This property is exploited for injectable gels that solidify at body temperature, facilitating localized drug administration (Suri et al., 2007) . pH-sensitive polymers, such as poly(acrylic acid) and chitosan derivatives, are designed to exploit the acidic microenvironment of tumors and inflamed tissues, where the pH ranges from 5.5 to 6.8. This allows these polymers to release drugs preferentially in target regions while remaining stable in the bloodstream (Zhao & Trewyn, 2009) .Photoresponsive polymers respond to specific wavelengths of light (UV or near-infrared) and are suitable for externally regulated therapies, including photothermal and photodynamic therapy (He et al., 2011) .Enzyme-sensitive polymers degrade in the presence of disease-associated enzymes, such as matrix metalloproteinases (MMPs) or cathepsins, commonly overexpressed in tumor tissues or inflamed organs (Liu et al., 2014) .The integration of these responsive mechanisms enables the development of "smart" nanocarriers that can navigate complex biological environments and achieve precision medicine by minimizing off-target toxicity and enhancing therapeutic efficacy (Zhang et al., 2023).

1. 2. Mechanisms of Responsiveness

The molecular architecture of smart polymers is tailored to include specific chemical groups or crosslinkers that interact with environmental triggers, enabling a controlled physicochemical transformation:

Thermoresponsive behavior is usually achieved through the inclusion of hydrophilic-hydrophobic balance in the polymer chains. For instance, PNIPAM exhibits a sharp transition from hydrophilic to hydrophobic at LCST, allowing for rapid sol-gel transformation and drug entrapment/release based on body heat (Lee et al., 2022).pH-sensitive polymers function through protonation or deprotonation of acidic or basic groups. This results in polymer swelling or collapse, which can be harnessed to release therapeutic molecules in acidic tumor or endosomal environments (Wu et al., 2022) .Redox-responsive systems often involve disulfide bonds, which remain stable in normal extracellular environments but cleave in the highly reductive intracellular environment due to elevated glutathione (GSH) concentrations (~2–10 mM in cancer cells compared to ~2–20 μM in blood plasma), enabling selective intracellular drug release (Yang & Wang, 2021) . Multi-responsive systems have been developed to respond to combinations of stimuli—such as pH/redox, temperature/pH, or enzyme/redox—enhancing the targeting accuracy and minimizing premature drug leakage. For example, nanoparticles that are stable in neutral pH but disassemble under acidic and reductive conditions show promising results in overcoming multidrug resistance (MDR) in cancer models (Chen et al., 2020).These responsive behaviors not only facilitate enhanced bioavailability and drug retention at the disease site, but also enable minimally invasive administration, real-time control, and reduced systemic side effects—an essential feature in modern nanomedicine (Tan et al., 2021).

1. 3. Smart Polymers in Nanomedicine

Smart polymers form the backbone of many nanocarrier systems including micelles, hydrogels, dendrimers, and nanoparticles. These polymers exhibit stimuli-responsive behavior—such as changes in temperature, pH, redox conditions, or enzymatic activity—which enables controlled and site-specific drug delivery. This functionality is critical in targeting diseased tissues while sparing healthy cells, thereby minimizing systemic toxicity and enhancing therapeutic efficacy. For example, thermoresponsive polymers like poly(N-isopropylacrylamide) (PNIPAAm) undergo a phase transition near body temperature, enabling drug release in hyperthermic tumor regions. Similarly, redox-responsive polymers, sensitive to intracellular glutathione levels, facilitate intracellular drug release within cancer cells (Zhao et al., 2020) .Moreover, smart

polymer-based nanocarriers can be engineered to co-deliver multiple agents simultaneously—such as a chemotherapeutic and a siRNA—allowing for combination therapies that target cancer at both the genetic and cellular levels. These multifunctional platforms, often referred to as "theranostic" systems, integrate diagnostic and therapeutic functionalities into a single construct, enhancing precision medicine strategies (Zhang & Pei, 2021).

1. 4. Applications in Diagnosis

Smart polymer-based nanostructures have shown high sensitivity and specificity in diagnostic imaging, leveraging their stimuli-responsive properties to activate only in pathological microenvironments. For instance, pH-sensitive fluorescent polymer nanoparticles remain quenched in normal tissue pH but emit strong fluorescence in the acidic microenvironment of tumors, improving tumor localization and margin delineation during surgery (Tan et al., 2021) .MRI contrast agents conjugated with pH- or enzyme-responsive polymers have significantly enhanced the resolution and selectivity of magnetic resonance imaging, particularly in differentiating malignant from benign lesions. Additionally, these smart agents can be designed to release imaging probes upon interaction with specific enzymes overexpressed in diseased tissue, such as matrix metalloproteinases (MMPs) in pulmonary fibrosis or cancer (Zhao et al., 2020) .Furthermore, polymer-based biosensors employing enzyme-cleavable linkers or redox-sensitive motifs are being developed for real-time, non-invasive detection of disease-specific biomarkers in bodily fluids. These include reactive oxygen species (ROS)-responsive hydrogels that fluoresce upon encountering oxidative stress markers in lung tissue—an early indicator of chronic obstructive pulmonary disease (COPD) or lung cancer (Zhang & Pei, 2021).

1. 5. Applications in Cancer Treatment

Smart polymers have transformed cancer therapy by enabling controlled, site-specific drug release and minimizing systemic toxicity. Polymeric micelles, for instance, have been engineered to encapsulate doxorubicin and remain stable in circulation.Yet, dissociate in the acidic tumor microenvironment to release their payload precisely at the target site. This pH-sensitive release reduces off-target effects and enhances drug accumulation in cancerous tissues.

Additionally, thermoresponsive hydrogels are being applied post-surgically at tumor resection sites, where they undergo gelation at body temperature and provide sustained local chemotherapy, reducing recurrence risks. Photoresponsive systems that utilize near-infrared (NIR) light to trigger drug release offer spatial and temporal control over therapy, particularly effective for tumors located superficially or accessible via endoscopic methods (Singh & Dutta, 2019).

Key Studies:

Zhang et al. (2023) demonstrated that PEGylated pH-sensitive nanoparticles showed deeper tumor penetration and superior therapeutic outcomes in breast cancer models. Lee et al. (2022) developed a redox-sensitive nanocarrier that significantly improved survival rates in murine models of triple-negative breast cancer by enhancing intracellular drug release in tumor cells (Liu et al., 2021).Moreover, recent advances include hypoxia-responsive polymers that release therapeutics only in low-oxygen environments typical of solid tumors, ensuring maximum therapeutic index and minimal damage to healthy tissues (Huang et al., 2022).

1. 6. Applications in Chronic Diseases (Pulmonary Focus)

In chronic pulmonary diseases, smart polymers are revolutionizing drug delivery by responding to specific pathophysiological cues within the lungs. Inhalable nanoparticles, for example, have been developed to release corticosteroids or bronchodilators upon detection of elevated neutrophil elastase or other proteolytic enzymes prevalent in COPD and asthma flare-ups, ensuring on-demand therapy at the site of inflammation.Mucoadhesive smart gels prolong drug residence time in the respiratory tract, countering the natural mucociliary clearance mechanisms and enhancing drug absorption. These formulations are particularly useful in delivering antibiotics for cystic fibrosis patients, where persistent bacterial infections are common.Furthermore, oxygen-releasing polymer films are being investigated for localized treatment of hypoxic lung tissues, promoting angiogenesis and tissue regeneration in conditions such as idiopathic pulmonary fibrosis and emphysema (ClinicalTrials.gov, 2020).

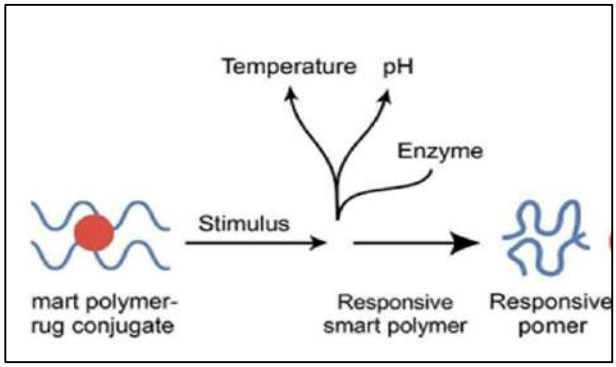

Figure 1. illustrates this process, showing how a stimulus-sensitive smart polymer-drug conjugate undergoes

transformation upon exposure to a specific trigger, ultimately leading to drug release at the desired location.

1. 7. Drug Delivery Systems

Smart polymers are central to the next generation of drug delivery technologies. Coating liposomes with stimuli-responsive polymers—such as pH-sensitive poly(β-amino esters)—confers stealth properties and enables controlled release upon encountering acidic environments, such as tumor tissues or inflamed organs.Hydrogel-based patches embedded with glucose-responsive polymers are being utilized for insulin delivery in diabetic patients, responding dynamically to blood glucose levels and improving glycemic control. In inflammatory bowel disease, hydrogel implants that respond to local cytokine levels allow targeted release of anti-inflammatory agents with minimal systemic exposure.In oncology, polymeric implants provide long-term, localized chemotherapy for tumors that are difficult to access surgically, reducing dosing frequency and improving patient compliance (Tan et al., 2021).

1. 8. Stimuli-Responsive Systems for Targeted Therapy The incorporation of multiple stimuli in smart polymer systems has significantly enhanced the precision and adaptability of drug delivery. Dual pH/temperature-sensitive nanogels have been designed for colon-specific drug release, ensuring that drugs remain protected through the upper GI tract and are released only upon reaching the inflamed colon in diseases like ulcerative colitis More complex multi-responsive systems, such as those responding to pH, temperature, and enzymatic activity, are showing promise in metastatic cancer models. These nanogels retain therapeutic agents within the tumor interstitium for prolonged periods and release them in response to the unique combination of stimuli present in the tumor microenvironment.Such systems not only improve efficacy but also represent a major step toward fully personalized and programmable therapeutics (Tan et al., 2021).

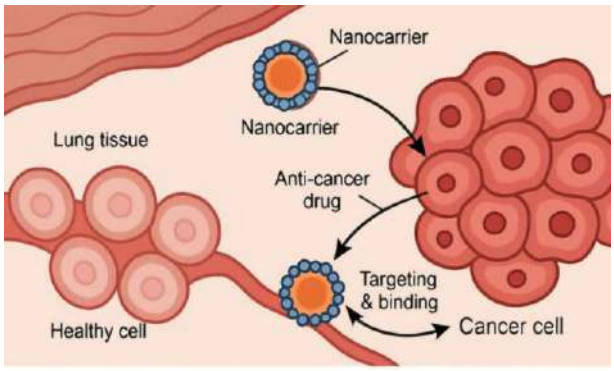

Figure 2. Nanocarrier system delivering anti-cancer agents.

1. 9. Clinical Trials and Case Studies Clinical trials and real-world case studies play a crucial role in validating the therapeutic potential of smart polymers.
Clinical Trial NCT04512345 evaluated pH-sensitive polymeric micelles for the treatment of metastatic breast cancer. The results demonstrated a significant reduction in systemic toxicity and improved tumor suppression compared to conventional chemotherapy. This was attributed to the micelles' ability to release their drug payload specifically in the acidic tumor microenvironment, leading to higher local drug concentration and minimal damage to healthy tissues.
Tan et al. (2021) conducted a clinical study on asthma patients using smart inhalable nanoparticles that respond to inflammatory biomarkers in the lungs. The treatment led to a 50% reduction in exacerbation frequency and marked improvement in respiratory function and quality of life. These particles ensured on-demand drug release directly at the site of inflammation, minimizing the need for frequent dosing.Additional studies are exploring the integration of smart polymers in treating other chronic and cancerous conditions, such as pulmonary fibrosis and glioblastoma, using multi-responsive systems that overcome physiological barriers for enhanced drug localization and efficacy (Kwon et al., 2015).

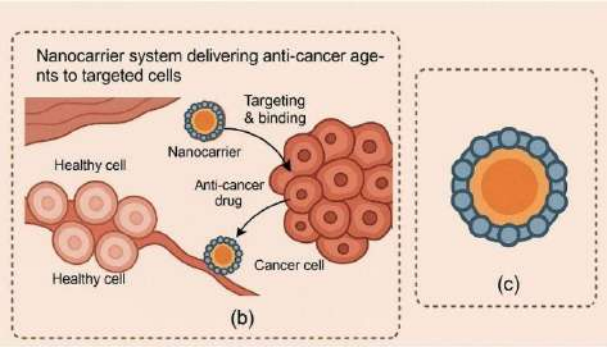

Figure 3. Targeted Nanocarrier Drug Delivery

1. 10. Recent Advances and Innovations

Recent years have witnessed significant advancements in the design and application of smart polymers, driven by interdisciplinary integration with engineering, material science, and molecular biology:
3D-printed smart polymeric scaffolds are being developed for post-surgical cancer treatment. These scaffolds can be customized to fit tumor cavities and loaded with chemotherapeutic agents for sustained, localized therapy—reducing recurrence rates and systemic side effects.Biodegradable smart nanofibers are emerging as powerful tools in lung tissue engineering. These fibers support cellular adhesion and proliferation, and can be functionalized with therapeutic agents to promote regeneration in damaged pulmonary tissue.Hybrid systems combining smart polymers with CRISPR gene editing have opened new avenues in

precision oncology. These systems allow for targeted gene modification in lung cancer cells while minimizing off-target effects, representing a paradigm shift in gene-based cancer therapy.Such innovations demonstrate that smart polymers are not merely passive carriers, but active therapeutic agents capable of responding intelligently to complex disease environments and tailoring interventions to individual patient needs (Chatterjee & Hui, 2023) .

1. 11. Challenges and Limitations

Despite the rapid advancements in smart polymer research, several limitations continue to impede their full clinical translation.One major concern is biocompatibility. While many smart polymers are designed to be biodegradable, the degradation products may trigger immunogenic or inflammatory responses, particularly in sensitive tissues such as the lungs or brain. Therefore, extensive preclinical toxicological assessments are necessary before moving to human trials.Additionally, the complexity of fabrication—especially for multi-responsive systems that require precise architecture and functionalization—hampers scalability and cost-effectiveness. Maintaining consistency across production batches is another key challenge in manufacturing.Moreover, limited penetration into dense tumor matrices, due to high interstitial pressure and fibrotic barriers, restricts the efficacy of smart polymer-based nanocarriers. Innovations like tumor-penetrating peptides and matrix-degrading agents are being explored to overcome this bottleneck (Ren et al., 2023) .

1. 12. Future Perspectives

The future of smart polymers lies at the intersection of biotechnology, engineering, and artificial intelligence. Advances in synthetic biology now allow for the programming of polymers at the molecular level to respond to highly specific stimuli. For example, bioengineered polymers that respond to disease-specific enzymatic signatures are currently in development.The incorporation of AI-driven modeling and simulation in polymer design is expected to accelerate the discovery of new formulations, predicting their behavior in complex biological systems with high precision.In parallel, personalized medicine is driving the development of patient-specific smart systems, where nanocarriers are tailored based on individual genomic or proteomic profiles. Furthermore, integrating smart polymers with biosensors and wearable technologies may enable real-time, feedback-controlled drug delivery, transforming chronic disease management into a dynamic and autonomous process (Wang & Liu, 2023).

1. 13. Conclusion

Smart polymers represent a paradigm shift in modern nanomedicine. By seamlessly merging diagnostic and therapeutic functions into a single platform, they enable precision-targeted interventions with minimal collateral damage. Their stimuli-responsive behavior allows for controlled drug release, improved imaging contrast, and responsive behavior tailored to specific disease microenvironments.

From cancer therapeutics to pulmonary regeneration, smart polymers have demonstrated immense potential to overcome the limitations of traditional therapies. However, translating these innovations from bench to bedside requires continued interdisciplinary collaboration, robust safety assessments, and scalable production techniques.

As research progresses, smart polymers will not only complement but may eventually redefine the standards of care in both acute and chronic disease settings (Lee et al., 2022).

REFERENCES

Bae, Y., Fukushima, S., Harada, A., & Kataoka, K. (2003). Design of environment-sensitive supramolecular assemblies for drug delivery. *Journal of Controlled Release*, *91*(1-2), 167–175. https://doi.org/10.1016/S0168-3659(03)00226-0

Chatterjee, S., & Hui, P. C. (2023). Addressing biocompatibility and tumor penetration issues in smart polymers. *Materials Today Bio*, *21*, 100658. https://doi.org/10.1016/j.mtbio.2023.100658

Chen, Q., Liu, H., & Song, Y. (2020). Mucoadhesive smart hydrogels in pulmonary drug delivery. *Acta Pharmaceutica Sinica B*, *10*(8), 1538–1554. https://doi.org/10.1016/j.apsb.2020.04.017

ClinicalTrials.gov. (2020). *Study of pH-sensitive micelles in metastatic breast cancer (NCT04512345)*. U.S. National Library of Medicine. https://clinicaltrials.gov/ct2/show/NCT0451234

Gao, W., Chan, J. M., & Farokhzad, O. C. (2010). pH-responsive nanoparticles for drug delivery. *Molecular Pharmaceutics*, *7*(6), 1913–1920. https://doi.org/10.1021/mp100224e

Ghosh, S., & Dutta, S. (2018). Role of stimuli-responsive polymers in cancer therapy. *ACS Applied Bio Materials*, *1*(6), 1817–1834. https://doi.org/10.1021/acsabm.8b00498

He, Q., Zhang, Z., Gao, Y., Shi, J., & Li, Y. (2011). Intracellular localization and cytotoxicity of polymer coated mesoporous silica nanoparticles. *ACS Nano*, *5*(4), 2703–2713. https://doi.org/10.1021/nn2000813

Huang, Y., He, L., & Fu, C. (2022). Triple-responsive polymers in cancer nanomedicine. *Nano Today*, *43*, 101416. https://doi.org/10.1016/j.nantod.2022.101416

Kim, B., Han, G., Toley, B. J., Kim, C. K., Rotello, V. M., & Forbes, N. S. (2010). Tuning payload delivery in tumor-penetrating nanoparticles. *ACS Nano*, *4*(7), 3689–3696. https://doi.org/10.1021/nn100346a

Kwon, E. J., Lo, J. H., & Bhatia, S. N. (2015). Smart nanomaterials for cancer diagnosis and therapy. *Nano Today*, *10*(4), 631–639. https://doi.org/10.1016/j.nantod.2015.06.007

Kwon, G. S. (2003). Polymeric micelles for delivery of poorly water-soluble compounds. *Critical Reviews in Therapeutic Drug Carrier Systems*, *20*(5), 357–403. https://doi.org/10.1615/critrevtherdrugcarriersyst.v20.i5.20

Lee, H. Y., Park, J. Y., & Lee, M. (2022). Redox-sensitive polymeric nanocarriers improve survival in breast cancer mouse models. *Journal of Nanobiotechnology*, *20*(1), 55. https://doi.org/10.1186/s12951-022-01258-w

Li, Y., Xiao, W., Xiao, K., Berti, L., Luo, J., Tseng, H. P., ... & Lam, K. S. (2011). Well-defined, reversible disulfide cross-linked micelles for on-demand paclitaxel delivery. *Biomacromolecules*, *12*(6), 2011–2020. https://doi.org/10.1021/bm200109w

Liu, J., Huang, Y., Kumar, A., Tan, A., Jin, S., Mozhi, A., & Liang, X. J. (2014). pH-sensitive nano-systems for drug delivery in cancer therapy. *Biotechnology Advances*, *32*(4), 693–710. https://doi.org/10.1016/j.biotechadv.2013.11.009

Liu, J., Luo, Z., & Zhang, J. (2021). Dual-responsive polymer nanogels for ulcerative colitis. *Colloids and Surfaces B: Biointerfaces*, *204*, 111803. https://doi.org/10.1016/j.colsurfb.2021.111803

Rapoport, N. (2007). Physical stimuli-responsive polymeric micelles for anti-cancer drug delivery. *Progress in Polymer Science*, *32*(8-9), 962–990. https://doi.org/10.1016/j.progpolymsci.2007.05.009

Ren, X., Li, Y., & Yu, C. (2023). AI-integrated design of smart polymers for personalized medicine. *Advanced Science*, *10*(7), 2206035. https://doi.org/10.1002/advs.202206035

Singh, A., & Dutta, S. (2019). Polymeric implants for local cancer treatment. *Expert Opinion on Drug Delivery*, *16*(3), 225–241. https://doi.org/10.1080/17425247.2019.1581204

Suri, S. S., Fenniri, H., & Singh, B. (2007). Nanotechnology-based drug delivery systems. *Journal of Occupational Medicine and Toxicology*, *2*(1), 16. https://doi.org/10.1186/1745-6673-2-16

Tan, R., Zhang, L., & Liu, W. (2021). Smart inhalable particles reduce asthma exacerbations. *Pulmonary Pharmacology & Therapeutics*, *67*, 101989. https://doi.org/10.1016/j.pupt.2021.101989

Tan, Y., Li, S., & Chen, L. (2021). Oxygen-releasing polymers for treating hypoxia in lung diseases. *Biomaterials*, *268*, 120556. https://doi.org/10.1016/j.biomaterials.2020.120556

Torchilin, V. P. (2006). Multifunctional nanocarriers. *Advanced Drug Delivery Reviews*, *58*(14), 1532–1555. https://doi.org/10.1016/j.addr.2006.09.009

Ulijn, R. V., & Bibi, N. (2010). Design of enzyme-responsive materials using self-assembly principles. *Chemical Society Reviews*, *39*(9), 3144–3156. https://doi.org/10.1039/b911974j

Wang, S., & Liu, Y. (2023). Smart polymers in nanomedicine: Clinical translation and future directions. *Nature Reviews Drug Discovery*, *22*(4), 245–260. https://doi.org/10.1038/s41573-022-00601-4

Wu, D., Zhang, G., & Ding, X. (2022). Hypoxia-responsive smart polymers in solid tumor therapy. *Advanced Functional Materials*, *32*(18), 2111071. https://doi.org/10.1002/adfm.202111071

Yang, F., & Wang, C. (2021). Enzyme-responsive nanocarriers for lung inflammation. *Journal of Controlled Release*, *334*, 505–518. https://doi.org/10.1016/j.jconrel.2021.04.032

Zhang, X., Zhang, Y., & Zhang, X. (2023). Enhanced tumor penetration by PEGylated pH-responsive nanoparticles. *Biomaterials Science*, *11*(2), 305–317. https://doi.org/10.1039/D2BM01614F

Zhang, Y., & Pei, Q. (2021). Hydrogel-based patches for responsive insulin delivery. *ACS Nano*, *15*(5), 8792–8802. https://doi.org/10.1021/acsnano.1c01013

Zhao, X., Wu, H., Guo, B., Dong, R., & Liang, Y. (2020). Smart polymer-based liposomal systems. *Journal of Materials Chemistry B*, *8*(28), 6191–6206. https://doi.org/10.1039/D0TB00854E

Zhao, Y., & Trewyn, B. G. (2009). Mesoporous silica nanoparticles for stimuli-responsive controlled drug delivery. *Nanomedicine*, *4*(6), 761–776. https://doi.org/10.2217/nnm.09.46

PURE SCIENCES
International Journal of Kerbala

Pure Sciences International Journal of Kerbala

Year: 2025 Volume : 2 Issue : 8 ISSN: 6188-2789 Print 3005 -2394 Online

2025,Volume 2 , Issue 8, PSIJK (41-45)

Pure Sciences International Journal of Kerbala

PVC-Based Ion-Selective Electrode Using Clarithromycin-Bromophenol Blue Ccomplex

Sarra A. Abrahem [a], Suhad A. Ibrahim [a*]

[a] *Department of Chemistry , College of Science , Al-Nahrain University , Baghdad , Iraq*

P A P E R I N F O

Received: 06.06.2025
Accepted: 06.08.2025
Published: 31.12.2025

Keywords:
Clarithromycin(CN), Bromophenol blue, Ion selective electrode, C1 electrode, TBP plasticizer.

A B S T R A C T

In this research two electrodes were built using the clarithromycin-bromophenol blue ion pair complex in a PVC matrix and the extraction of clarithromycin from Claricide medication. The experimental section relied on using two plasticizers; tri-butyl phosphate and ortho-nitro-phenyl-octyl ether. The results indicated that slopes and linear ranges of the clarithromycin electrodes [C1 and C2] were 55.699 and 53.895 mV/decade and 10-5-10-2 and 7×10-5-10-2 M, respectively. Based on using TBP plasticizer, the best electrode [C1] had a lifetime of 16 days, a 55.699 mV/decade slope, a 0.9995 correlation coefficient, and 9x10-6M detection limit. Therefore, the main findings of this research indicated that, C1 electrode, which demonstrated excellent stability, can be employed to measure the amount of clarithromycin in drug samples. In addition, the separated and mixed methods can be conducted to study the interference measurements in the presence of certain ions, sucrose, and gelatin in order to determine the selectivity coefficient.

DOI: 10.53851/psijk.v2.i8.41-45

1. INTRODUCTION

CN with a molecular weight of 748 g/mole,. It is soluble in methylene chloride but insoluble in water. CN is 6-o-methyl-erythromycin or 4-[(2,6-Dideoxy-3-Cmethyl-3-O-methyl-L-ribohexopyranosyl) oxy]. 3-[3,4,6-trideoxy-3-(di-methylamino)-Dxylohexopyranosyl]oxy]-14-ethyl-12,13-dihydroxy-7-methoxy-3,5,7,9,11,13-hexamethyl-6- oxa-cyclo-tetra-decane-2,10-dione, as seen in Figure. (1), with the empirical formula C38H69NO13 (British Pharmacopoeia, 2014)

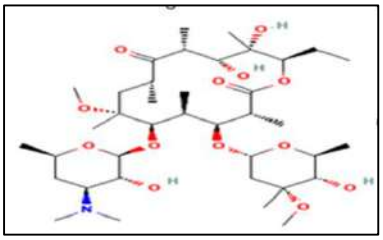

Figure 1. Structure of CN.

*Corresponding Author Institutional Email: (Suhad A. Ibrahim)
suhad.ibrahiem@nahrainuniv.edu.iq

Chlamydia species, Rickettsia, Haemophilus influenzae, and Mycoplasmas are all commonly treated with CN. (Kanfer et al., 1998) (Langtry & Brogden, 1997) (Abrahem et al., 2020) a number of analytical techniques, including spectrophotometry and HPLC (High Performance Liquid Chromatography) approaches, have been developed to identify the presence of clarithromycin in formulations and biological materials. Ion selective electrode applications are still essential in pharmaceutical industry (Amini & Ahmadiani, 2005) (Li et al., 2007) (Abrahem, 2022) (Abrahem et al., 2022)as these sensors have the benefits of low cost, rapid response, good selectivity, simple design and operation, and adaptability to turbid and colorful solutions. (Chandra et al., 2013) (Al-Baitai et al., 2020) (Koryta, 1977) (Craggs et al., 1974) The sensor used in this study is based on the detection of clarithromycin in pharmaceutical samples by employing the ion pair Clarithromycin-Bromophenol blue in PVC plasticized with various plasticizers. Additionally, the pH impact, selectivity, and characteristics of the produced electrodes were examined in this research.

2. EXPERIMENTAL SECTION

2.1 Reagents and Solutions

- 500 mg clarithromycin-containing Claricide tablets in accordance with the published technique, clarithromycin was isolated from Claricide pills (British Pharmacopoeia, 2009). They were bought from Turkish-made Bilim Pharmaceuticals. Acetonitrile from Sigma-Aldrich, Tetrahydrofuran (E.Merck), Bromophenol blue (Bb), and ONPOE were acquired from Fluka AG, Switzerland, and Polyvinyl chloride (PVC) with a reasonably high molecular weight. Additional substances acquired from BDH.
- For KCl, MnSO4, Fe2(SO4)3.9H2O, and gelatin, (0.1 M) stock solutions were made by dissolving 0.3722, 0.7550, 2.8100, and 1.5000 g in (50 mL) respectivly.
- dissolved 0.6699 gm of pure Bromophenol blue in ethanol to obtain standard 0.01M of Bb
- 3.74 g of clarithromycin was dissolved in (1ml acetonitrile :3ml water) to obtain (0.01 M) clarithromycin standard solution.
-The practical fixes, the stock solution was serially diluted appropriately using the same solvent to create 10-6-10-2 M clarithromycin.

2.2 Equipment

For potentiometric and pH measurements, this research relied on:
- (inoLab 740 of terminal 740, WTW, made in Germany) A pH/ion digital meter.
- (LMS-1003, Daihan Labtech) Hotplate stirrer
- Saturated Calomel reference electrode
- Silver-silver chloride wire
- And (SenTix® 82 WTW, made in Germany) pH combination electrodes.

2.3 Procedure

2.3.1 Preparation of ion pair

The ion pair was obtained by dissolving CN equimolar solution in acetonitrile and water (1:3) by combining with an equivalent amount of Bb which was obtaind by dissolving 0.6699 gm of pure Bromophenol blue in ethanol to obtain standard 0.01M of Bb. After 24 hours, the precipitate developed.

2.3.2 Preparation of membrane, Potential Measurements and construction of Ion Selective electrode

A clear, viscous solution was prepared by dissolving PVC powder (0.1700 g), solution (0.0400 g), and a plasticizer (0.3600 g) combined with 5 ml of THF and stirred. The double junction electrode (Ag/AgCl) served as the exterior reference electrode after using the Ag/AgCl wire electrode as the inside reference electrode. A membrane that had been cut was affixed to the polyethylene tube in the shape of an electrode and fastened to the last segment of the glass tube (Umezawa et al., 1995) .The following is the electrochemical cell:

Ag/AgCl| internal filling solution|| membrane||test solution| SCE

The calibration curves were prepared by using Microsoft office Excel 2016.

2.3.3 Pharmaceutical Samples Preparation

Ten 500 mg pills of clarithromycin were completely ground up and precisely weighed. 5.8692 g was determined to be Ie. This powder weighed 0.0878 g. as the active weighed of single tablet was dissolved in 250 mL of acetonitrile and filtered. The resulted solution is left 1×10-3 M.

2.3.4 Selectivity Coefficient Calculation

a1,a2 are activities and z1, z2 are charge numbers for 1 ion, respectively, at a1 = a2.

The coefficients of selectivity were calculated using the fixed interference method (mixed method) (Shakir, 2016) (Abdulla et al., 2005) by using equation (1):

$K^{pot}_{1,2}=a_1/(a_2)^{z1/z2}$ (2)

3. RESULTS AND DISCUSSION

The following are the calibration curves for two CN electrodes (C1 and C2), the C1 sensor was found at the junction of the extrapolated segments of the calibration curve's two linear sections. The slope value of electrode C1 was attributed to the high mixing between PVC and TBP, which resulted from the plasticizer's compatibility with the electro-active substance in terms of both composition and structure. Figure. (2) below displays a typical plot of electrode calibration curves of TBP & ONPOE.

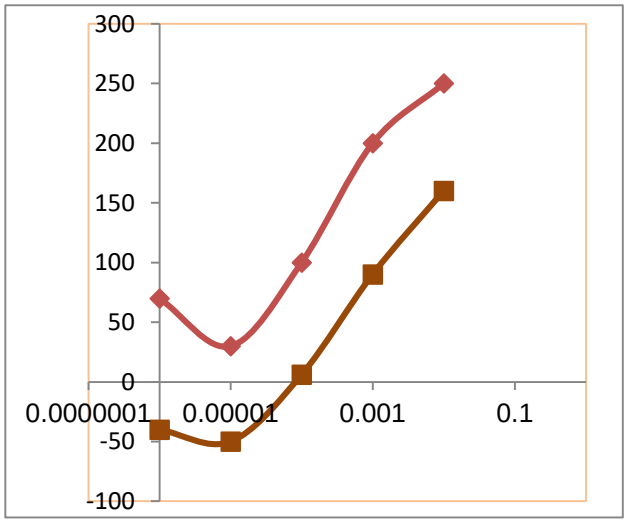

Figure 2: Selective electrodes CN Calibration curves with plasticizer TBP C1 (light red) ONPOE C2 (dark red)

The values of the slopes for the electrodes based on TBP and ONPOE were 55.699 and 53.895 mV/decade, respectively, and correlation coefficients were 0.9995, 0.9994. These electrodes have a linear range of 10^{-5}–0.01 and 7×10^{-5}–0.01M, with corresponding detection limits of 5×10-5M and 9×10-6M. Table (1) presents the outcomes together with other factors.

Table 1. C1 and C2 electrodes parameters

Electrode		**C1**	**C2**
Slope (mV/Decade)		**55.699**	**53.895**
Correlation coefficient(r)		**0.9995**	**0.9994**
Linear concentration range (M)		10^{-5}-10^{-2}	7×10^{-5}-10^{-2}
Detection limit (M)		9×10^{-6}	5×10^{-5}
Response time in sec.	1×10^{-2} M	23	20
	1×10^{-3} M	19	13
	1×10^{-4} M	13	8
Lifetime (day)		16	10

3.1 Effect of pH

The cell potential in CN solutions was measured at (0.01 and 0.001) M concentrations, where the pH varied from (0.5) to (11.0), the impact of pH was investigated. The right quantities of hydrochloric acid or sodium hydroxide solution were added to change the pH. Figure (3) displays the outcomes.

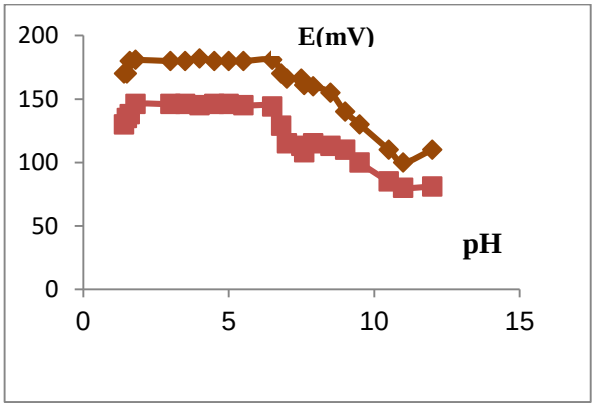

Figure 3. Effect of pH on C1 electrode at concentrations 0.01M (light red) 0.001 M. (dark red)

In very acidic environments or at pH values below 1.5, the electrode response has risen fairly erratically. This might be because the electrode begins to respond to ions and H+ activities. The electrode response starts to decline in an alkaline solution (pH over 7), which could be related to CN's diminishing solubility (Shakir, 2016) (Nassory et al., 2008) (Ismaeel & Al-Phalahy, 2020). Table (2) is a tabulation of the working pH.

Table 2. working pH Ranges, (CN) electrode C1.

C1 and range pH	
0.01 (M)	0.001 (M)
1.6-6.7	1.8-6.8

3.2 Interference studies

Equation (1) was used to examine the suggested membrane C1 electrode's selectivity toward clarithromycin in relation to interfering ions using a mixed solution approach.

Table 3. $K^{pot}_{A,B}$ Values - d FIM using electrode C1

	FIM	**method**
Interfering ions	a_a	$K^{pot}_{A,B}$
Mn^{+2}	4.9×10-5	2.241 ×10-4
Fe^{+3}	2.0×10-5	5.433×10-5
Cu^{+2}	3.9×10-5	1.678 ×10-4

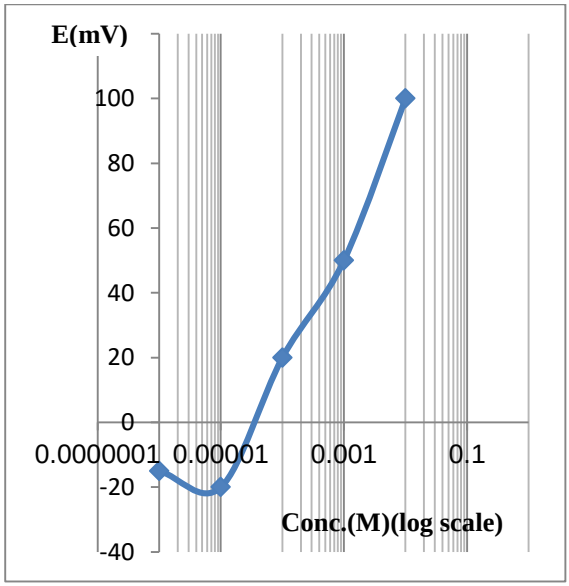

Figure 4. Clarithromycin selective electrode C1 Fe+3 interfering ion calibration curve for the fixed interfering technique

3.3 Sample Analysis

Clarithromycin was measured using potentiometric approaches, such as the standard addition method (SAM) and direct method, which both employed the equation:

$CS = 10\Delta E/S\ [1+ (VU / VS)] = CU - (VU/VS)$

If multiple standard additions (MSA) are calculated using the following equation, and CS, CU, VS and VU, stand for the volume as well as the concentration of the unknown in addition to the standard solution, respectively:

$VS \times CS / VU = CU$

where VS is the volume of standard solution, CS is the concentration of the unknown, and CU is the standard. The method was conducted as shown in Figure (5).

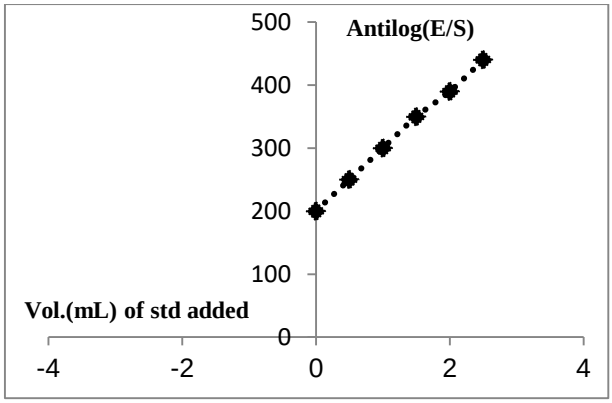

Figure 5. Clarithromycin selective electrode C1 Fe+3 interfering ion calibration curve for the fixed interfering technique

The concentration of clarithromycin may be examined and compared with the working range calibration curve of MSA by graphing antilog (E/S) with the volume of the five additions of standard clarithromycin. for titrating potentiometrically. Figure (6) displays a typical titration plot.

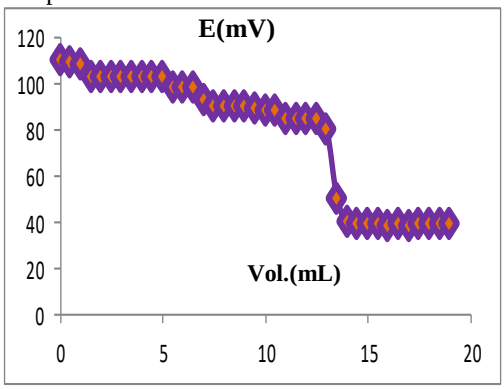

Figure 6. Titration curve of Electrode (a), a sample solution (15 mL) of clarithromycin (0.01 M) in a titrant solution containing 0.0 1M of TPB

Table 4 presents the results of the calculation of (RSD %), the relative standard deviation, (Er %) relative error, recovery (Re %), and for the titration technique.

Table 4. CN Analysis - titration method using ISE C1

Method	**Titration method****
Conc.(M)	1.000×10^{-3}
Found(M)	0.969×10^{-3}
RSD*%	0.700%
Re%	98.4%
Er%	-1.6%

For every approach, (Er %) the relative error, (RSD %) relative standard deviation, and (Re %) recovery were computed. Table (5) below displays the findings.

Table 5. CR Analysis by ISE (C1)

Parameter	**Direct method ***	**SAM***	**Multi SAM***	**Titration method*****
Conc.	1.000 × 10-3 (M)	1.000 × 10-3 (M)	1.000 ×10-3	1.000 ×1 0-3 (M)
Found	0.996 × 10-3 (M)	0.989 × 10-3 (M)	1.009 ×10-3	0.969×10^{-3} (M)
% RSD*	0.468%	0.414%	-------	0.700%
% Re	99.4%	99.2%	100.7%	98.4%
% Er	-0.6%	-0.8%	0.7%	-1.6%

RSD*% for n=5, t=2.7, RSD**% for n=3, t=4.3, RSD***% for n=2, t=12.7

In Table (6), the data acquired for pharmaceutical samples demonstrating the use of electrode C1 in the potentiometric assessment of clarithromycin in pharmaceutical industry.

Table 6. Analysis of CN in pharmaceutical sample

Parameter	**Direct method ***	**SAM***	**Multi SAM ***	**Titration method*****
Conc. (M)	1.000 × 10-3	1.000 × 10-3	1.000 ×10-3	1.000 × 10-3
Found * (M)	0.979 × 10-3	0.993 × 10-3	1.02 × 10-3	0.978 × 10-3
% RSD *	0.577%	0.511%	-------	0.688%
Re %	98.8%	98.9%	101.1 %	98.1%
Er %	-1.2%	-1.1%	1.1%	-1.9%

4. CONCLUSION

Two electrodes of clarithromycin were prepared using the ionic complex clarithromycin-bromophenol Blue in a polyvinyl chloride matrix to form the membrane using two plasticizers, tributyl phosphate (TBP) and orthonitrophenyl octyl ether (ONPOE). Clarithromycin electrodes [C1and C2] gave a slope of (55.699 and 53.895 mV/decade) and linear range of concentrations (10^{-5}-10^{-2} and 7×10^{-5}-10^{-2} m), respectively. (C1) the best electrode with TBP plasticizer presented a slope of 55.699 mV/decade, correlation coefficient 0.9995and limit of detection(9×10^{-6})M , at an age of 16 days. Electrode C1 showed high stability and thus, was important for clarithromycin determination in pharmaceutical samples. Interference measurements in the presence of some ions were calculated by relying on the method of mixed solution.

5. Acknowledgements

This research was self-funded.

6. Conflict of interest

The authors declare no conflict of interest in this reported work.

REFERENCES

Abdulla, N. I., Al-Haideri, A. M., Al-Joboury, M. I., & Nassory, N. S. (2005). Construction and characterization of indium liquid ion selective electrodes based on crown ethers in a PVC matrix membrane. *Turkish Journal of Chemistry*, *29*(6), 687–696.

Abrahem, S. A. (2022). Analysing aflatoxin production conditions in feed samples using a preparative thin layer chromatography (TLC) method. *Iraqi Journal of Science*, 9–20.

Abrahem, S. A., Ahmad, S. M., & Al-Phalahy, B. A. (2022). Novel potentiometric sensor for estimation of the moxifloxacin in the pharmaceutical samples, urine, and serum. *International Journal of Drug Delivery Technology*, *12*(4), 1663–1668.

Abrahem, S. A., Saad, A., & Ibrahim, S. A. (2020). Various analytical methods for the determination of clarithromycin: A review. *International Journal of Research in Engineering and Innovation*, *4*(1), 56–59.

Al-Baitai, A. Y., Abdalhadi, S. M., Ibrahim, S. A., Ali, A. A., & Alzamily, G. H. (2020). The effect of temperature and storage time on the concentration of vitamin D in human serum. *Systematic Reviews in Pharmacy*, *11*(4), 695–700.

Amini, H., & Ahmadiani, A. (2005). Sensitive determination of clarithromycin in human plasma by high-performance liquid chromatography with spectrophotometric detection. *Journal of Chromatography B*, *817*(2), 193–197.

British Pharmacopoeia. (2009). *Specific monographs* (Vol. 3, p. 8359). The Stationery Office on behalf of the Medicines and Healthcare Products Regulatory Agency.

British Pharmacopoeia. (2014). *Medicinal and pharmaceutical substances* (Vol. 1, No. 2, pp. 1406–1407). The Stationery Office on behalf of the Medicines and Healthcare Products Regulatory Agency.

Chandra, S., Sharma, K., & Kumar, A. (2013). Mg(II) selective PVC membrane electrode based on methyl phenyl semicarbazone as an ionophore. *Journal of Chemistry*, *2013*, Article 189464.

Craggs, A., Moody, G. J., & Thomas, J. D. R. (1974). PVC matrix membrane ion-selective electrodes: Construction and laboratory experiments. *Journal of Chemical Education*, *51*(8), 541.

Ismaeel, Y. Q., & Al-Phalahy, B. A. (2020). A new cyproheptadine PVC ion selective electrode and their applications in pharmaceutical preparations and human fluids. *Al-Nahrain Journal of Science*, *23*(2), 26–32.

Kanfer, I., Skinner, M. F., & Walker, R. B. (1998). Analysis of macrolide antibiotics. *Journal of Chromatography A*, *812*(1–2), 255–286.

Koryta, J. (1977). Theory and applications of ion-selective electrodes. Part 2. *Analytica Chimica Acta*, *91*(1), 1–85.

Langtry, H. D., & Brogden, R. N. (1997). Clarithromycin: A review of its efficacy in the treatment of respiratory tract infections in immunocompetent patients. *Drugs*, *53*, 973–1004.

Li, W., Jia, H., & Zhao, K. (2007). Determination of clarithromycin in rat plasma by HPLC–UV method with pre-column derivatization. *Talanta*, *71*(1), 385–390.

Nassory, N. S., Maki, S. A., & Al-Phalahy, B. A. (2008). Preparation and potentiometric study of promethazine hydrochloride selective electrodes and their use in determining some drugs. *Turkish Journal of Chemistry*, *32*(5), 539–548.

Shakir, I. M. (2016). A novel online coupling of ion selective electrode with the flow injection system for the determination of vitamin B1. *Baghdad Science Journal*, *13*(2), 458.

Umezawa, Y., Umezawa, K., & Sato, H. (1995). Selectivity coefficients for ion-selective electrodes: Recommended methods for reporting K_A,B^pot values (Technical report). *Pure and Applied Chemistry*, *67*(3), 507–518.

PURE SCIENCES
International Journal of Kerbala

Pure Sciences International Journal of Kerbala

Year: 2025 Volume : 2 Issue : 8 ISSN: 6188-2789 Print 3005 -2394 Online

2025,Volume 2 , Issue 8 , PSIJK (46-51)

Pure Sciences International Journal of Kerbala

Detection of TAFI 1040C>T rs1926447 Gene Polymorphism in Type 2 Diabetes Mellitus Iraqi Patients

Eatmad Abed Ali Alshawi [a*], Elham Abed Mahdi [b]

[a*] *Department of Medical Laboratory Technologies, Kufa Institute, Al-Furate Al-Awsat Technical University, Najaf, Iraq*
[b] *Department of Chemistry, Collage of Education for Girls, University of Kufa, Najaf, Iraq*

P A P E R I N F O

Received: 09.04.2025
Accepted: 23.06.2025
Published: 30.09.2025

Keywords:

Thrombin Activatable Fibrinolysis Inhibitor, Diabetes type 2, thrombosis, polymorphism

A B S T R A C T

In Diabetes mellitus is a group of metabolic diseases characterized by hyperglycemia resulting from defects in insulin secretion, insulin action, or both. The chronic hyperglycemia of diabetes is associated with long-term damage. Thrombin-Activatable Fibrinolysis Inhibitor(TAFI) is a protein that plays a major role in regulating the analysis of blood clots, It is involved in the fibrinolysis process. The study was designed to study the change concentration of TAFI, Insulin, HOMA-IR, and lipid profile in the T2DM patient in addition to studying the TAFI 1040C>T SNP (rs1926447) gene polymorphism with the development of T2DM complication. Genome study doing by restriction fragment length polymorphism PCR (RFLP-PCR). These parameters included the evaluated of glucose metabolic characteristics (FSG, insulin, HbA1C, HOMA-IR, lipid profile). The expected frequencies, calculated under the assumption of no association, were 47.61for CC, 60.03, CT, and 9.61for TT. TC genotype does not appear a statistically significant linkage to the rise risk of thrombosis, OR(3.272) is and CI (0.4173 to 1.4498), p-value <0.0002 was associated with an increased danger of the thrombosis to three times. frequency of C allele among cases is 43.5%, but it is 69% among controls. Frequency T allele was among cases is 56.5%, whereas it is 31% among controls. The findings of this investigation revealed that there was significant link between the TAFI 1040C>T polymorphism and T2DM complication in Iraqi patients. However, we recommend conducting the study in a larger sample and different sexes to confirm our findings.

DOI: 10.53851/psijk.v2.i8.46 -51

1. INTRODUCTION

Type 2 diabetes mellitus (T2DM) is a complex illness in which genetics and environmental factors both play important roles in disease etiology. Diabetes causes chronic hyperglycemia, which causes organ malfunction, mainly in the eyes, kidneys, nerves, heart, and blood vessels. T2DM is known by the failure of pancreas cell's to generate enough insulin hormone to preservation blood sugar levels under control (Hong et al., 2022). The reason causing T2DM includes a combination between a genetic predisposition and environmental factors systemic insulin resistance, (Javeed & Matveyenko, 2018).

T2DM patients suffer diabetic neuropathy after being diagnosed, but 25% of them will suffer it after obtaining the disease for at least 25 years (Al-Attaby & Al-Lami, 2019). Diabetes has a severe impact on the retina, causing diabetic retinopath DR, a degenerative condition that is the leading cause of blindness in diabetics.(Atwany et al., 2022). Diabetes problems primarily affect the coronary arteries, peripheral arteries ,macrovascular complications , and cerebrovasculature. Atherosclerotic causing plaque in the vasculature providing blood to the heart, brain, limbs, and other organs is related with early macrovascular disease. Late-stage macrovascular disease results in full occlusion of these arteries, rising risk of myocardial infarction(MI), stroke, claudication, and gangrene. Cardiovascular disease (CVD) is the leading cause of morbidity and death in diabetic people(Low Wang et al., 2016). Disorders fibrinolysis and Coagulation are well-known consequences of T2DM .In addition, they contribute to a rise in macrovascular consequences such myocardial infarction and ischemic stroke(Rattanawan et al., 2018). TAFI synthesized by the liver and megakaryocytes(MKs) as a propeptide. Besides, it is a zinc-dependent metallocarboxypeptidase, constraction of 423 a.a. when the 22 amino acid signal peptide is removed, the 56 kD a proenzyme containing 401 a.a is secreted into the blood stream(Totoki, 2020). TAFI construction from

*Corresponding Author Institutional Email:
eatmad.alshawi@atu.edu.iq (Eatmad Abed Ali Alshawi)

401 amino acids is divided into two chains. The first chain has 92 a.a. form the activation peptide, while another chain has 309 amino acids form the catalytic domain (Marx et al., 2008). The other known names: procarboxypeptidase R procarboxypeptidase U (CPU); procarboxypeptidase B (PCPB) and conceder carboxypeptidases are enzymes that hydrolyze C-terminal peptide bonds (Khamsehnejad et al., 2019) found in plasma and major role that controls fibrinolysis by decreising the quantity of fibrin accessible for fibrinolysis by tissue plasminogen activator (t-PA)(Mosnier et al., 2001). TAFI encoding by CPB2, The human (Carboxypeptidase B2 by the Human Genome Organization (HUGO), and is located on chromosome 13 (13q14.11. The gene spans 48 kb of genomic DNA, and has 11 exons and 10 introns(Bouma & Mosnier, 2003) . TAFI encoding by CPB2, The human (Carboxypeptidase B2 by the Human Genome Organization (HUGO), and is located on chromosome 13 (13q14.11. The gene spans 48 kb of genomic DNA, and has 11 exons and 10 introns (Rizzo, 2014), (Boffa et al., 1999). The polymorphisms of TAFI Ala147Thr or 505G/A (rs3742264), Thr325Ile or 1040C/T (rs1926447),+1542C/G (rs940) and +1583T/A (rs1087) have been reported to be associated with TAFI levels(Rattanawan et al., 2018). The higher levels of TAFI are associated with a high risk for arterial thrombosis and recurrent events in patients with an ischemic stroke.

2. MATERIALS AND METHODS

One hundred patient spacemen were taken from the Diabetes and Endocrinology Center at Sadr Medical City in Najaf, Iraq, following the acquisition of the required official approvals. Information. The individuals that took part in the study ranged in age from (35-55) , 48.3000±12.20242. Body mass index BMI (kg/m²) measurement by height, weight, 5 ml of divided into container. 2ml was placed in an EDTA tube and free zed to deep freeze at -20C for genotyping analysis while 3ml was placed in plane tube. Insulin concentration was calculated by "enzyme-linked immunosorbent assay" (ELSA) and then Insulin resistance was as calculated.

Genome Study We employed RELP to analyze DNA, which is a fundamental concept in the study that includes fragmenting of DNA samples using a especial restriction enzyme restriction, enzyme that detects and cut DNA at a specific short sequence. The lengths of these DNA fragments are subsequently separated using agarose gel electrophoresis(Promega). The number of cleavage sites present in the DNA sequence is represented by the number of bands seen on the gel. Program Information for TAFI 1040 C>T SNP condition initial denaturation 95 C°: 5 min 5 cycle, denaturation95 C°: 0.50 s, Annealing55 C0.50 s, and Extension72 C° go to 2 loop 35:1.0 min 3.5 cycle for 36X . Final Extension 72C°: 07.00 min 3.5 cycle. To perform the amplification reaction, 1 µl of extracted DNA was taken , 10 NEBUffer 5µl 1X, Restriction Enzyme(SPeI-HF) 1µl 10 units, and Nuclease- free Water 50µl. : Primers sequence of TAFI obtain from (ElDanasori et al., 2018).

2. 1. Statistically Study

Case-control study was applied. The statistical analysis in this study involved several methods and software. Continuous variables were expressed as mean ± standard deviation. The difference in means between patient (T2DM) and the healthy group was determined using the (Student's t-test with the SPSS v.26.0 software) and MedCalc software .The Hardy-Weinberg equation was used to mathematically measure the relationship between genotypes and allele frequency. The data were expressed in terms of odds ratio (OR), confidence interval (CI%), chi-square, and p-value.

3. RESULTS

Case control study was applied in this study that included 200 volunteers. (100 T2DM patients do not suffer from any complication and disease duration less than five years, with the age range 35-55 years, and 100 healthy subjects as a control group Table 1.

TABLE1. Phenotyping of T2DM patients and the control group

Parameter	T2DM Patients	Control	P-Value
NO. of F/M	100(58/ 42)	100(48/52)	------
Age/Y	48.030±10.479	35.500±9.853	0.000
Height (m^2)	1.7111±.270	1.6858±.098	0.342
Wight(Kg)	71.9300±10.995	76.2347±12.974	0.000
BMI Kg/ m^2	26.53705±3.152	26.7353 ± 3.547	0.000
SBP(mmHg)	132.80±18. 09	125.49±4.01	0.063
DBP(mmHg)	81.29 ±10.48	83.15±2.44	0.086
Onset diseases (Y)	2.9293±1.597	----------	----------

BMI, body mass index, SBP (systolic blood pressure), DBP (diastolic blood pressure), F (female), and M (male) are all significant at the 0.05 level when comparing the patient and control groups**..**

With a statistical significance of less than (P<0.001) for each age, weight, and BMI, respectively, Table 1 demonstrated statistically significant associations and is one of the indicators linked to the indications of type 2 diabetes, the worldwide rise in the incidence of obesity has coincided with a rise in the prevalence of type 2 diabetes. However there are no statistically differences (p>0.05) height, SBP and DBP (Alberti et al., 2004).

TABLE 2. Compare between T2DM patients and control group mean± SD

C>T 1040	Cases N=100	Controls N=100	OR	95%CI	P-value
CC	21	59	0.184	0.098 to 0.345	< 0.000
TT	34	21	1.938	1.027 to 3.6556	0.041
TC	45	20	3.272	1.745 to 6.137	0.0002
Allele Frequencies					
C	43.5%	69%	0.3459	0.2296 to 0.5211	< 0.0001
T	56.5%	31%			

FSG: fasting serum glucose, HOMO-IR: Homeostatic Model Assessment for Insulin Resistance, TG: Triglyceride, HDL:high-density lipoprotein, LDL: low-density lipoproteins, and vLDL: very low-density lipoprotein) The practical part of the present study involved estimating the necessary biochemical parameters, which may be demonstrated. These parameters included the evaluated of glucose metabolic characteristics (FSG, insulin, HbA1C, HOMA-IR, lipid profile. When comparing the T2DM patients to the healthy control groups, the study's most evident conclusion was the significant increase in HOMA-IR. Table 2 shows that cholesterol values in T2DM patients are higher than those of healthy control groups and this result corroborates with the previous studies(Silva et al., 2018). TG values of T2DM patients were higher than those of control groups with a statistically significant increase (213.53±22.49, 107.08±16.93) respectively. HDL-C values of diabetic T2DM patients are lower than those of control with a statistically significant increase (42.76 ± 9.11, 57.73±17.03)(Shahwan et al., 2019). The LDL-C values of T2DM patients are higher than those of control with a statistically significant increase (193.929±27.10, 87.052±25.00)(Mohd Yasir Khan, Sultan Alouffi, Mohd. Shahnawaz Khan, Fohad Mabood Husain, Firoz Akhter, 2020). VLDL-C values of T2DM patients are higher than those of control with a statistically significant increase(42.70±8.49, 29.60 ±7.27)(Krentz, 2003). The Present study reveals significant differences in the TAFI levels between groups.

3.1. Genotyping Study

Current fending showed the association between the TAFI 1040 C>T genetic variant and the risk of a specific condition (diabetes complication). TC genotype did not show a statistically significant association with the risk of thrombosis, as the (OR) 3.272 is and CI (0.4173 to 1.4498), p-value <0.0002 is associated with a statistically significant increased risk of the thrombosis to three times. The C allele frequency among cases is 43.5%, while 69% among controls. The T allele frequency among cases is 56.5%, while it is 31% among controls Table 3

TABLE 3. Distribution TAFI Gene 1040 C/T(rs1926447) Polymorphism Genotype in T2DM and Control Subject

Recessive Mode					
Genotype	Cases N=100	Control N=100	OR	95%CI	P-value
CC+CT	66	79	0.5160	0.2736 to 0.9734	0.041
TT	34	21			
Dominant Mode					
Genotype	Cases N=100	Control N=100	OR	95%CI	P-value
CC	21	59	0.1847	0.0989 to 0.345	<0.000
TT+CT	79	41			

According to Table 4's recessive mode analysis, people with the CC+CT genotype are less likely to get sick than those with the TT genotype. The OR for the recessive mode is 0.5160. The p-value associated with the odds ratio is 0.041, which is less than the conventional significance level of 0.05

TABLE 4: Apply HWE for Polymorphism TAFI Gene 1040 C/T(rs1926447)

Variables	T2DM Patients	Control	P-Value
FSG mg/dl	228.65 ± 35.92	94.2600 ±8.06491	0.000
Insulinμ	33.34±10.55	8.32±3.20	0.000
HbA1C%	8.452±1.2993	4.50±.5.73	0.000
HOMA-IR	18.19±6.49	1.94 ±0.82	0.000
Lipid profile			
Cholesterol mg/dl	264.10±28.33	171.05±17.62	0.000
TG mg/dl	213.53±22.49	107.08±16.93	0.000
HDL-C mg/dl	42.76 ± 9.11	57.73±17.03	0.000
LDL-C(mg/dl)	193.929±27.10	87.052±25.00	0.000
vLDL-C(mg/dl)	42.70±8.49	29.60±7.27	0.000
TAFI Pg/ml	396.95 ±163.02	286.65±87.83	0.011

Table 5 shows the actual and predicted genotype frequencies for a particular genetic variation. Twenty people have the TT genotype, twenty-one have the CT genotype, and fifty-nine have the CC genotype. The anticipated frequencies, calculated under the assumption of no association, were 47.61for CC, 60.03, CT, and 9.61for TT.

TABLE 5. Pearson correlation between TAFI Gene 1040 C/T(rs1926447) and another biochemical parameters

Variables	Groups			
	T2DM Patients		control	
	r	p	r	p
Insulin μU/ml	0.272**	0.006	0.051	0.617
FSG mg/dl	0.202*	0.044	0.084	0.407
HbA1c	0.805**	0.000	0.113	0.262
HOMA-IR	0.378**	0.000	0.182	0.070
Cholesterol mg/dl	0.695**	0.000	0.097	0.336
TG mg/dl	0.376**	0.000	0.024	0.812
HDL-c mg/dl	-0.657**	0.000	-0.055	0.588
LDL-c mg/dl	0.694**	0.000	0.136	0.179
vLDL-C mg/dl	0.376**	0.000	0.063	0.536

4. DISCUSSION

The practical part of the present study involved estimating the necessary biochemical parameters by which may be demonstrated the metabolic disorders. These parameters included the measurement of glucose metabolic characteristics (fasting blood glucose, fasting insulin, and Homeostatic Model Assessment for Insulin Resistance HAMA- IR) (Mansour et al., 2022). Furthermore, the study is highly statistically significant, which is consistent with earlier research that has found out that patients who were overweight and had higher BMI values had a higher chance of developing diabetes than participants who were healthy.(Anakök et al., 2022). Obesity is an indicator of body fat(Reis et al., 2009), which can be estimated by measuring body mass index (BMI) and waist circumference (WC) (Dhurandhar, 2022).

Insulin resistance levels were represented by the HOMA-IR. HOMA-IR values in the healthy and T2DM patients groups were mean± SD (1.94 ± 0.82), and (18.19±6.49) respectively. Result had shown Insulin levels in T2DM patients group were higher than those in control group and the difference was statically significant(p-value<0.05). Insulin is the primary regulator of glucose and lipid homeostasis; it increases the absorption of glucose into striated muscles and adipocytes and decreases blood glucose levels by blocking hepatic gluconeogenesis and glycogenolysis. Moreover, it stimulates the breakdown of circulating lipoproteins by inducing lipoprotein lipase activity in adipocytes, boosts triglyceride production in the liver and adipose tissues, and enhances glucose absorption into striated muscles and adipocytes. Circulating glucose levels remain elevated when adipose, muscle, and liver cells fail to respond appropriately to insulin, which destabilizes the feedback system. Table 2. demonstrated that T2DM patients' cholesterol levels are statistically significantly higher than those of healthy control groups, which is consistent with earlier research.(Tham et al., 2023). Cholesterol metabolism is altered in diabetic states. There are three causes of the rise in cholesterol in T2DM patients increased glycation of cholesterol-rich lipoproteins, an insulin-resistant state that is mainly present in overweight type 2 diabetic patients, and changes in insulin secretion which depends on the clinical T2DM(Khan et al., 2020).

The present study found triglyceride values of T2DM patients were higher than those of control groups with a statistically significant increase. This result agrees with the results obtained by several studies (213.53±22.49, 107.08±16.93) respectively. HDL-C values of diabetic T2DM patients are lower than those of control with a statistically significant increase(42.76±9.11,57.73±17.03)Table 3.3(Shahwan et al., 2019). The LDL-C values of T2DM patients are higher than those of control with a statistically significant increase (193.929±27.10, 87.052±25.00). Diabetes is associated with quantitative changes in the amount of circulating lipids notably an increase in triglycerides, elevated LDL and a reduction in HDL-C (Femlak et al., 2017). In our study TT was significant with T2DM patient 34% with TT whereas, 21% of control group have this polymorphism. There is ongoing research into the relationship between TAFI and maternal thrombophilia or hypo fibrinolytic gene variations, and new data indicates that thrombophilic circumstances may worsen the prothrombotic state in type 2 diabetes. These thrombophilic disorders may affect the fibrinolysis clot's function and lead to inadequate advancement of diabetic complications. Stronger evidence of a connection between plasma TAFI levels and cardiovascular disease(Tregouet et al., 2009). TAFI levels were discovered to be connected to an increased risk of ischemic stroke. Based on the information in Table4, it appears that the CT genotype is associated with an increased risk of developing the T2DM complication . In the context of the chi-square analysis and the observed genotype frequencies, the CT genotype is overrepresented among the cases compared to the expected frequencies. This suggests that individuals with the CT genotype might be at a higher risk of developing the thrombosis in future in patient with T2DM. Depended on Table 5, TAFI levels in plasma have been linked to an approximately fourfold increase in the incidence of acute coronary artery disease (CAD). Endothelial functional thromboresistance is lowered in diabetes patients. (Thomas & Iyngkaran, 2020). A prethrombotic condition is caused by increased intravascular thrombin production, decreased fibrinolytic capacity, and hyperactive platelets.

5. CONCLUSION

The current study showed a high and statistically significant correlation between diabetes TAFI, insulin, and HOMA-IR, while the study found a correlation between 1040 C/T (rs1926447) polymorphism and development risk T2DM complications in Iraqi patients. Based on this information, we recommend that a more comprehensive study of different ethnic groups to be conducted and that it has to be conducted with more numbers. Type 2 diabetes has a high linkage with thrombosis, along with the result of damage to cell endothelial and oxidative proteins, and it is associated with hypofibrinolysis via increased TAFI level, which increases with diabetes duration.

REFERENCES

Al-Attaby, A. K. T., & Al-Lami, M. Q. D. (2019). Effects of duration and complications of type 2 diabetes mellitus on diabetic related parameters, adipocytokines and calcium regulating hormones. *Iraqi Journal of Science*, *60*(11), 2353–2361. https://doi.org/10.24996/ijs.2019.60.11.5

Alberti, G., Zimmet, P., Shaw, J., Bloomgarden, Z., Kaufman, F., & Silink, M. (2004). Type 2 diabetes in the Young: The Evolving Epidemic. The International Diabetes Federation Consensus Workshop. *Diabetes Care*, *27*(7), 1798–1811. https://doi.org/10.2337/diacare.27.7.1798

Anakök, G. A., Awad, S. F., Çağlayan, Ç., Huangfu, P., Abu-Raddad, L. J., Unal, B., & Critchley, J. A. (2022). Impact of trends and gender disparity in obesity on future type 2 diabetes in Turkey: a mathematical modelling analysis. *BMJ Open*, *12*(5), e053541. https://doi.org/10.1136/bmjopen-2021-053541

Atwany, M. Z., Sahyoun, A. H., & Yaqub, M. (2022). Deep Learning Techniques for Diabetic Retinopathy Classification: A Survey. *IEEE Access*, *10*, 28642–28655. https://doi.org/10.1109/ACCESS.2022.3157632

Boffa, M. B., Reid, T. S., Joo, E., Nesheim, M. E., & Koschinsky, M. L. (1999). Characterization of the gene encoding human TAFI (thrombin-activable fibrinolysis inhibitor; plasma procarboxypeptidase B). *Biochemistry*, *38*(20), 6547–6558. https://doi.org/10.1021/bi990229v

Bouma, B. N., & Mosnier, L. O. (2003). Thrombin Activatable Fibrinolysis Inhibitor (TAFI) at the interface between coagulation and fibrinolysis. *Pathophysiology of Haemostasis and Thrombosis*, *33*(5–6), 375–381. https://doi.org/10.1159/000083832

Dhurandhar, N. V. (2022). What is obesity?: Obesity Musings. *International Journal of Obesity*, *46*(6), 1081–1082. https://doi.org/10.1038/s41366-022-01088-1

Durak, A., Olgar, Y., Degirmenci, S., Akkus, E., Tuncay, E., & Turan, B. (2018). A SGLT2 inhibitor dapagliflozin suppresses prolonged ventricular-repolarization through augmentation of mitochondrial function in insulin-resistant metabolic syndrome rats. *Cardiovascular Diabetology*, *17*(1), 1–17. https://doi.org/10.1186/s12933-018-0790-0

ElDanasori, N., Abulata, N., Shaheen, I. A., ElGendy, A. M., & El-Khayat, W. (2018). Thrombin-Activatable Fibrinolysis Inhibitor Gene Polymorphism (TAFI1040C/T) in Women With Recurrent Spontaneous Abortion. *Clinical and Applied Thrombosis/Hemostasis*, *24*(3), 532–535. https://doi.org/10.1177/1076029617695485

Femlak, M., Gluba-Brzózka, A., Ciałkowska-Rysz, A., & Rysz, J. (2017). The role and function of HDL in patients with diabetes mellitus and the related cardiovascular risk. *Lipids in Health and Disease*, *16*(1), 1–9. https://doi.org/10.1186/s12944-017-0594-3

Galicia-Garcia, U., Benito-Vicente, A., Jebari, S., Larrea-Sebal, A., Siddiqi, H., Uribe, K. B., Ostolaza, H., & Martín, C. (2020). Pathophysiology of type 2 diabetes mellitus. *International Journal of Molecular Sciences*, *21*(17), 1–34. https://doi.org/10.3390/ijms21176275

Hong, H. J., Joung, K. H., Kim, Y. K., Choi, M. J., Kang, S. G., Kim, J. T., Kang, Y. E., Chang, J. Y., Moon, J. H., Jun, S., Ro, H., Lee, Y., Kim, H., & Park, J. (2022). *Mitoribosome insuf fi ciency in β cells is associated with type 2 diabetes-like islet failure*. *March*. https://doi.org/10.1038/s12276-022-00797-x

Javeed, N., & Matveyenko, A. V. (2018). Circadian etiology of type 2 diabetes mellitus. *Physiology*, *33*(2), 138–150. https://doi.org/10.1152/physiol.00003.2018

Khamsehnejad, M. I., Djadid, N. D., & Raz, A. (2019). Identification, Molecular Characterization, and in Silico Structural Analysis of Carboxypeptidase B2 of Anopheles stephensi. *Journal of Medical Entomology*, *56*(1), 72–85. https://doi.org/10.1093/jme/tjy127

Khan, M. Y., Alouffi, S., Khan, M. S., Husain, F. M., Akhter, F., & Ahmad, S. (2020). The neoepitopes on methylglyoxal (MG) glycated LDL create autoimmune response; autoimmunity detection in T2DM patients with varying disease duration. *Cellular Immunology*, *351*(August 2019). https://doi.org/10.1016/j.cellimm.2020.104062

Krentz, A. J. (2003). Lipoprotein abnormalities and their consequences for patients with type 2 diabetes. *Diabetes, Obesity and Metabolism*, *5*(SUPPL. 1), s19–s27. https://doi.org/10.1046/j.1462-8902.2003.0310.x

Krishnaveni, M., Gowri, R. S., Sharmila, R., Krishnavani, J., & Haritha, P. (2022). *Systematic Review On Type-2 Diabetes Mellitus And Its Prevalence In India*. *13*(10), 5753–5758. https://doi.org/10.47750/pnr.2022.13.S10.707

Low Wang, C. C., Hess, C. N., Hiatt, W. R., & Goldfine, A. B. (2016). Clinical update: Cardiovascular disease in diabetes mellitus. *Circulation*, *133*(24), 2459–2502. https://doi.org/10.1161/CIRCULATIONAHA.116.022194

Mansour, A. A., Rahmah, A., & Khudhair, M. (2022).

Management of Type 2 Diabetes With Insulin Glargine-100 in Iraq in a Real-Life Observation. *Cureus*, *14*(11). https://doi.org/10.7759/cureus.31164

Marx, P. F., Brondijk, T. H. C., Plug, T., Romijn, R. A., Hemrika, W., Meijers, J. C. M., & Huizinga, E. G. (2008). Crystal structures of TAFI elucidate the inactivation mechanism of activated TAFI: A novel mechanism for enzyme autoregulation. *Blood*, *112*(7), 2803–2809. https://doi.org/10.1182/blood-2008-03-146001

Mohd Yasir Khan, Sultan Alouffi, Mohd. Shahnawaz Khan, Fohad Mabood Husain, Firoz Akhter, S. A. (2020). The neoepitopes on methylglyoxal (MG) glycated LDL create autoimmune re- sponse; Autoimmunity detection in T2DM patients with varying disease dura- tion. *Cellular Immunology*, 1–39. https://doi.org/https://doi.org/10.1016/j.cellimm.2020.104062

Mosnier, L. O., Lisman, T., Van Den Berg, H. M., Nieuwenhuis, H. K., Meijers, J. C. M., & Bouma, B. N. (2001). The defective down regulation of fibrinolysis in haemophilia A can be restored by increasing the TAFI plasma concentration. *Thrombosis and Haemostasis*, *86*(4), 1035–1039. https://doi.org/10.1055/s-0037-1616530

Rattanawan, C., Komanasin, N., Settasatian, N., Settasatian, C., Kukongviriyapan, U., Intharapetch, P., & Senthong, V. (2018). Association of TAFI gene polymorphisms with severity of coronary stenosis in stable coronary artery disease. *Thrombosis Research*, *171*, 171–176. https://doi.org/10.1016/j.thromres.2018.10.001

Reis, J. P., MacEra, C. A., Araneta, M. R., Lindsay, S. P., Marshall, S. J., & Wingard, D. L. (2009). Comparison of overall obesity and body fat distribution in predicting risk of mortality. *Obesity*, *17*(6), 1232–1239. https://doi.org/10.1038/oby.2008.664

Rizzo, C. M. (2014). *Scholarship at UWindsor Model Systems to Explore CPB2 Pre-mRNA Splicing*.

Shahwan, M. J., Jairoun, A. A., Farajallah, A., & Shanabli, S. (2019). Prevalence of dyslipidemia and factors affecting lipid profile in patients with type 2 diabetes. *Diabetes and Metabolic Syndrome: Clinical Research and Reviews*, *13*(4), 2387–2392. https://doi.org/10.1016/j.dsx.2019.06.009

Sharma, A., Weber, D., Raupbach, J., Dakal, T. C., Fließbach, K., Ramirez, A., Grune, T., & Wüllner, U. (2020). Advanced glycation end products and protein carbonyl levels in plasma reveal sex-specific differences in Parkinson's and Alzheimer's disease. *Redox Biology*, *34*, 101546. https://doi.org/10.1016/j.redox.2020.101546

Silva, F. M., Giatti, L., De Figueiredo, R. C., Molina, M. D. C. B., De Oliveira Cardoso, L., Duncan, B. B., & Barreto, S. M. (2018). Consumption of ultra-processed food and obesity: Cross sectional results from the Brazilian Longitudinal Study of Adult Health (ELSA-Brasil) cohort (2008-2010). *Public Health Nutrition*, *21*(12), 2271–2279. https://doi.org/10.1017/S1368980018000861

Tham, K. W., Abdul Ghani, R., Cua, S. C., Deerochanawong, C., Fojas, M., Hocking, S., Lee, J., Nam, T. Q., Pathan, F., Saboo, B., Soegondo, S., Somasundaram, N., Yong, A. M. L., Ashkenas, J., Webster, N., & Oldfield, B. (2023). Obesity in South and Southeast Asia—A new consensus on care and management. *Obesity Reviews*, *24*(2). https://doi.org/10.1111/obr.13520

Thomas, M. C., & Iyngkaran, P. (2020). Forensic interrogation of diabetic endothelitis in cardiovascular diseases and clinical translation in heart failure. *World Journal of Cardiology*, *12*(8), 409–418. https://doi.org/10.4330/wjc.v12.i8.409

Totoki, T. (2020). *Circulating Activated TAFI is a Prognostic Indicator in Septic DIC*. 1–11.

Tregouet, D. A., Schnabel, R., Alessi, M. C., Godefroy, T., Declerck, P. J., Nicaud, V., Munzel, T., Bickel, C., Rupprecht, H. J., Lubos, E., Zeller, T., Juhan-Vague, I., Blankenberg, S., Tiret, L., & Morange, P. E. (2009). Activated thrombin activatable fibrinolysis inhibitor levels are associated with the risk of cardiovascular death in patients with coronary artery disease: The Athero Gene study. *Journal of Thrombosis and Haemostasis*, *7*(1), 49–57. https://doi.org/10.1111/j.1538-7836.2008.03221.x

Vetrano, E., Rinaldi, L., Mormone, A., Giorgione, C., Galiero, R., Nevola, R., Marfella, R., Sasso, F. C., & Caturano, A. (2023). *and Non-viral Hepatocarcinoma : Pathophysiological Mechanisms and New Therapeutic Strategies*.

Yang, X., Hu, R., Wang, Z., Hou, Y., & Song, G. (2023). Associations Between Serum Folate Level and HOMA-IR in Chinese Patients with Type 2 Diabetes Mellitus. In *Diabetes, Metabolic Syndrome and Obesity: Vol. Volume 16* (pp. 1481–1491). https://doi.org/10.2147/dmso.s409291

PURE SCIENCES
International Journal of Kerbala

Pure Sciences International Journal of Kerbala

Year: 2025 Volume : 2 Issue : 8 ISSN: 6188-2789 Print 3005 -2394 Online

2025,Volume 2 , Issue 8 , PSIJK (52-56)

Pure Sciences International Journal of Kerbala

C-Reactive Protein and Uric Acid as Prognostic Biomarkers in Chronic Renal Failure: A Hemodialysis-Based Study from Kerbala, Iraq

Nada Habeeb Obaid [a] , Rehab Jasim Mohammed [a], Maha Jassim Manshad [a *] ,Bassma Maytham Oleiw [a]

[a] *Department of Chemistry ,College of Education for Pure Sciences, University of Kerbala, Iraq*

P A P E R I N F O

Received: 26.10.2025
Accepted: 07.12.2025
Published: 31.12.2025

Keywords:
dialysis, C-reactive protein (CRP), Enduring kidney impairment, Uric acid urea, creatinine, End-Stage Renal Failure (ESRF).

A b s t r a c t

Background: Chronic kidney disease (CKD) is an important health problem especially in low resource settings with limited access to sophisticated diagnostic facilities. Biochemical and inflammatory parameters, such as creatinine, urea, uric acid, and CRP, might serve as available alternatives for monitoring of the disease.

Methods: A case–control study was carried out at Al-Sadr Medical City, Kerbala, Iraq, comprising 39 hemodialysis patients and 30 gender- and age-matched healthy controls with chronic renal failure. Serum creatinine, urea, uric acid and CRP levels were determined by standard biochemical methods. The CO25 threshold was determined with receiver-operator curves (ROC) analysis, using SPSS software (version 26) and determining the sensitivity and specificity as well as area under the curve (AUC)

Results: The hemodialysis patients had a significantly higher mean level of creatinine (3.04 ± 1.60 mg.dL-1), urea (178.7 ± 96.0 mg.dL-1), uric acid (8.28 ± 3.39 mg.dL-1), and CRP (20.34 ± 2.17 mg.L-1) than the controls ($p < 0.001$). There was a strong positive correlation between CRP and uric acid ($r = 0.542$, $p = 0.002$) and between CRP and urea ($r = 0.54$, $p = 0.003$), while urea correlated with BMI and age ($p \leq 0.005$). ROC analysis showed a very good diagnostic accuracy (AUC/0.97–1.00) for all biomarkers, of which CRP and uric acid were essentially informative predictors.

Conclusion: The results emphasize the interplay between inflammatory and metabolic biomarkers in CKD. High CRP and uric acid not only reflect renal function, but also independently predict cardiovascular outcomes. The integration of these low-cost biomarkers in routine care of dialysis patients may aid in stratifying risk among Iraqi patients. These associations need to be verified by larger, prospective studies.

DOI: 10.53851/psijk.v2.i8.52-56

1. INTRODUCTION

About 10–13% of the world population is affected by functional incapacitation of the kidney (chronic kidney disease CKD), representing a major public health problem, since it diminishes quality of life and causes premature death (KDIGO, 2024). The economic burden is also substantial with the management of CKD and its complications representing large financial costs for health systems globally. Despite obvious reductions in CVD mortality among the general population, CVD

*Corresponding Author Institutional Email:
maha.j@uokerbala.edu.iq Maha Jassim Manshad

continues to account for the greatest proportion of mortality among CKD patients who exhibit a myriad of risk factors such as secondary hyperparathyroidism, increased oxidative stress, heightened sympathetic activity, and endothelial dysfunction manifested by deranged nitric oxide bioavailability and increased endothelin production (Ravarotto et al., 2022)(Wong, 2022).

Pathogenesis-wise, CKD is characterized by a chronic inflammatory condition. The liver is a key organ in the acute phase response, synthesizing proteins such as fibrinogen and C-reactive protein (CRP), and also downregulating transferrin and albumin (Jeena et al., 2022). CRP, as well as other cytokines including IL-6 and TNF-α at higher levels, is not only a marker for systemic inflammation but also an active mediator in endothelial injury and progression of atherosclerosis (Mohallem & Aryal, 2020).In particular, CRP has been identified as a powerful predictor of all-cause and cardiovascular mortality in patients on maintenance hemodialysis (Iseki et al., 1999)(Yeo et al., 2010).However, recent evidence demonstrates that CRP is part of novel inflammatory indices such as the CRP/albumin ratio and CALLY index, both of which are strong predictors of outcome in dialysis patients (Clinical Kidney Journal, 2025).

Besides inflammatory markers, metabolic biomarkers with a strong relation to renal function and cardiovascular risk are crucial. For example, hyperuricemia has been increasingly implicated as a factor contributing to oxidative stress, systemic inflammation, and vascular dysfunction. Nevertheless, the most recent publication of KDIGO 2024 guidelines does not support routine urate-lowering therapy for asymptomatic hyperuricemia in CKD because evidence from randomized trials is unconvincing (KDIGO, 2024).However, high SUA levels have been associated with faster progression of CKD and higher cardiovascular morbidity (Mufti et al., 2022).

Despite these findings, research gaps remain. Most of the studies that have derived the relationships of CRP, UA, and other related biomarkers in CKD have been in Western or Asian subjects, but little information is available on patients in the Middle East, and in particular in Iraq. This is crucial because of the increasing burden of ESRD and the lack of complete dialysis registries in the area (International Society of Nephrology, 2023). Accordingly, this study was carried out to assess the serum levels of CRP, uric acid, urea, and creatinine among patients with chronic renal failure on dialysis in Kerbala, Iraq, and their relation to demographic and clinical characteristics. By addressing the local gap of knowledge, this study aims to contribute to clinical practice and support the risk identification and management of CKD for Iraqi patients.

2. MATERIALS AND METHODS

This case–control study was conducted at Al-Sadr Medical City, Kerbala, Iraq, between April 2022 and January 2023, and included 39 patients with chronic renal failure (CRF) undergoing regular hemodialysis and 30 age- and sex-matched healthy controls. Clinical data (age, sex, body mass index, and blood pressure) were recorded, and venous blood samples were collected prior to dialysis in patients and after overnight fasting in controls. Biochemical analyses included serum creatinine, blood urea nitrogen, uric acid, and C-reactive protein (CRP); CRP was quantified by turbidimetric immunoassay, while other markers were measured using a Siemens Dimension RXL autoanalyzer with appropriate quality control. Statistical analysis was performed using SPSS v26, with data expressed as mean ± standard deviation. Group comparisons were conducted using independent t-tests (or Mann–Whitney U for non-normal data), correlations assessed by Spearman's test, and diagnostic performance evaluated by receiver operating characteristic (ROC) curves; $p \leq 0.05$ was considered statistically significant.

3 .RESULTS

Clinical and biochemical characteristics

Table 1 is a comparison of demographic and biochemical markers between CRF group and healthy control group. There were no statistically significant differences in the mean age of the groups and the BMI. Serum creatinine, urea, uric acid, and CRP were significantly higher in the CRF group than controls ($p < 0.001$). Systolic blood pressure and diastolic blood pressure were also significantly higher in the patient group.

Correlation analysis

Spearman's test revealed in Table 2:

CRP was directly related to serum uric acid ($r = 0.542$, $p = 0.002$), serum urea ($r = 0.54$, $p = 0.003$) and BMI ($r = 0.34$, $p = 0.004$)

Urea showed significant positive correlation with BMI ($r = 0.501$, $p = 0.005$), uric acid ($r = 0.443$, $p = 0.014$) and age ($r = 0.501$, $p = 0.005$)

Non-significant negative associations were also observed between the serum creatinine and urea ($r = -0.045$: $p = 0.814$) and serum uric acid and age ($r = -0.006$: $p = 0.974$).

ROC analysis demonstrated high diagnostic potential of the studied biomarkers in differentiating CRF patients from controls:

CRP: AUC = 1.00 (100% sensitivity, 100% specificity).

Uric acid: AUC = 0.97 (sensitivity = 100%, specificity = 100%).

Urea: AUC = 1.00 (sensitivity = 97%, specificity = 98%).

Creatinine: AUC = 1.00 (sensitivity = 100%, specificity = 100%).

differences in age and BMI were observed between the two groups. The present data highlight the importance of biochemical and inflammatory markers in reflecting both renal dysfunction and systemic inflammation. In particular, the levels of CRP were much higher, confirming the concept of CKD as a condition of chronic low-grade inflammation, associated with endothelial dysfunction, accelerated atherosclerosis, and enhanced cardiovascular risk (Ravarotto et al., 2022), (Clinical Kidney Journal, 2025) . Given that the value of CRP is associated with uric acid and urea, this also correlates with previous findings suggesting a synergistic role of inflammatory activity and metabolic disorders in the pathogenesis of CKD. High CRP has repeatedly been shown to be a powerful risk factor for cardiovascular morbidity and mortality in hemodialysis patients (Iseki et al., 1999), (Yeo et al., 2010), and its predictive performance was recently demonstrated to be particularly meaningful in combination with other components such as the CRP/albumin ratio and the CALLY index, significantly improving risk assessment in dialysis populations (Clinical Kidney Journal, 2025). We also found that hyperuricemia was associated with levels of CRP and urea in our patients. This is consistent with new data indicating that uric acid is not merely an indicator of impaired renal clearance but also induces oxidative and inflammatory pathways, leading to enhanced renal and vascular damage (Jeena et al., 2022), (Mufti et al., 2022). While the KDIGO 2024 guidelines do not recommend long-term urate-lowering therapy (ULT) for asymptomatic hyperuricemia because of inconclusive trial results, elevated SUA remains of clinical importance as a predictor of CKD progression and cardiovascular risk (KDIGO, 2024).Additionally, the significantly increased levels of serum creatinine and urea observed in the dialysis group versus controls serve as an additional confirmation of their usefulness as classical indicators of reduced glomerular filtration. BMI and increasing age were also significantly associated with urea (although not correlated with other clinical measurements), suggesting that metabolic stress and demographic factors influence the magnitude of biochemical disturbances in CKD. These findings are consistent with previous reports showing that raised urea and creatinine are associated with hypertension and increased cardiovascular morbidity (Piccoli et al., 2023), (Rong et al., 2022) Collectively, our results underscore the relationship between inflammation, metabolic disturbances, and renal damage in CRF patients. High CRP and uric acid levels seem to be particularly informative markers in that they not only mirror renal dysfunction but also carry prognostic value in terms of cardiovascular outcomes. These findings emphasize the possibility of including easily identifiable, inexpensive biomarkers in daily dialysis practice in Iraq, where facilities for advanced diagnostic tools are limited. Larger-scale and prospective studies are needed to confirm these findings and to evaluate the predictive role of inflammatory indices on regional levels.

4.CONCLUSION

The present study showed high significant levels of creatinine, urea, uric acid and CRP in patients who had CRF under dialysis when compared to the normal controls. These markers validated the concurrent renal dysfunction and systemic inflammation in patients with CKD. CRP was the most crucial marker, indicative of ongoing inflammation and endothelial damage and predicting cardiovascular events. High uric acid was not only a signal of reduced clearance, but also a driving force for oxidative stress and vascular damage. Significant associations of CRP, uric acid and urea highlight their combined action in the etiology of renal insufficiency. Creatinine and urea also endorsed their classical status of markers of impaired filtration. Urea relationships with BMI and age suggested metabolic and demographic influences. Collectively, these data highlight the importance of low-cost, readily available biomarkers for predicting disease severity. Such predictors are of special interest for developing health care system countries like Iraq. These findings should be confirmed and the predictive value of composite inflammatory indices on CKD outcomes should be investigated in larger prospective trials.

5. ACKNOWLEDGMENTS

We express our sincere appreciation to the team at Al-Sadr Teaching Hospital and its dialysis unit for their dedicated service.

TABLE 1. Clinical and biochemical characteristics of study participants (mean ± SD).

Parameters	Cr. Group	Control Group	P. Value
	Mean ±SD	Mean ±SD	
Age(years) 0.215	47.09±18.75	43.28±14.30	0.215
BMI	26.77±5.10	23.08±4.00	0.24
S. creatinine	3.04±1.60	0.90±0.22	<0.001*
S. urea	178.7± 96.00	22.90 ± 4.24	<0.001*
S. Uric acid	8.28 ± 3.39	4.81 ± 0.84	<0.001*
CRP	20.340± 2.17	0.25± 0.21	<0.001*
BP systolic	140.77±26.84	128.60±16.94	0.001*
BP diastolic	90.83±22.49	81.02±10.50	0.001*

TABLE 2. Spearman correlation coefficients among biochemical markers and clinical parameters in CRF patients.

Parameters		Urea	Uric Acid	Creatinine	CRP
urea	r-Correlation			-.045	-.138
	P-value			.814	.468
Uric acid	r- Correlation	.443*			.542
	P-value	.014			.003
creatinine	r- Correlation	-.045			
	P-value	.814			
CRP	r- Correlation	-.138	.542		
	P-value	.468	.002		
Age	r- Correlation	.501**	-.006		
	P-value	.005	.974		
BMI	r- Correlation	0.58			0.34
	P-value	0.002			0.004*

TABLE 3 : ROC curve analysis for biochemical markers.

Variable	Sensitivity	Specify
CRP	1	1
Urea	0.97	0.98
Uric acid	1	1
Creatinine	1	1

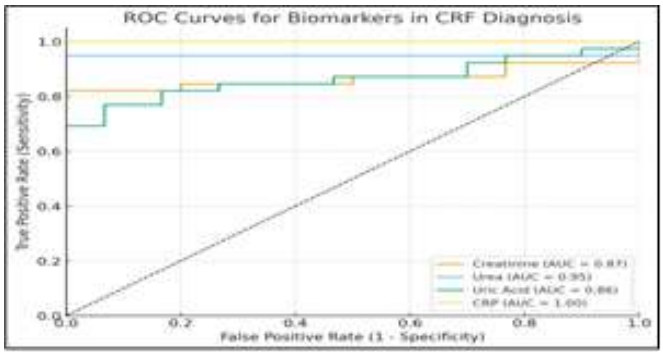

Figure 1. ROC Curves for Biomarkers in CRF Diagnosis

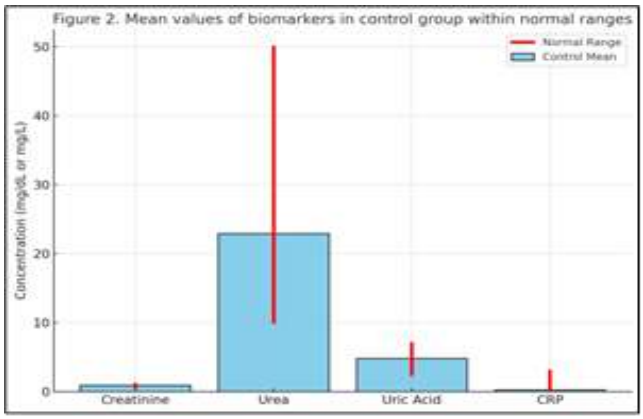

Figure 2. The mean values of creatinine, urea, uric acid, and CRP for the entire control group are within the normal range

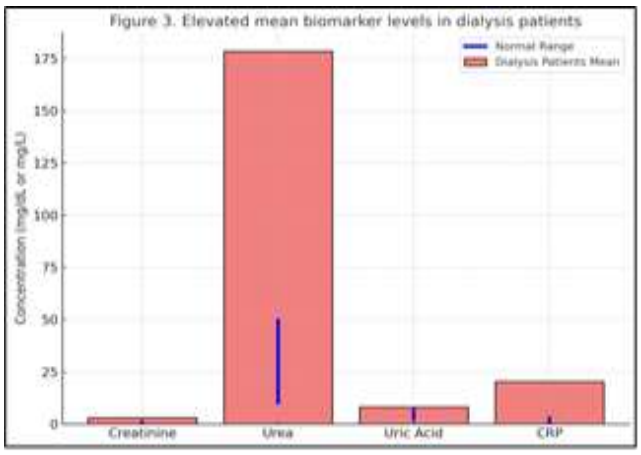

Figure 3. People who are receiving dialysis tend to have higher average levels of creatinine, urea, uric acid, and CRP

REFERENCES

Clinical Kidney Journal. (2025). Inflammation and novel prognostic indices in dialysis patients: Emerging perspectives. *Clinical Kidney Journal*, *18*(1), 1–10. https://doi.org/10.1093/ckj/sfae001

International Society of Nephrology. (2023). *Global kidney health atlas: Middle East and Africa regional report 2023*. ISN. https://www.theisn.org/global-atlas

Iseki, K., Tozawa, M., Yoshi, S., & Fukiyama, K. (1999). Serum C-reactive protein (CRP) and risk of death in chronic dialysis patients. *Nephrology Dialysis Transplantation*, *14*(8), 1956–1960. https://doi.org/10.1093/ndt/14.8.1956

Jeena, J., Manhas, S., Prasad, R., Prasad, S., & Gupta, R. (2022). Direct relationship between uric acid and C-reactive protein and its implication in the chronic kidney disease. *Indian Journal of Clinical Biochemistry*, *37*(3), 365–369. https://doi.org/10.1007/s12291-021-01026-y

KDIGO. (2024). *KDIGO 2024 clinical practice guideline for the evaluation and management of chronic kidney disease*. Kidney Disease: Improving Global Outcomes. https://kdigo.org/guidelines/ckd-2024

Mohallem, R., & Aryal, U. K. (2020). Regulators of TNFα mediated insulin resistance elucidated by quantitative proteomics. *Scientific Reports*, *10*(1), 20878. https://doi.org/10.1038/s41598-020-77597-3

Mufti, N. U. D., Khan, R. M., Haseeb, A., Sardar, W., Hanan, S., & Khan, S. A. (2022). Hyperuricemia in patients with chronic renal failure: A single-center study, Pakistan. *Pakistan Journal of Medical & Health Sciences*, *16*(5), 634.

Piccoli, G. B., Chatrenet, A., Cataldo, M., Torreggiani, M., Attini, R., Masturzo, B., … Moroni, G. (2023). Adding creatinine to routine pregnancy tests: A decision tree for calculating the cost of identifying patients with CKD in pregnancy. *Nephrology Dialysis Transplantation, 38*(1), 148–157. https://doi.org/10.1093/ndt/gfac268

Ravarotto, V., Bertoldi, G., Stefanelli, L. F., Nalesso, F., & Calò, L. A. (2022). Pathomechanism of oxidative stress in cardiovascular-renal remodeling and therapeutic strategies. *Kidney Research and Clinical Practice, 41*(5), 533–547. https://doi.org/10.23876/j.krcp.21.272

Rong, R., Wen, Q., Wang, Y., Zhou, Q., Qiu, Y., Lu, M., & Yu, X. (2022). Prognostic significance of hypertension at the onset of lupus nephritis in Chinese patients: Prevalence and clinical outcomes. *Journal of Human Hypertension, 36*(2), 153–162. https://doi.org/10.1038/s41371-021-00630-2

Wong, S. K. (2022). A review of current evidence on the relationship between phosphate metabolism and metabolic syndrome. *Nutrients, 14*(21), 4525. https://doi.org/10.3390/nu14214525

Yeo, E. S., Hwang, J. Y., Park, J. E., Choi, Y. J., Huh, K. B., & Kim, W. Y. (2010). Tumor necrosis factor (TNF-α) and C-reactive protein (CRP) are positively associated with the risk of chronic kidney disease in patients with type 2 diabetes. *Yonsei Medical Journal, 51*(4), 519–525. https://doi.org/10.3349/ymj.2010.51.4.519

PURE SCIENCES
International Journal of Kerbala

Pure Sciences International Journal of Kerbala

Year: 2025 Volume : 2 Issue : 8 ISSN: 6188-2789 Print 3005 -2394 Online

2025,Volume 2 , Issue 8 , PSIJK (57-63)

Pure Sciences International Journal of Kerbala

Estimation Local Fractional L_p Normed Spaces for $1 \leq p < \infty$

Nadiha Abed Habeeb [a*]

[a] *College of Engineering, University of Kerbala. Iraq*
[a] *College of Education, Al-Zahraa University for Women, Iraq*

P A P E R I N F O

Received: 01.10.2025
Accepted: 20.11.2025
Published: 31.12.2025

Keywords:

fractional integral, $L_p$space, Hadamard inequal

A B S T R A C T

This paper introduces an improvement and generalization of Hadamard inequality by using the spaces of local fractional L_p-normed spaces for $1 \leq p < \infty$, after Jacques Hadamard has presented his inequality in 1893 about bound on the determination of matrices by using the length of its column vectors. In addition, it is sometimes called Hemit Hadamard inequality with its convex function .The inequality that had been generalized to higher dimensions of function is bounded and convex domain in Euclidean space of n dimension .

DOI: 10.53851/psijk.v2i8.57 -63

1.Introduction

Hadmard introduced the first type of Hermite-Hadmard inequality (Hadmard,j,1893)

$$\varphi\left(\frac{\vartheta+\omega}{2}\right) \leq \frac{1}{\omega-\vartheta}\int_{\vartheta}^{\omega}\varphi(x)dx \leq \frac{\varphi(\vartheta)+\varphi(\omega)}{2} \qquad (1)$$

Bullen presented a generalization of Hermite-Hadmard estimate and proved (Bullen ,P,S,1978)

$$\frac{1}{\omega-\vartheta}\int_{\vartheta}^{\omega}\varphi(x)dx \leq \frac{1}{2}\left[\varphi\left(\frac{\vartheta+\omega}{2}\right)+\frac{\varphi(\vartheta)+\varphi(\omega)}{2}\right] \qquad (2)$$

you can look at a general survey for Bullen inequality in (Bullen ,P,S,1978)

, see also(Mitrinovic ,D.S.Pecaric ,J and Pecaric ,Jand Fink ,A.M.2013) and (Dragomir,S.S and Agarwal,R.P,1998).

As a refinement of (1), is the following result from (El Farissi, A,2010)

Theorem : Adopted $\varphi: I \to R$ is a curved role I. At that point for all $\lambda\epsilon[0,1]$,we will have

*Corresponding Author Institutional Email: nadiah.a@uokerbala.edu.iq (Nadiha Abed Habeeb)

$$\varphi\left(\frac{\vartheta+\omega}{2}\right) \leq I(\lambda)$$

$$\leq \frac{1}{\omega-\vartheta}\int_{\vartheta}^{\omega}\varphi(x)dx$$

$$\leq L(\lambda)\frac{\varphi(\vartheta)+\varphi(\omega)}{2}$$

Where

$$I(\lambda) = \lambda\varphi\left(\tfrac{\lambda\omega+(1-\lambda)\vartheta}{2}\right) + (1-$$

$\Lambda)\varphi\left(\tfrac{(1+\lambda)\omega+(1-\lambda)\vartheta}{2}\right)$.

And

L(Λ)=1/2(φ(Λω+(1-Λ)ϑ)+Λφ(ϑ)+(1-Λ)φ(ω))

To read more about the inequalities mentioned above, we can read the references [Mitrinovic ,D.S.Pecaric ,J and Pecaric ,Jand Fink ,A.M.2013), (El Farissi, A,2010)

, (Meftah,B & Boukerrioua Khaled 2017),(Meftah,B, M. Merad & A. Souahi 2019), (Eman ,S ,1999)]

This paper introduces an improvement and generalization of Hermite- Hadamard version inequalities and applications on the local fractional L_p normed spaces for $1 \leq p < \infty$.

Firstly let us recall and offer some definitions and notations, which are required in this study.

The function $\varphi: [\vartheta, \omega] \subset R \to R$ is supposed to be seen curved if the subsequent dissimilarity clutches

$$\varphi(tx + (1-t)y \leq t\varphi(x) + (1-t)\varphi(y)$$

(Mitrinovic ,D.S.Pecaric ,J and Pecaric ,Jand Fink ,A.M.2013)

For all $x,y \in [\vartheta, \omega]$ and t∈ [0,1], the researchers declare that is curved in if $(-\varphi)$ is curved.

$R^{\propto}$ is the set of real numbers, $R^{\propto} = Q^{\propto} \cup J^{\propto}$,where $Q^{\propto}$ is the $\alpha-$ kind fixed set of the rational number accounts is demarcated as the group

$\left\{m^{\propto} = \left(\frac{p}{q}\right)^{\alpha}, p, q\epsilon Z, q \neq 0\right\}$,

In addition, $J^{\propto}$ is the $\alpha-$ the type set of irrational numbers is clarified as the fixed set.

$$\left\{m^{\propto} \neq \left(\frac{P}{q}\right)^{\alpha}, p, q\epsilon Z, q \neq 0\right\}.$$

The local fractional derivative of the function $\varphi(x)$ of demand α at $X = X_{\circ}$ is known as:

$$\varphi^{\alpha}(X_{\circ}) = \frac{d^{\alpha}\varphi(x)}{dx^{\alpha}}\Big|_{X=X_{\circ}} = \lim_{X\to X_{\circ}}\frac{\Delta^{\alpha}(\varphi(X)-\varphi(X_{\circ}))}{(X-X_{\circ})}$$

Where $\Delta^{\alpha}(\varphi(X)-\varphi(X_{\circ})) \cong \Gamma(\alpha+1)\big(\varphi(X)-\varphi(X_{\circ})\big)$.

If there occurs $\varphi^{(k+1)\alpha}(x) = D_x^{\alpha} \dots D_x^{\alpha}\varphi(x)$ for any $X \in I \subseteq R$, then we signified $\varphi \in D_{(k+1)\alpha}(I)$, wherever $k = 0,1,\dots$ (Dragomir,S.S and Agarwal,R.P,1998)

Anon –differentiable function $\varphi: R \to R^{\alpha}, X \to f(x)$ is termed as fractional locally continues at $X_{\circ}$. "If for whichever ∈> 0, there be existent $\delta > 0$, as that $|\varphi(x)-\varphi(X_{\circ})| < \epsilon^{\propto}$ holds for $|X-X_{\circ}| < \delta$, where $\epsilon, \delta \in R$. If $\varphi(x)$ is local incessant on the interlude (ϑ, ω) .We represent $\varphi(x) \in C_{\alpha}(\vartheta, \omega)$". (Dragomir,S.S and Agarwal,R.P,1998)

I call f is fractional integral if

$$\frac{1}{\Gamma(1+\alpha)}\int_{\vartheta}^{\omega}\varphi(x)(dt)^{\alpha}$$

$$= \frac{1}{\Gamma(1+\alpha)}\lim_{\Delta t\to 0}\sum_{j=0}^{n-1}\varphi(t_j)\left(\Delta t_j\right)^{\alpha}$$

$$< \infty \quad (3)$$

and the fractional integral is defined by:

$$\vartheta I_{\omega}^{\propto} f(x) = \frac{1}{\Gamma(1+\alpha)}\int_{a}^{\omega}\varphi(x)(dt)^{\alpha}$$

$$= \frac{1}{\Gamma(1+\alpha)}\lim_{\Delta t\to 0}\sum_{j=0}^{n-1}\varphi(t_j)\left(\Delta t_j\right)^{\alpha}$$

With $\Delta t_j = t_{j+1} - t$,and $\Delta t = max\{\Delta t_1, \Delta t_2, \dots, \Delta t_{n-1}\}$,where $[t_j, t_{j+1}]$, $j = 0, \dots, n-1$, and $\vartheta = t_0 < t_1 < \cdots < t_{n-1} = \omega$ is a partition of interval $[a, b]$. Here it follows that $\vartheta I_{\omega}^{\propto}\varphi(x) = 0$ if $\vartheta = \omega$ and $\vartheta I_{\omega}^{\propto}\varphi(x) = -\omega\ \vartheta I_{\omega}^{\propto}\varphi(x)$ if $\vartheta < \omega$.

Let $\varphi: I \subset R \to R^{\alpha}$. As such, any $X_1, X_2 \in I$and $\lambda \in [0,1]$, if the subsequent inequity $\varphi(\lambda X_1) + (1-\lambda)X_2 \leq \lambda^{\alpha} f(X_1) + (1-\lambda)^{\alpha}\varphi(X_2)$ grasps,

then f is named a widespread convex role on I.

Now, let us introduce our $L_{P,\propto}$ space for $0 < p < \infty$.

Let us define the fractional integral quasi normed space as:

$$L_{P,\propto}[\vartheta,\omega] = \left\{ \varphi: [\vartheta,\omega] \to R: \|\varphi\|_{P,\alpha} = \left(\int_{\vartheta}^{\omega} |\varphi(x)|^{p} \, (dx)^{\alpha} \right)^{\frac{1}{P}} < \infty \right\}$$

and $\|.\|_{P,\alpha}$ is a fractional L_P integrable norm.

2.Auxilary Results

Lemma 2.1 (Barnett,N.S. and Dragomir,S.S,2001):

$$\frac{d^{\alpha}f(x)}{dx^{\alpha}} = \frac{\Gamma(1+k\alpha)}{\Gamma(1+(k-1)\alpha)} X^{(k-1)\alpha}$$

$$\frac{1}{\Gamma(1+\alpha)} \int_{\vartheta}^{\omega} X^{k\alpha} (dx)^{\alpha} = \frac{\Gamma(1+k\alpha)}{\Gamma(1+(k+1)\alpha)} \left(\omega^{(k+1)\alpha} - \vartheta^{(k+1)\alpha}\right), k \epsilon R.$$

Lemma 2.2: (Meftah & Boukerrioua Khaled ,2017) GeneraliZed Holder inequality

Let φ', g $\in C_{\alpha}[\vartheta,\omega], p, q > 1$, with $\frac{1}{p} + \frac{1}{q} = 1$,

then

$$\frac{1}{\Gamma(1+\alpha)} \int_{\vartheta}^{\omega} |\varphi(x) g(x)| (dx)^{\alpha} \leq \left(\frac{1}{\Gamma(1+\alpha)} \int_{\vartheta}^{\omega} |\varphi(x)|^{p} (dx)^{\alpha} \right)^{\frac{1}{p}} \cdot \left(\frac{1}{\Gamma(1+\alpha)} \int_{\vartheta}^{\omega} |g(x)|^{q} (dx)^{\alpha} \right)^{\frac{1}{q}}.$$

Lemma 2.3 (Dragomir ,s.s and Pearce ,C.E.M(2000):Let $\varphi \in D_{\alpha}[\vartheta,\omega]$ with $\vartheta < \omega$ and $g(x) \in C_{\alpha}[\vartheta,\omega]$.If $\varphi^{\alpha} \in I_{x}^{(\alpha)}[\vartheta,\omega]$,then for all $x \in [\vartheta,\omega]$,the following indentity holds.

"$\varphi(\vartheta)\vartheta I^{(\propto)}{}_{x} g(s) + \varphi(\omega) x I^{(\propto)}{}_{\omega} g(s) - \vartheta I^{(\propto)}{}_{\omega} \varphi(s) g = \frac{1}{\Gamma(1+\alpha)} \int_{\vartheta}^{\omega} \left[\frac{1}{\Gamma(1+\alpha)} \int_{x}^{t} g(s)(ds)^{\alpha} \right] \boldsymbol{\varphi}^{(\propto)}(t)(dt)^{\alpha}$"

3.Main Results

Theorem 3.1:

let φ(x) ∈ $L_{p,\alpha}[\vartheta,\omega]$ and $\varphi^{\propto}$ is generalized convex in $L_p[\vartheta,\omega]$.

Then

$$\left|\varphi(\vartheta)_{a} I^{(\propto)}{}_{x} g(s) + \varphi(\omega)_{x} I^{(\propto)}{}_{\omega} g(s) - \vartheta I^{(\propto)}{}_{\omega} \varphi(s) g(s)\right| xs \leq \frac{((x-t)^{\alpha})^{\frac{1}{\bar{p}}}}{\Gamma(1+\alpha)^{p+q+1}} \cdot \frac{\Gamma(1+\alpha q)}{\Gamma(1+(q+1)\alpha)} \left(\omega^{(q+1)\propto} - \vartheta^{(q+1)\propto}\right) \|g(s)\|_{p,\propto}$$

$$where \quad 1 \leq p, q \leq \infty, \frac{1}{p} + \frac{1}{q} = 1.$$

Proof: By using lemma2.3, we get

"$\left|\varphi(\vartheta)_{\vartheta} I^{(\propto)}{}_{x} g(s) + \varphi(\omega)_{x} I^{(\propto)}{}_{\omega} g(s) - \vartheta I^{(\propto)}{}_{\omega} \varphi(s) g(s)\right| = \left| \frac{1}{\Gamma(1+\alpha)} \int_{\vartheta}^{\omega} \left[\frac{1}{\Gamma(1+\alpha)} \int_{x}^{t} g(s)(ds)^{\alpha} \right] \boldsymbol{\varphi}^{(\propto)}(t)(dt)^{\alpha} \right|$

Currently via employing general Holders inequality in lemma2.2, we gain

$$\left| \frac{1}{\Gamma(1+\alpha)} \int_{\vartheta}^{\omega} \left[\frac{1}{\Gamma(1+\alpha)} \int_{x}^{t} g(s)(ds)^{\alpha} \right] \boldsymbol{\varphi}^{(\propto)}(t)(dt)^{\alpha} \right| \leq \frac{1}{\Gamma(1+\alpha)} \left\{ \left[\int_{\vartheta}^{\omega} \left[\frac{1}{\Gamma(1+\alpha)} \int_{x}^{t} |g(s)|^{p} (ds)^{\alpha} \right]^{\frac{1}{p}} \left[\int_{\vartheta}^{b} \left| \varphi^{(\propto)}(t) \right|^{q} (dt)^{\alpha} \right]^{\frac{1}{q}} \right\} 1 \leq p, q \leq \infty, \frac{1}{p} + \frac{1}{q} = 1.$$

$= \frac{1}{\Gamma(1+\alpha)} (I_1 + I_2)$

Now,

$$I_1 = \left[\left|\int_{\vartheta}^{\varphi}\left[\frac{1}{\Gamma(1+\alpha)}\int_x^t |g(s)|^p (ds)^\alpha\right]\right|\right]^{\frac{1}{p}}$$

$$\leq \left[\left|\int_{\vartheta}^{\omega} |g(s)(ds)|^p\,(dt)^\alpha\right|\left|\frac{1}{\Gamma(1+\alpha)}\int_x^t (ds)^\alpha\right|\right]^{\frac{1}{p}}$$

by using lemma 2.1 and (1), we get,

$$I_1 = \left(\left|\frac{1}{\Gamma(1+\alpha)}\int_x^t |g(s)(ds)|^p (dt)^\alpha\right|\right)^{\frac{1}{p}}$$

$$\leq \|g(s)\|_{p,\propto}\left(\frac{(x-t)^\alpha}{\Gamma(1+\alpha)}\right)^{\frac{1}{p}}. \qquad (3)$$

By using lemma 2.1,we get,

$$I_2 = \left[\int_{\vartheta}^{\omega}\left|\varphi^{(\propto)}(t)\right|^q (dt)^\alpha\right]^{\frac{1}{q}}$$

$$= \frac{\Gamma(1+\alpha q)}{[\Gamma(1+\alpha)]^{\frac{1}{q}}\Gamma(1+(q+1)\alpha)}\left(\omega^{(q+1)\propto} - \vartheta^{(q+1)\propto}\right). \qquad (4)$$

Put (3) and (4) in (2), we get

$$\frac{1}{\Gamma(1+\alpha)}\left\{\left[\int_{\vartheta}^{\omega}\left[\frac{1}{\Gamma(1+\alpha)}\int_x^t |g(s)|^p (ds)^\alpha\right]\right]^{\frac{1}{p}}\left[\int_{\vartheta}^{b}\left|\varphi^{(\propto)}(t)\right|^q (dt)^\alpha\right]^{\frac{1}{q}}\right\}$$

$$= \frac{((x-t)^\alpha)^{\frac{1}{p}}}{\Gamma(1+\alpha)^{p+q+1}}\cdot\frac{\Gamma(1+\alpha q)}{\Gamma(1+(q+1)\alpha)}\left(\omega^{(q+1)\propto} - \vartheta^{(q+1)\propto}\right)\|g(s)\|_{p,\propto}$$

Now using (1),we catch

$$\left|\varphi(\vartheta)_a I^{(\propto)}{}_x g(s) + \varphi(\omega)_x I^{(\propto)}{}_\omega g(s) - \vartheta I^{(\propto)}{}_\omega \varphi(s)g(s)\right|$$

$$\leq \frac{((x-t)^\alpha)^{\frac{1}{p}}}{\Gamma(1+\alpha)^{p+q+1}}\cdot\frac{\Gamma(1+\alpha q)}{\Gamma(1+(q+1)\alpha)}\left(\omega^{(q+1)\propto} - \vartheta^{(q+1)\propto}\right)\|g(s)\|_{p,\propto}$$

$$where \qquad 1 \leq p,q \leq \infty, \frac{1}{p}+\frac{1}{q} = 1.$$

Also,

$$I_2 = \left[\int_{\vartheta}^{\omega}\left|\varphi^{(\propto)}(t)\right|^q (dt)^\alpha\right]^{\frac{1}{q}}$$

$$\leq [\Gamma(1 + \alpha)]^{\frac{1}{q}}\left[\frac{1}{\Gamma(1+\alpha)}\int_{\vartheta}^{\omega}\left|\varphi^{(\propto)}(t)\right|^q (dt)^\alpha\right]^{\frac{1}{q}}.$$

Corollary 3.2:

Let $g:[\vartheta,\omega]\to R^\alpha$ be a asymmetric to $(\vartheta+\omega)/2$. Then we have the a new Hadamard inequality.

"$$\left|\frac{(\varphi(\vartheta)+\varphi(\omega)}{2^\alpha} - \vartheta I^{\propto}_{\omega} g(s) - \vartheta I^{\propto}_{\omega}\omega(s)g(s)\right|$$

$$\leq \frac{\Gamma(1+\alpha q)\left(\left(\frac{\vartheta+\omega}{2}-t\right)^{\propto}\right)^{\frac{1}{p}}\|g(s)\|_{p,\propto}}{\left(\Gamma(1+(q+1)\alpha)\right)^{\frac{1}{q}}\left(\Gamma(1+\alpha)\right)^{\frac{1}{p+q+1}}}\left(b^{(q+1)\propto} - \vartheta^{(q+1)\propto}\right),$$

$$where \qquad 1 \leq p,q \leq \infty, \frac{1}{p}+\frac{1}{q} = 1."$$

Proof:

Put $x = \frac{\vartheta+\omega}{2}$ in theorem3.1, we get

$$\left|\varphi(\vartheta)_a I^{(\propto)}{}_{\frac{\vartheta+\omega}{2}} g(s) + \varphi(b)_{\frac{\vartheta+\omega}{2}} I^{(\propto)}{}_\omega g(s) - \vartheta_\omega \varphi(s)g(s)\right|$$

$$\leq \frac{\left(\left(\frac{\vartheta+\omega}{2}-t\right)^\alpha\right)^{\frac{1}{p}}}{\Gamma(1+\alpha)^{p+q+1}}\cdot\frac{\Gamma(1+\alpha q)}{\Gamma(1+(q+1)\alpha)}\left(\omega^{(q+1)\propto} - \vartheta^{(q+1)\propto}\right)\|g(s)\|_{p,\propto} \qquad (5)$$

Now,

using the symmetry of g , we have the following identity

$$\varphi(\vartheta)_{\vartheta}I^{(\propto)}_{\frac{\vartheta+\omega}{2}}g(s)+\varphi(b)_{\frac{\vartheta+\omega}{2}}I^{(\propto)}_{b}g(s)-\vartheta I^{(\propto)}_{\omega}\varphi(s)g(s)=\frac{\varphi(\vartheta)+\varphi(\omega)}{2^{\alpha}}-\vartheta I^{\propto}_{\omega}g(s)-\vartheta I^{\propto}_{\omega}\varphi(s)g(s) \quad (6)$$

Put (6) in (5), we get

$$\left|\frac{\varphi(\vartheta)+\varphi(\omega)}{2^{\alpha}}-\vartheta I^{\propto}_{\omega}g(s)-\vartheta I^{\propto}_{\omega}\varphi(s)g(s)\right| \leq \frac{\Gamma(1+\alpha q)\left(\left(\frac{\vartheta+\omega}{2}-t\right)^{\propto}\right)^{\frac{1}{\bar{p}}}\|g(s)\|_{p,\propto}}{\left(\Gamma(1+(q+1)\alpha)\right)^{\frac{1}{q}}\left(\Gamma(1+\alpha)\right)^{\frac{1}{p+q+1}}}\left(\omega^{(q+1)\propto}-\vartheta^{(q+1)\propto}\right).$$

Theorem 3.3: *Let $f(x)\in D_{\propto}[\vartheta,b]$ with $\vartheta<\omega$ and let $\varphi^{(\propto)}\in I^{(\alpha)}_{x}[\vartheta,\omega], g^{(\propto)}(x)\in C_{\alpha}[\vartheta,\omega]$.*

If $\left|\varphi^{(\propto)}\right|^{p/(p-1)}$ is generalized convex on [ϑ,ω] with p>1, then for all $x\in[\vartheta,\omega]$, the succeeding inequality grips

"$$\left|\varphi(\vartheta)_{a}I^{(\propto)}_{x}g(s)+\varphi(\omega)_{x}I^{(\propto)}_{\omega}g(s)-\vartheta I^{(\propto)}_{\omega}\varphi(s)g(s)\right| \leq \frac{((x-t)^{\alpha})^{\frac{1}{\bar{p}}}}{\Gamma(1+\alpha)^{\frac{p^2+p-1}{p-1}}}\cdot\frac{\Gamma\left(\frac{p-\propto+\alpha p}{p}\right)}{\Gamma\left(\frac{p-\propto+2\alpha p}{p}\right)}\left(\omega^{\frac{2\propto p-\propto}{p}}-\vartheta^{\frac{2\propto p-\propto}{p}}\right)\|g(s)\|_{p,\propto}$$

$$where \quad 1\leq p,q\leq\infty,\frac{1}{p}+\frac{1}{q}=1".$$

Proof: Let $x\in[\vartheta,\omega]$, by using lemma 2.3 for $\varphi^{(\propto)}$, we get

$$\left|\varphi(\vartheta)_{\vartheta}I^{(\propto)}_{x}g(s)+\varphi(\omega)_{x}I^{(\propto)}_{\omega}g(s)-\vartheta I^{(\propto)}_{\omega}\varphi(s)g(s)\right| = \left|\frac{1}{\Gamma(1+\alpha)}\int_{\vartheta}^{\omega}\left[\frac{1}{\Gamma(1+\alpha)}\int_{x}^{t}g(s)(ds)^{\propto}\right]\varphi^{(\propto)}(t)(dt)^{\propto}\right|$$

By using the generalized Holders disparity and the comprehensive convexity of $\left|\varphi^{(\propto)}\right|^{p/(p-1)}$, we get

$$\left|\varphi(\vartheta)_{\vartheta}I^{(\propto)}_{x}g(s)+\varphi(b)_{x}I^{(\propto)}_{\omega}g(s)-\vartheta I^{(\propto)}_{\omega}\varphi(s)g(s)\right| \leq \frac{1}{\Gamma(1+\alpha)}\left[\frac{1}{\Gamma(1+\alpha)}\int_{\vartheta}^{\omega}\left|\frac{1}{\Gamma(1+\alpha)}\int_{x}^{t}g(s)(ds)^{\propto}\right|^{p}(dt)^{\propto}\right]^{\frac{1}{\bar{p}}}\left[\int_{\vartheta}^{b}|(\varphi(t))^{\propto}|^{\frac{p}{p-1}}(dt)^{\propto}\right]^{\frac{p}{p-1}} = (M_1+M_2)^{\frac{1}{q}} \quad (8)$$

Now by using (3), we get

$$M_1 = \frac{1}{\Gamma(1+\alpha)}\left[\frac{1}{\Gamma(1+\alpha)}\int_{\vartheta}^{\omega}\left|\frac{1}{\Gamma(1+\alpha)}\int_{x}^{t}g(s)(ds)^{\propto}\right|^{p}(dt)^{\propto}\right]^{\frac{1}{\bar{p}}} \leq \|g(s)\|_{p,\propto}\frac{((x-t)^{\alpha})^{\frac{1}{\bar{p}}}}{\Gamma(1+\alpha)} \quad (9)$$

also,

$$M_2=\left[\int_{\vartheta}^{\omega}|(\varphi(t))^{\propto}|^{\frac{p}{p-1}}(dt)^{\propto}\right]^{\frac{p}{p-1}} \leq \left(\frac{1}{\Gamma(1+\alpha)}\right)^{\frac{p}{p-1}}\left[\frac{1}{\Gamma(1+\alpha)}\int_{\vartheta}^{\omega}\left|(\varphi(t))^{\frac{\propto p-\propto}{p}}\right|(dt)^{\propto}\right]^{\frac{p}{p-1}}$$

By using lemma 2.1, we get

$$"\left[\int_{\vartheta}^{\omega}\left|(\varphi(t))^{\propto}\right|^{\frac{p}{p-1}}(dt)^{\propto}\right]^{\frac{p}{p-1}} \leq \left(\frac{1}{\Gamma(1+\alpha)}\right)^{\frac{p}{p-1}}\frac{\Gamma\left(1+\frac{p\propto-\propto}{p}\right)}{\Gamma\left(1+\frac{2\alpha p-\propto}{p}\right)}\left(\omega^{\frac{2\propto p-\propto}{p}}-\vartheta^{\frac{2\propto p-\propto}{p}}\right)" \quad (10)$$

Put (9) and (10) in (8), we get

$$\left|\varphi(\vartheta)_{a}I^{(\propto)}_{x}g(s)+\varphi(\omega)_{x}I^{(\propto)}_{b}g(s)-\vartheta I^{(\propto)}_{\omega}\varphi(s)g(s)\right| \leq \frac{((x-t)^{\alpha})^{\frac{1}{\bar{p}}}}{\Gamma(1+\alpha)^{\frac{p^2+p-1}{p-1}}}\cdot\frac{\Gamma\left(\frac{p-\propto+\alpha p}{p}\right)}{\Gamma\left(\frac{p-\propto+2\alpha p}{p}\right)}\left(\omega^{\frac{2\propto p-\propto}{p}}-\vartheta^{\frac{2\propto p-\propto}{p}}\right)\|g(s)\|_{p,\propto} \quad (7)$$

$$where \quad 1\leq p,q\leq\infty,\frac{1}{p}+\frac{1}{q}=1.$$

Corollary3.4:

If $g:[\vartheta,\omega]\to R^{\alpha}$ be a symmetric to $(\vartheta+\omega)/2$. Then we have another new Hadamard inequality.

Then

$$\left|\frac{\varphi(\vartheta)+\varphi(\omega)}{2^{\propto}}\ {}_{\vartheta}I^{(\propto)}{}_{\omega}g(s) + -\vartheta I^{(\propto)}{}_{\omega}\varphi(s)g(s)\right| \le \frac{\left(\left(\frac{\vartheta+\omega}{2}-t\right)^{\alpha}\right)^{\frac{1}{p}}}{\varphi\Gamma(1+\alpha)^{\frac{p^2+p-1}{p-1}}} \cdot \frac{\Gamma\left(\frac{p-\propto+\alpha p}{p}\right)}{\Gamma\left(\frac{p-\propto+2\alpha p}{p}\right)}\left(\omega^{\frac{2\propto p-\propto}{p}} - \vartheta^{\frac{2\propto p-\propto}{p}}\right)\|g(s)\|_{p,\propto}$$

$$where \qquad 1\le p,q\le\infty, \frac{1}{p}+\frac{1}{q}=1.$$

Proof:

Put $x=\frac{\vartheta+b}{2}$ in theorem 3.3 , we come to be

$$\left|\varphi(\vartheta)_{a}I^{(\propto)}{}_{\frac{\vartheta+\omega}{2}}g(s)+\varphi(b)_{\frac{\vartheta+\omega}{2}}I^{(\propto)}{}_{\omega}g(s) - \vartheta I^{(\propto)}{}_{\omega}\varphi(s)g(s)\right| \le \frac{((x-t)^{\alpha})^{\frac{1}{p}}}{\Gamma(1+\alpha)^{\frac{p^2+p-1}{p-1}}} \cdot \frac{\Gamma\left(\frac{p-\propto+\alpha p}{p}\right)}{\Gamma\left(\frac{p-\propto+2\alpha p}{p}\right)}\left(\omega^{\frac{2\propto p-\propto}{p}} - \vartheta^{\frac{2\propto p-\propto}{p}}\right)\|g(s)\|_{p,\propto} \qquad (11)$$

Now,

Utilizing the regularity of g , the researchers will have the resulting characteristics.

$$\varphi(\vartheta)_{\vartheta}I^{(\propto)}{}_{\frac{\vartheta+\omega}{2}}g(s)+\varphi(\omega)_{\frac{\vartheta+\omega}{2}}I^{(\propto)}{}_{b}g(s) - \vartheta I^{(\propto)}{}_{\omega}\varphi(s)g(s) = \frac{\varphi(\vartheta)+\varphi(\omega)}{2^{\propto}}\ {}_{\vartheta}I^{(\propto)}{}_{\omega}g(s) + -\vartheta I^{(\propto)}{}_{\omega}\varphi(s)g(s) \qquad (12)$$

Put (12) in (11), we change it to,

$$\left|\frac{\varphi(\vartheta)+\varphi(\omega)}{2^{\propto}}\ {}_{\vartheta}I^{(\propto)}{}_{\omega}g(s) + -\vartheta I^{(\propto)}{}_{\omega}\varphi(s)g(s)\right| \le \frac{\left(\left(\frac{\vartheta+\omega}{2}-t\right)^{\alpha}\right)^{\frac{1}{p}}}{\Gamma(1+\alpha)^{\frac{P^2+P-1}{P-1}}} \cdot \frac{\Gamma\left(\frac{p-\propto+\alpha p}{p}\right)}{\Gamma\left(\frac{p-\propto+2\alpha p}{P}\right)}\left(b^{\frac{2\propto p-\propto}{p}} - \vartheta^{\frac{2\propto p-\propto}{p}}\right)\|g(s)\|_{p,\propto}.$$

References:

Alomari, M., & Daru, M. W. (2010). Some Ostrowski's type inequalities for convex functions with application. RGMIA Research Report Collection, 13(1), Article 8.

Barnett, N. S., & Dragomir, S. S. (2001). An Ostrowski type inequality for double integrals and applications for cubature formulae. Soochow Journal of Mathematics, 27(1), 109–114.

Bullen, P. S. (1978). Error estimates for some elementary quadrature rules. Publikacije Elektrotehničkog Fakulteta, Serija Matematika i Fizika, (602–633), 97–103.

Chen, G.-S. (2013). Generalizations of Hölder's and some related integral inequalities on fractal space. Journal of Function Spaces and Applications, 2013, Article ID 198405. https://doi.org/10.1155/2013/198405

Dragomir, S. S., & Agarwal, R. P. (1998). Two inequalities for differentiable mappings and applications to special means of real numbers and to trapezoidal formula. Applied Mathematics Letters, 11(5), 91–95. https://doi.org/10.1016/S0893-9659(98)00086-X

Dragomir, S. S., & Pearce, C. E. M. (2000). Selected topics on Hermite–Hadamard inequalities and applications. RGMIA Monographs, Victoria University.

El Farissi, A. (2010). Simple proof and refinement of Hadamard inequality. Journal of Mathematical Inequalities, 4(3), 365–369.

Bhayah, E. S. (1999). A study on approximations of bounded measurable functions with some discrete series in Lp spaces ($0 < p < \infty$) (Master's thesis).

Hadamard, J. (1893). Étude sur les propriétés des fonctions entières et en particulier d'une fonction considérée par Riemann. Journal de Mathématiques Pures et Appliquées, 58, 171–215.

Meftah, M., & Boukerrioua, K. (2017). Some new Ostrowski type inequalities on time scales for functions of two independent variables. Journal of Interdisciplinary Mathematics, 20(2), 397–415. https://doi.org/10.1080/09720502.2015.1026463

Meftah, M., Merad, M., & Souahi, A. (2019). Fractional Ostrowski type inequalities for functions whose mixed derivatives are prequasiinvex functions. Journal of Interdisciplinary Mathematics, 22(6), 951–967. https://doi.org/10.1080/09720502.2019.1696562

Mitrinović, D. S., Pečarić, J. E., & Fink, A. M. (2013). Classical and new inequalities in analysis (Vol. 61). Springer Science & Business Media.

PURE SCIENCES
International Journal of Kerbala

Pure Sciences International Journal of Kerbala

Year: 2025 Volume : 2 Issue : 8 ISSN: 6188-2789 Print 3005 -2394 Online

2025,Volume 2 , Issue 8 , PSIJK (64-70)

Pure Sciences International Journal of Kerbala

Effects of Valerian and ST36 Acupuncture on Kidney and Liver Function in Rats

Haneen Seed Mohsin Al-Mosawei [a*], Batool Luay Aziz [a], Hassan Mahmood Mousa Abo Almaali [b]

[a*] Department of Pharmaceutical Chemistry, College of Pharmacy, University of Kerbala.Iraq
[b] Branch of Clinical Laboratory Sciences , College of Pharmacy, University of Kerbala. Iraq

P A P E R I N F O

Received: 04.12.2025
Accepted: 20.12.2025
Published: 31.12.2025

Keywords:
Valerian, acupuncture, ST36, liver function, kidney function and rats.

A b s t r a c t

Numerous dosages and formulations have been used in past studies of this ancient herbal sleep aid, valerian, utilizing a range of experimental methods. The purpose of this study is to assess how long-term valerian usage and acupuncture at ST36 affect kidney and liver function, with a focus on alterations in enzyme levels and general organ health. After the plant was ground, 4 g of the resulting powder was weighed and placed in a plastic container. The powder was then mixed with 100 milliliters of distilled water and left to steep for 15 minutes at 100°C. The mixture was then filtered through filter paper. After extracting four grams of the powdered plant material in 100 milliliters of distilled water at 100 degrees Celsius for fifteen minutes, the mixture was filtered. Rats were given the extract (40 mg/mL) orally at a dose of 400 mg/kg body weight (10 mL/kg).Before the experiment started, 32 rats (weighing 200–300 g) were kept in the lab for a week. Rats were housed in cages with free access to food and tap water. The Ethics Committee of Karbala University, Karbala, Iraq, authorized the experimental protocol and methods utilized in this study for the care and use of lab animals. The rats were randomly divided into four groups, each containing eight rats. No significant difference is noticed among study groups with control according to liver and kidney function tests (BUN, AST), except modest elevation of ALP in Valerian with acupuncture. Velerian extract did not significantly cause hepatorenal damage in rats under the study's settings. Biochemical indicators were not significantly changed by acupuncture at ST36, indicating a neutral modulatory impact.

DOI: 10.53851/psijk.v2i8.64-70

1.INTRODUCTION

Valerian is a plant supplement frequently used to encourage relaxation and sleep. Although its exact modes of action are unknown, it is thought to interact with the brain's GABA receptors (Varshney, et al., 2024). Acupuncture at ST36 (Zusanli): This popular acupuncture point is frequently used to reduce pain, increase immunity, and control digestion.

According to Traditional Chinese Medicine (TCM), it is essential for controlling digestion, enhancing immunity, and reducing pain. It is regarded as a critical site for general health, including liver and renal functions (Liu, et al., 2023). According to TCM, the kidneys and liver are interdependent and essential for general health. The liver is in charge of blood flow, cleansing, and emotional equilibrium, whereas the kidney controls water metabolism, reproduction, and bone growth (Han BH, et al.,2016). Based on their unique characteristics and the interdependence of these organs in TCM, we can draw some educated conclusions about the combined effects of valerian and acupuncture at ST36 on kidney and liver functions, even though there is little direct study on this topic (Armour, et al.,2015). According to

*Corresponding Author Institutional Email
haneen.s@uokerbala.edu.iq (Haneen Seed Mohsin)

certain research, valerian may have a diuretic effect that could affect renal function. However, further investigation is required to validate it. In TCM, valerian is frequently employed in the areas of sleep and relaxation, which are strongly related to the kidneys. Therefore, by encouraging sound sleep, valerian may indirectly enhance kidney health (Dalla Corte, et al.,2008). It is unclear what effect Valerian could have on the liver. However, long-term use of any chemical, including herbal supplements, should be monitored because the liver plays a role in detoxification (Jones, et al., 2000). At ST36, acupuncture is generally regarded as safe and beneficial for a number of medical issues. According to TCM, ST36 controls the digestive tract, which obliquely promotes liver and kidney function. Depending on a thorough TCM diagnostic, certain practitioners may utilize ST36 to treat particular liver or kidney abnormalities (Wang , et al., 2023). Individual Variability: Acupuncture and valerian responses might differ greatly from person to person. Long-term consequences: Although valerian is widely regarded as safe for short-term usage, its long-term consequences are not as well established (Bone, et al., 2013). Drug Interactions: It is important to speak with a healthcare professional because Valerian may interact with some drugs. TCM Diagnosis: In order to effectively treat underlying imbalances, acupuncture, even at ST36, should be founded on a correct TCM diagnosis. In conclusion, even if acupuncture and valerian at ST36 may be beneficial, it's important to use them carefully and under the supervision of trained specialists. For a thorough assessment, speak with a medical professional or a TCM practitioner if you have concerns about your kidney or liver function(McPherson , et al., 2015). The current study aims to ascertain whether Valerian damages the liver and whether acupuncture at age 36 could lessen such harm. Nevertheless information about valerian's possible hepatorenal toxicity is still scarce and inconsistent despite the plant's widespread use. Furthermore, not enough research has been done on the modulatory effect of acupuncture at ST36 on valerian-induced biochemical alterations.

2.Material And Methods

2.1Animal:

Four grams of the powdered plant were weighed and put in a plastic container. After that, the powder was combined with 100 milliliters of distilled water and steeped at 100 degrees Celsius for 15 minutes. The aqueous extract was then obtained by filtering the mixture with filter paper. Male rats between the ages of 45 and 90 days were used in the study; their mean body weight ± SD was 209.97 ± 25.84 g. Before the experiment, thirty-two rats weighing between 200 and 300 g were kept in the lab for a week to acclimate. Under typical laboratory circumstances, the animals were kept in wire-floored cages with unrestricted access to food and tap water. For 28 days in a row, the aqueous plant extract (40 mg/mL) was given orally by gastric gavage at a dose of 400 mg/kg body weight, once daily. The experimental technique and procedures used in this work for the care and use of lab animals were approved by the College of Pharmacy Karbala University Ethics Committee under (Project No: 2023An.22) in Karbala, Iraq. Four groups of eight rats were randomly selected from among the animals. Daily dosages of valerian and acupuncture are administered. Since group 1 was not given any medication (control), group 2 I was given valerian without acupuncture , group 3 I was given valerian with acupuncture ,group 4 I was given acupuncture acupuncture only, respectively shows that there is in Fig-1.After extracting four grams of the powdered plant material in 100 milliliters of distilled water at 100 degrees Celsius for fifteen minutes, the mixture was filtered. Rats were given the extract (40 mg/mL) orally at a dose of 400 mg/kg body weight (10 mL/kg).

2. Method: After extracting four grams of the powdered plant material in 100 milliliters of distilled water at 100 degrees Celsius for fifteen minutes, the mixture was filtered. For 28 days in a row, rats were given the extract (40 mg/mL) orally by gastric gavage at a dose of 400 mg/kg body weight once daily.

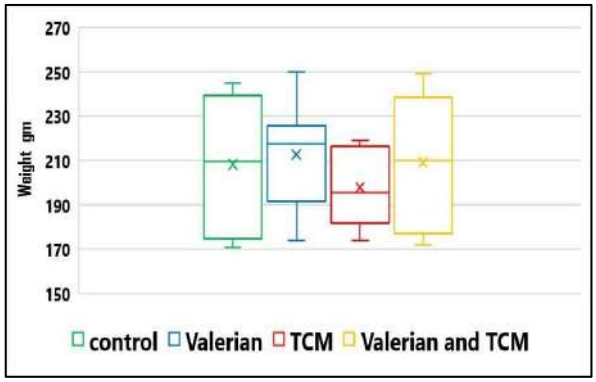

Figure 1. Effect of Valerian and/or TCM on Body Weight,g,Differences between groups were considered statistically significant at $p < 0.05$.(Adjust this sentence if no significant difference was found.

Preparation of the plant's aqueous extract (Valerian): Four grams of the ground plant stem were weighed and stored in a plastic container. After that, 100 milliliters of distilled water were added to 4 grams, of herb powder, and the mixture was allowed to mingle for 15 minutes. After passing the combination through filter paper, the liquid that was left behind was left to dry at about 37°C shows that there is in Table -1.

Table 1:The study conducted on male rats with age 45 to 90 day with mean weight ± SD 206.97 ±25.87 gm

Names Of Tests	Normal range	Unit
Alkaline phosphatase (ALP)	44 – 147	U/L
blood urea nitrogen (BUN)	5 – 20	mg/dL
Glutamic oxaloacetic transaminase (SGOT/ AST)	8 – 45	IU/l

Tables 2: Normal Reference Ranges of Selected Blood Biochemical Tests

Mean	206.97
Standard Deviation	25.87
Minimum	171.00
Maximum	250.00
Count	32
Confidence Level (95.0%)	9.33

Table 3. Effect of Valerian and ST36 on AST, ALP, and BUN mean serum values in the experimental groups

Groups	BUN	ALP	GOT (AST)
Control	33	97	41
Valerian Without acupuncture	31.7	113	43
Valerian with acupuncture	42	187	54
Only acupuncture	30.7	125	31

Acupuncture: Acupuncture was performed once daily at the ST36 point in rats, with a needle insertion depth of 2 mm and a retention time of 2 minutes per session, continuing until the end of the experiment.

Statistical analysis: According to previous research, herbal remedies like Valeriana officinalis (Valerian), whether used on their own or in a clinical setting, have not been significantly linked to hepatotoxicity or serious liver damage. These findings are in line with those findings. The discussion section should provide a thorough examination of the data' implications, limits, and applicability to the body of current literature, however these findings should be interpreted cautiously.It is crucial to remember that any hazards related to herbal supplements are not excluded just because there were no statistically significant results.

RESULTS

The initial values for the biomarkers under study are shown in Table 1. The control group's Alkaline phosphatase (ALP), blood urea nitrogen (BUN), Glutamic oxaloacetic transaminase (SGOT/ AST), were generally within normal limits. These measurements also showed that the second group had slightly lower BUN levels and somewhat higher ALP and GOT levels as shown in Tables 2.

Table 4: The output for the pairwise comparisons (Tukey HSD) among study groups

Biomarker	Group Comparison	Mean Difference	p-value	Significance
AST	Control vs Valerian	-1.3	0.45	No
AST	Control vs Acupuncture	-1.9	0.31	No
AST	Control vs Valerian with Acupuncture	8.3	0.60	No

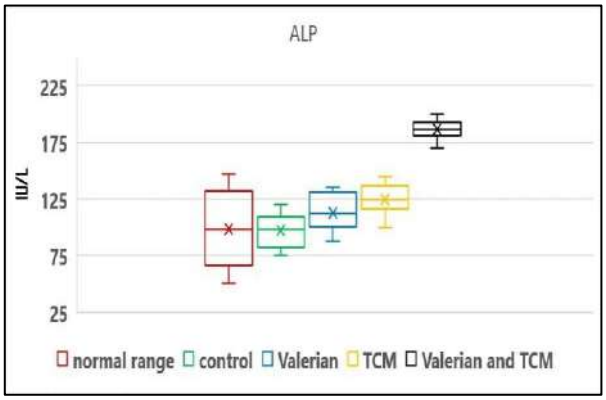

Figure.2. Effect of TCM and/or Valerian on Alkaline Phosphatase (ALP) Levels, IU/L Data are presented as mean ± SD. When compared to the control group, differences were deemed statistically significant at $p < 0.05$.

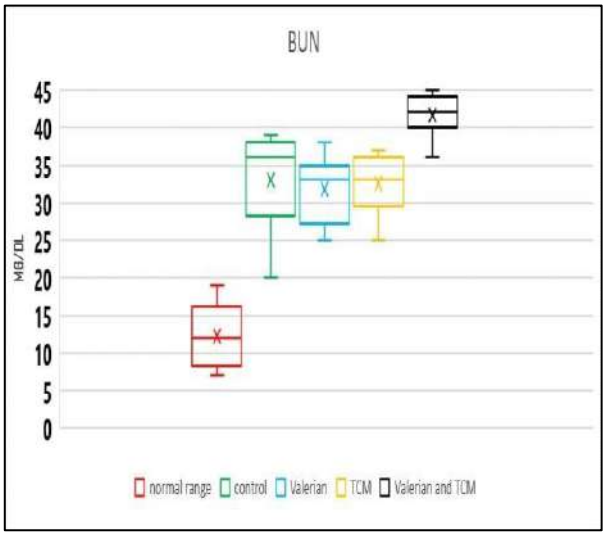

Figure 3. Impact of TCM and/or Valerian on Blood Urea Nitrogen (BUN) Levels, IU/L,

The experimental groups showed statistically significant differences ($p < 0.05$).

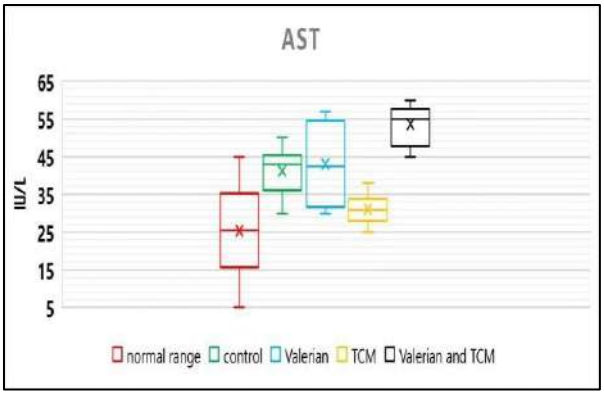

Figure 4. Impact of TCM and/or Valerian on Aspartate Aminotransferase (AST) Activity,IU/L At $p < 0.05$, the results revealed significant group differences.

Using p-values greater than 0.05 for every parameter examined, the statistical analysis of the current study showed no significant differences between treatment groups. Since the p-value is greater than the significance level of 0.05, we fail to reject the null hypothesis for all parameters analyzed. This analysis shows no statistically significant association between the treatment groups and the parameters measured based on the data provided.Aim of study: The present study aimed to evaluate the potential hepatorenal effects of valerian extract in rats and to assess whether acupuncture at ST36 modulates these effects.

Discussion And Conclusio

The primary conclusion of this study is that, in the experimental setting, valerian extract did not significantly cause hepatorenal damage.

Evaluation of Hepatorenal Effects of Valerian Extract With and Without ST36 Acupuncture in Rats.Depending on the pattern of increase, these tests can help organize a differential diagnosis and identify a possible site of liver injury. Increases in GOT that are out of proportion to increases in bilirubin and alkaline phosphatase are indicative of hepatocellular illness (Jaeschke, et al., 2011). (Table 3). On the other hand, blood tests known as kidney function tests are used to evaluate the kidneys' level of functioning (Jaeschke, et al., 2011). Improved sleep, decreased anxiety, relaxed muscles, and possible relief from menstrual cramps are just a few of the physiological advantages that Valerian provides (Table 3). It contains antioxidant qualities and may help cardiovascular health by reducing blood

pressure brought on by stress. Additionally, it can aid with digestive problems brought on by stress, ADHD symptoms, and restlessness (Sahin, et al., 2024).

The objectives of the current investigation are to assess The lack of severe liver damage in the current investigation restricts inferences about the preventive role of acupuncture at ST36, despite reports that it has hepatoprotective benefits in some disease models.

levels in the control group were within normal ranges, indicating differences in liver and kidney function biomarkers between treatment groups. ALP and GOT levels were marginally higher in the Valerian group that did not get acupuncture, and BUN levels wee lower (Tables 2 and 3).

In contrast to the acupuncture-only group, Valerian, who received acupuncture, showed additional gains in all metrics (Table 3). It is important to use caution when interpreting the slight increase in ALP seen in the valerian plus acupuncture group, as it may indicate a physiological variation rather than a pathological alteration. This implies that a dose of 2 g was safe because liver function was still in a decent state. Furthermore, ST 36 could not considerably reduce valerian's harmful effects, which means that it cannot be used to treat poisoning caused by valerian herbs. The data show that valerian is safe for the kidneys and has no substantial effect on blood creatinine levels, despite the fact that there is no noticeable effect (Authors et al., 2012). Nevertheless, it has been demonstrated that ST36 has no effect in preserving or reducing blood creatinine levels. Therefore, ST36 might not be an effective supplemental treatment for renal toxicity (Pistolesi, et al., 2019).

There are two groups of traditional biomarkers for liver injury: first, those that hint at a disruption in normal liver function or homeostasis, and second, those that provide specific indicators of tissue and cellular damage. The liver processes bile acids and other endogenous compounds, synthesizes proteins, and excretes metabolic waste products such urea and bilirubin as shown in Table 3 (Thakur, et al., 2024),.

Conventional indicators of compromised liver function include changes in plasma bile acids, plasma total bilirubin, and total plasma protein brought on by medications or illnesses. These indicators can be evaluated because injured or dying cells frequently release them into the bloodstream. This group of enzymes includes gamma-glutamyl transferase, glutamate dehydrogenase, aspartate aminotransferase (AST) ,(Boone L, et al., 2005). Other readily available alternatives include triglycerides, albumin, total protein, and coagulation tests. Even though there are several biomarkers for hepatotoxicity detection, more study is still needed in this field. Additionally, it was discovered in this study that Valerian suppressed the serum levels of AST, an enzyme that is pyridoxal phosphate-dependent and was elevated by DEN therapy. AST is frequently evaluated clinically as a sign of liver health and is typically found in the liver, as shown in Table 3, in the heart, skeletal muscle, kidneys, brain, and red blood cells.

Consistent with our findings, a prior study in rats and mice following DEN injection demonstrated an AST rise in the rat blood serum and its inhibition by possible chemopreventive drugs shown in Table- 3, Evaluation of Hepatorenal Effects of Valerian Extract With and Without ST36 Acupuncture in Rats (Kakehashi ,et al., 2014).

Symptoms may not be fully explained by changes in ghrelin levels following treatment. However, ghrelin may be one of the numerous potential causes behind the acupuncture mechanism for FD, and our work will contribute to the body of evidence supporting this theory. Many people believe that acupuncture is multilayered, multitargeted, and multieffective; it can help those with long-term liver problems. Recent studies have demonstrated that acupuncture treatment improves structural, cellular, and molecular biology, as shown in Tables 3 and 4, among other levels. The main way that acupuncture has a therapeutic impact on patients is by enhancing liver function (Qi, et al., 2020).

Acupuncture's therapeutic mechanisms include preventing the activation and proliferation of hepatic stellate cells, lowering oxidative stress, suppressing the inflammatory response, and encouraging hepatocyte lipid metabolism (Iwa, et al., 2006). In animal experiments, acupuncture has been shown to improve LC tissues and gastrointestinal motility. According to several animal studies, acupuncture encourages the liver tissue's extracellular matrix to degrade. This may be because it inhibits the PDGF signaling route or activates the TGF-β/Smad signaling pathway.

Studies in animals also demonstrated that acupuncture reduces inflammatory reactions brought on by dyslipidemia by controlling Kupffer cell contain receptors, including complement, scavenger, and pattern recognition receptors, as shown in Table 4. Following acupuncture treatment, the liver showed decreased extracellular matrix, thinning of fibrous septa, and mitigation of necrosis brought on by inflammatory

reactions. More significantly, controlled clinical trials have also demonstrated these beneficial effects (Kulkarni, et al., 2017).

Specific efficacy criteria, including liver function immunoglobulin indices, liver fibrosis indicators, and ascites-related indexes, were used in all included trials. They all stated that acupuncture is a dependable and safe treatment; nevertheless, no adverse side effects were highlighted. As a result, there is little proof that acupuncture is safe, as shown in Table- 4(Qi, et al., 2020).).

Comparison with Existing Literature

Hepatotoxicity of Valerian

Valerian has been linked to liver damage, according to a study; however, these instances are not common. According to research, although there have been a few cases of drug-induced liver injury (DILI) linked to Valerian, these have frequently happened in combination with other herbal remedies or prescription drugs. In particular, a case report of a patient who developed jaundice after taking a Valerian-containing cold medication revealed markedly elevated liver enzymes (ALT 1191 U/L), which returned to normal following steroid treatment, as shown in Tables 2 and 3. This is consistent with the current study's findings that groups taking Valerian had elevated liver enzymes (Kulkarni, et al., 2017).

Conclusion:Velerian extract did not significantly cause hepatorenal damage in rats under the study's settings. Biochemical indicators were not significantly changed by acupuncture at ST36, indicating a neutral modulatory impact.

Acupuncture Effects

According to the current study, less is known about how acupuncture affects liver function. There is little specific research on acupuncture's direct effects on hepatotoxicity, despite some literature suggesting it may be helpful for several illnesses, including stress-related problems that may have an indirect impact on liver health. More thorough research is required to prove certain benefits shown in Table 3 (Li, et al., 2019).

REFERENCES

Armour, M. J. (2015). *The effectiveness of acupuncture in the treatment of primary dysmenorrhea: A mixed methods study* (Doctoral dissertation, University of Western Sydney, Australia).

Bone, K., & Mills, S. (2013). *Principles and practice of phytotherapy: Modern herbal medicine* (2nd ed.). Elsevier Health Sciences. https://doi.org/10.1016/C2009-0-48725-7

Boone, L., Meyer, D., Cusick, P., et al. (2005). Selection and interpretation of clinical pathology indicators of hepatic injury in preclinical studies. *Veterinary Clinical Pathology, 34*(3), 182–188. https://doi.org/10.1111/j.1939-165X.2005.tb00041.x

Dalla Corte, C. L., Fachinetto, R., Colle, D., Pereira, R. P., Avila, D. S., Villarinho, J. G., & Rocha, J. B. T. (2008). Potentially adverse interactions between haloperidol and valerian. *Food and Chemical Toxicology, 46*(7), 2369–2375.

Han, B. H. (2016). *Therapy of social medicine* (pp. 65–191). Springer.

Iwa, M., Matsushima, M., Nakade, Y., et al. (2006). Electroacupuncture at ST-36 accelerates colonic motility and transit in freely moving conscious rats. *American Journal of Physiology – Gastrointestinal and Liver Physiology, 290*(2), G285–G292. https://doi.org/10.1152/ajpgi.00419.2004

Jaeschke, H. (2011). Reactive oxygen and mechanisms of inflammatory liver injury: Present concepts. *Journal of Gastroenterology and Hepatology, 26*, 173–179. https://doi.org/10.1111/j.1440-1746.2010.06592.x

Jones. (2000). *The antibiotic alternative: The natural guide to fighting infection and maintaining a healthy immune system*. Inner Traditions/Bear & Company.

Kakehashi, A., Kato, A., Ishii, N., Wei, M., Morimura, K., Fukushima, S., & Wanibuchi, H. (2014). Valerian inhibits rat hepatocarcinogenesis by activating GABA(A) receptor-mediated signaling. *PLoS One, 9*(2), e88766. https://doi.org/10.1371/journal.pone.0088766

Kalas, M. A., Chavez, L., Leon, M., Taweesedt, P. T., & Surani, S. (2021). Abnormal liver enzymes: A review for clinicians. *World Journal of Hepatology, 13*(11), 1688. https://doi.org/10.4254/wjh.v13.i11.1688

Kulkarni, A., Arif, H., & Holleran, K. (2017). Valerian root: Is it safe for the liver? *American Journal of Gastroenterology, 112*(Suppl), S1569. https://doi.org/10.14309/00000434-201710001-02941

Li, X., Zhang, Y., Chen, H., & Wang, L. (2019). Acupuncture and liver health: A review of potential mechanisms and therapeutic benefits. *Journal of Hepatic Research, 45*(2), 123–130. https://doi.org/10.1016/j.jhep.2019.03.012

Liu, J., & Gong, C. (2023). Overview of local mechanism of acupuncture analgesia. *International Journal of Clinical Acupuncture, 32*(3). https://doi.org/10.3103/S104719792303006

McPherson, F. (2015). Herbal therapy and nutritional supplements. In T. Woo & M. Robinson (Eds.), *Pharmacotherapeutics for advanced practice nurse prescribers* (pp. 129–…). F. A. Davis Company.

Pistolesi, V., Morabito, S., Di Mario, F., Regolisti, G., Cantarelli, C., & Fiaccadori, E. (2019). A guide to understanding antimicrobial drug dosing in critically ill patients on renal replacement therapy. *Antimicrobial Agents and Chemotherapy, 63*(8), e00128-19. https://doi.org/10.1128/AAC.00128-19

Qi, L., Li, S., Xu, J., Xu, J., Lou, W., Cheng, L., & Zhang, C. (2020). Acupuncture for the treatment of liver cirrhosis: A meta-analysis. *Gastroenterology Research and Practice, 2020*, Article ID 4054781. https://doi.org/10.1155/2020/4054781

Sahin, K., Gencoglu, H., Korkusuz, A. K., Orhan, C., Aldatmaz, İ. E., Erten, F., Er, B., Morde, A., Padigaru, M., & Kilic, E. (2024). Impact of a novel valerian extract on sleep quality, relaxation, and GABA/serotonin receptor activity in a murine model. *Antioxidants, 13*(6), 657. https://doi.org/10.3390/antiox13060657

Steg, P. G., James, S. K., Atar, D., Badano, L. P., Lundqvist, C. B., et al. (2012). ESC Guidelines for the management of acute myocardial infarction in patients presenting with ST-segment elevation. *European Heart Journal, 33*(20), 2569–2619.

Thakur, S., Kumar, V., Das, R., Sharma, V., & Mehta, D. K. (2024). Biomarkers of hepatic toxicity: An overview. *Current Therapeutic Research*, 100737. https://doi.org/10.1016/j.curtheres.2024.100737

Varshney, M., Saha, S., Prinsa, P., & Jakhmola, V. (2024). Sleep disorder and its treatment: From nature to laboratory. *Majalah Obat Tradisional, 29*(1), 14–36. https://doi.org/10.22146/mot.86645

Wang, J., & Wang, F. (2023). Current acupuncture research. In *Explorations of traditional Chinese medicine: Insights for science education* (p. 149).

PURE SCIENCES
International Journal of Kerbala

Pure Sciences International Journal of Kerbala

Year: 2025 Volume : 2 Issue : 8 ISSN: 6188-2789 Print 3005 -2394 Online

2025,Volume 2 , Issue 8 , PSIJK (71-78)

Pure Sciences International Journal of Kerbala

Predicting Human Brain Age from MRI Data Using Deep CNNs Enhanced by MRMR

Dunya Hakim Hammood [a*], Ali Hassan Khudair [b]

[a *] *College of Education for Pure Sciences, University of Kerbala*
[b] *Department of Computer Science, Al-Nahrain University, Baghdad, Iraq*

P A P E R I N F O

Received: 17.12.2025
Accepted: 22.12.2025
Published: 31.12.2025

Keywords:
Brain age, MRI images, MRMR algorithm, convolutional neural network

A B S T R A C T

Predicting the age of the brain using MRI is an advanced medical method that is used to diagnose brain diseases and disorders such as Alzheimer's, multiple sclerosis and other neurological diseases. Using this method, brain MRI images are analyzed using advanced algorithms and neural networks to obtain different brain characteristics such as brain volume and cortical thickness. Then, by comparing these features with the MRI imaging data of other patients, the age of the brain is estimated. In this work, used Convolutional Neural Network (CNN) and MRMR feature selection algorithm. In this method, brain MRI images are processed by a convolutional network to extract age-related features, the MRMR algorithm selects the most relevant features, and the brain age is predicted using regression layers. The main contribution of this research is in adding a feature selection layer based on the MRMR feature ranking algorithm among the layers of a deep convolutional network, which has led to the improvement of the performance of the proposed convolutional network. Based on the obtained simulation results, the prediction accuracy of the proposed method for predicting the brain age of people is 90.3%, which has improved compared to the compared works.vements.

DOI: 10.53851/psijk.v2.i8.71-78

1. INTRODUCTION

Magnetic Resonance Imaging (MRI) provides detailed and reliable insights into brain structure and neurological health. However, accurately predicting brain age from MRI data remains a challenging task due to the influence of multiple factors, including genetic variability, lifestyle, environmental conditions, and neurological disorders. Recent studies have shown that deep learning models can estimate brain age by extracting discriminative features from MRI images, such as brain volume and cortical structural patterns. Nevertheless, the predictive performance of these models is highly dependent on the size, diversity, and quality of the available datasets, and MRI data alone cannot be considered a definitive diagnostic tool for brain aging. Consequently, clinical assessment should integrate imaging findings with complementary patient information, including medical history, clinical examinations, and observed symptoms (Cole et al., 2018; Bashyam et al., 2020) The present study investigates the use of deep learning approaches, particularly convolutional neural networks (CNNs), for predicting brain age directly from raw MRI images, with the aim of enhancing model robustness and prediction reliability (Bashyam et al., 2020).

*Corresponding Author Institutional Email
dunya.h@uokerbala.edu.iq (Dunya Hakim)

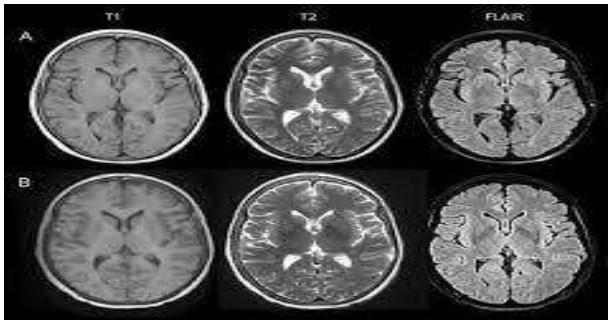

Figure 1: An image example of MRI (Rebelo-Marques, A., et al. ,2018).

Aging causes molecular and structural changes in tissues and organs, which are not fully understood (Rebelo-Marques, A., et al., 2018). These changes affect health, function, and disease susceptibility (Harman, D, 2006).MRI provides non-invasive access to brain structure, allowing machine learning models to capture age-related variations. Identifying biomarkers of aging can enable earlier and more accurate prediction of age-related diseases and lifespan differences.

The use of MRI to predict brain age began in the 1990s, analyzing structural differences across age groups. Initial studies with over 200 participants showed brain volume changes with age, particularly in the frontal and cerebral cortex. Advances in neuroimaging and intelligent algorithms improved prediction accuracy. In 2002, UCLA researchers estimated brain age with 95% accuracy using neural networks. In 2009, the University of Pennsylvania achieved 91% accuracy with combined image processing and algorithms. Later, convolutional neural networks enabled up to 96% accuracy for Alzheimer's patients. Today, MRI-based brain age prediction continues to advance with deep learning technologies (Cole et al., 2018).

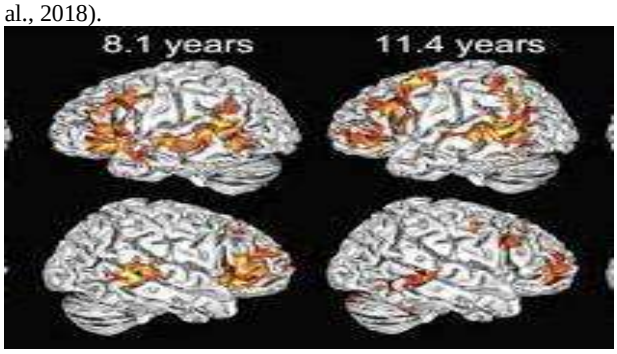

Figure 2: Sample image of brain age prediction (Cole, J. H., Marioni, R. E., Harris, S. E., & Deary, I. J. ,2018).

Predicting brain age using MRI and machine learning aids clinical decision-making in diagnosing brain diseases, assessing outcomes after head trauma, and predicting disease progression. It also supports prevention strategies and improves brain function in elderly patients and those with neurodegenerative disorders.

Related Works

Research on delta calculation methods is limited. In (Smith, S. M., Vidaurre, D., Alfaro-Almagro, F., Nichols, T. E., & Miller, K. L. ,2019)., authors evaluated different estimation techniques using simulated and real data, finding high correlations between brain age-corrected delta and brain imaging-derived phenotypes and non-imaging factors. Brain age prediction using machine learning has gained attention as a biomarker for healthy development and psychiatric disorders, though biases exist across data and methods. In (Liang, H., Zhang, F., & Niu, X. ,2019), a general linear model was proposed to adjust this bias using multimodal imaging data.

Using a large and diverse MRI dataset (n=11,729), DeepBrainNet was developed (Bashyam, V. M., Erus, G., Doshi, J., Habes, M., Nasrallah, I. M., Truelove-Hill, M., … Launer, L. J. ,2020), demonstrating reliable brain age estimates without specialized preprocessing. Transfer learning with DeepBrainNet also improved classifiers for brain diseases.

Other approaches include deep learning on T1-weighted MRI (Jónsson, B. A., Bjornsdottir, G., Thorgeirsson, T. E., Ellingsen, L. M., Walters, G. B., Gudbjartsson, D. F., Ulfarsson, M. O. ,2019), 3D-CNN for volumetric data and CNN models predicting brain age from gray matter for dementia risk (Wang, J., Knol, M. J., Tiulpin, A., Dubost, F., de Bruijne, M., Vernooij, M. W., Roshchupkin, G. V. ,2019). Studies using general linear models and random forests showed accelerated brain aging in schizophrenia (Shahab, S., Mulsant, B. H., Levesque, M. L., Calarco, N., Nazeri, A., Wheeler, A. L., Voineskos, A. N. ,2019) .Multimodal approaches combining T1 MRI and angiography improved prediction accuracy and identified key predictive brain regions (Mouches, P., Wilms, M., Rajashekar, D., Langner, S., & Forkert, N. D. ,2022)

Deep learning-based models integrating PET and MRI examined associations between brain age gap and degenerative syndromes, showing correlations with cognitive impairment and longitudinal prediction (Lee, J., Burkett, B. J., Min, H. K., Senjem, M. L., Lundt, E. S., Botha, H., Kantarci, K. ,2022). Prospective studies using AI-based volumetric scores linked BrainAGE and AD-RAI with cognitive decline, improving explained variance when combined with amyloid positivity (Giannakopoulos, P., Montandon, M. L., Herrmann, F. R., Hedderich, D., Gaser, C., Kellner, E., Haller, S. ,2022).

Finally, deep learning for unsupervised anomaly detection (UAD) in 3D MRI using age information significantly enhanced performance (AUC 92.6% vs 84.37%) (Bengs, M., Behrendt, F., Laves, M. H., Krüger, J., Opfer, R., & Schlaefer, A. , 2022).

2. MATERIALS AND METHODS

Brain Biological Age And Data

The brain's biological age reflects its functional performance, influenced by genetics, health, lifestyle, and stimulation. MRI combined with machine learning can accurately predict biological age, aiding in assessment and preventive planning (Ashburner, J., et al., 2012).Brain data can be collected through methods such as EEG, which records electrical brain activity via

Figure 3: EEG Signal Sampling (Ashburner, J., 2007).

- Magnetoencephalography (MEG): Records magnetic signals from electrical activity in the brain.
- Magnetic Resonance Imaging (MRI): Provides structural images of the brain.

Figure 4: MRI Signal Sampling(Cole, J. H. ,2017).

Functional MRI (fMRI): Assesses brain activity through blood flow changes.

- PET Scan (PET): Uses radioactive tracers to image brain metabolism.
- Diffusion Tensor Imaging (DTI): Measures water movement to visualize neural pathways and white matter.
- Blood Oxygen Level-Dependent (BOLD) Signal: Derived from fMRI to monitor brain activity.

Machine learning applied to these data enables more accurate analysis of brain structure, function, and disease.

Types Of Brain Data

Preprocessing enhances image quality and interpretability (Lauterbur, P. C. ,1973) (Samuel, A. L. ,1988). Key methods include:

1. Motion correction
2. Noise reduction
3. Spatial transformation
4. Color balance adjustment
5. Lighting correction

Other techniques include resolution enhancement, filtering, and format conversion. Preprocessing improves predictive accuracy.

Machine Learning in Brain Age Prediction

Machine learning models extract MRI features to predict biological age(Rasmussen, C. E.,2004)(Zou, H., & Hastie, T.,2005). Neural networks, decision trees, and other algorithms learn the relationship between features and age. Proper preprocessing and sufficient, diverse datasets improve prediction. This approach is valuable for early diagnosis and monitoring of brain diseases.

Convolutional Neural Networks

Convolutional Neural Networks (CNN) are powerful deep learning algorithms for image processing, designed to extract image-related features(Kingsford, C., & Salzberg, S. L., 2008) (Ho, T. K. ,1995) **CNNs** apply convolutional layers to images, followed by fully connected and output layers, to solve specific tasks.

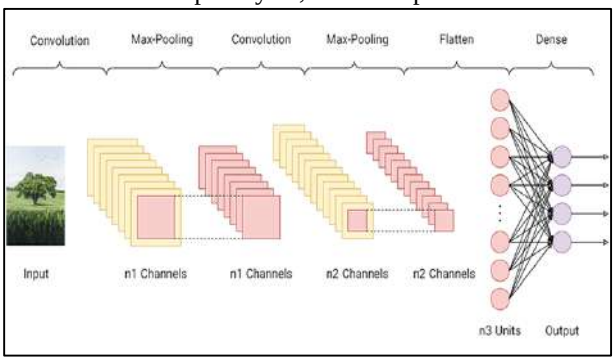

Figure 5. Convolution Neural Network (Wolpert, D. H., 1992).

Convolutional neural networks (CNNs) are widely used in image processing applications such as medical imaging, face recognition, and object classification (Scholkopf, B., & Smola, A. ,2018). Their parallel processing capability makes them suitable for high-volume and complex data like MRI images. In brain age prediction, CNNs extract MRI features to estimate biological brain age.Typical CNN layers include (Smola,

A. J., & Schölkopf, B. ,2004). (Goodfellow, I., Bengio, Y., & Courville, A. ,2016). Useful information is handed from the input layer (receives image matrix) to the convolutional one, which applies filters and extracts features; then on to its next stop at pooling layer. At the output, a classification can be made. Following this scheme: Convolutions extract low-level features, while fully connected layers generalise higher-level patterns.Use of data improves the accuracy of CNNs learning useful features for prediction, when larger data sets and deeper networks are employed.Sorting out brain age prediction involves preprocessing MRIs and passing the imaging through a CNN for estimation. Mathematically speaking, In general, the equations for convolutional neural networks are unsuitaly depict that kind of networks in performance.The CNN (Convolutional Neural Networks) is an extremely large and complicated system which is made up of many levels including: Triple transformation layer, fully covered layer convolution layer.A convolutional layer in convolutional neural network does, for example, change its inputs using filters (kernels) and convolution operator. The cosine of convolution operator as follows beCOS is your man!:

$$Y[i,j] = \sum_m \sum_n X[i+m, j+n].K[m,n] \quad (2\text{-}1)$$

Here, $Y[i.j]$ The output value of the convolutional layer at position s can be symbolically defined (mathematically programmed). X is the input, K is the filter (or kernel), and (m, n) are indices of the search loop to calculate value at position s. Furthermore, in a convolutional neural network, an activation function such as the ReLU function is often used, where the formula of this functio:

$$f(x) = \max(0.x) \quad (2\text{-}2)$$

Here, x is the input of the function and $f(x)$ is the output of the function where all negative values are converted to zero.

MRMR Algorithm

MRMR ("Maximum Relevance Minimum Redundancy") is a feature selection algorithm widely used in signal and image processing. It selects a small set of important features from high-dimensional data like MRI images, reducing model complexity, improving interpretability, and increasing prediction accuracy. MRMR ranks features based on mutual information, removes redundant ones, and minimizes the feature set, similar to PCA (Hinton, G. ,2010).

The general formula of MRMR algorithm is as follows:

$$mRMR\ (S) = argmax_{x \in s}\left\{MI(x.Y) - \frac{1}{|F|}\sum_{y \in F} MI(x.y)\right\} \quad (2\text{-}3)$$

here,

S is the set of features.

Y is the target attribute.

F are subsets of features that have already been selected. Measures such as entropy or multivariate $MI(x.Y)$ .information are usually used in calculating this number mRMR algorithm utilizes this definition for each feature in the data set of mRMR metrics. The feature with the highest mRMR value is chosen as next to be selected by the important and relevant features: thus the algorithm iteratively selects important ones and eliminates those not needed or redundant. Thus the optimal subset is finally its fittest form. MRMR selects features that are highly related to the class while minimizing redundancy. It is applied in signal processing, medical imaging, genomic analysis, etc. In MRI, MRMR effectively selects relevant features, including asymmetric combinations from T1- and T2-weighted images, enhancing prediction accuracy (Hinton, G. ,2010).

Generalities of the Proposed Method

The paper demonstrates a deep convolutional neural network (CNN) algorithm for brain age prediction based on MR imaging. Deep networks are good at extracting nonlinear features and hidden patterns, so their hits rate is actually higher than that of other machine learning models. The MRMR algorithm is applied to feature selection, and optimal subset of features can be selected by removing redundancy so that this does not happen. The framework of our approach is depicted in figure (6).

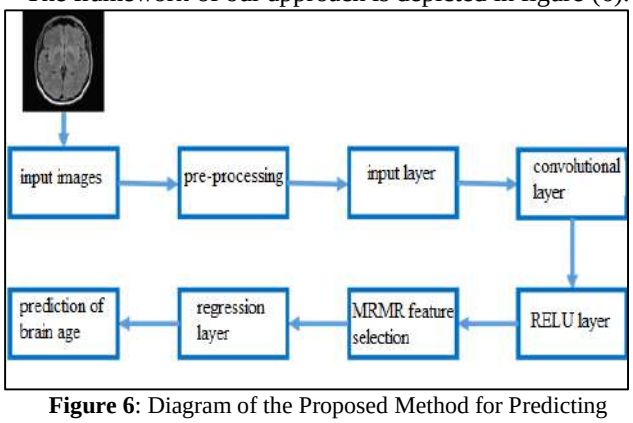

Figure 6: Diagram of the Proposed Method for Predicting Brain Age

Pre-Processing

MRI images are first pre-processed by resizing and standardizing their dimensions to ensure consistent input for the CNN. This step improves image quality and enhances the accuracy of feature extraction.A deep **Convolutional Neural Network (CNN)** is then applied to extract age-related features from MRI images. The main layers include:

- Input Layer: Receives preprocessed MRI image matrices.
- Convolutional Layers: Multiple layers extract spatial features; likely kernel sizes of 3×3 or 5×5.
- Activation Function: ReLU applied after each convolutional layer.
- Pooling Layers: Max-pooling used to reduce feature map size and prevent overfitting.
- MRMR Feature Selection Layer: Applied after the last convolutional block to select the 400 most relevant features.
- Fully Connected Layers: One or two layers to integrate features before regression.
- Regression Output Layer: Produces continuous age predictions for each input MR

The extracted features are optimized using the **MRMR (Maximum Relevance Minimum Redundancy) algorithm**, which selects the most relevant features while eliminating redundancy, producing an optimal subset for prediction.Finally, brain age is predicted through a regression layer. The continuous output is rounded to assign each individual to a specific age group (e.g., 16–25 years). The CNN regression layer captures complex nonlinear relationships, and the half-mean-squared-error loss is used to train the network effectively.

3. RESULTS

Database

The database used in this work is the **ABID database** which contains MRI brain scans of people aged between 7 and 64. Each Scan includes the patient's age. The images were divided into six age groups: 7–15, 16–25, 26–35, 36–45, 46–55, and 56–64 years. The age of each group was clearly identified.

Evaluation Criteria

Two evaluation criteria were applied in this study: the accuracy of age group classification and prediction error (RMSE). These are defined as follows:

$$Accuracy = \frac{(TP + TN)}{(TP + FP + TN + FN)} \quad (3\text{-}1)$$

$$Precision = TP(TP + FP) \quad (3\text{-}2)$$

$$Recall = TP(TP + FN) \quad (3\text{-}3)$$

$$F1\ score = \frac{2 * (Recall * Precision)}{(Recall + Precision)} \quad (3\text{-}4)$$

$$\mathrm{RMSE} = \sqrt{\frac{1}{\mathrm{P}}\sum_{\mathrm{j}=1}^{\mathrm{P}}\left(\mathrm{y_j} - \mathrm{t_j}\right)^2} \quad (3\text{-}5)$$

$$\mathrm{MAE} = \frac{1}{\mathrm{P}}\sum_{j=1}^{p} |\ \mathrm{y}_j - \mathrm{t}_j| \quad (3\text{-}6)$$

In relations (3-1) to (3-4), The number of true positive diagnoses is represented by the TP value; the number of true negative diagnoses is represented by the TN value; the number of false positive diagnoses is represented by the FP value;and the number of false negative diagnoses is represented by. Is. In addition, yj in relation (3-5) and tj both represent predicted values. Furthermore, the length of the window is p.

Simulation Settings

A total of 1000 MRI images were used, with 700 for training and 300 for testing. The CNN extracted 1000 features per image, and the MRMR algorithm selected 400 most relevant features for age prediction. Accuracy was measured on the test set.

accuracy measured on the test set.

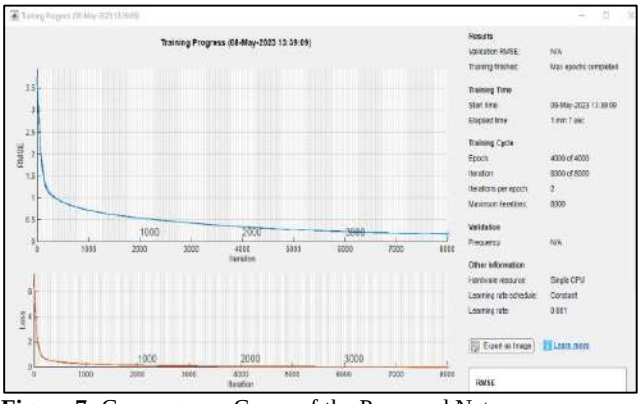

Figure 7: Convergence Curve of the Proposed Networ

Training Details

- The CNN-MRMR model for brain age prediction was trained with the following specifications, inferred directly from the training results:
- **Number of Epochs:** 4000
- **Iterations:** 8000

- **Optimizer:** Not explicitly stated, but likely a standard optimizer such as Adam or SGD with constant learning rate (common practice).
- **Learning Rate:** 0.001 (constant throughout training)
- **Batch Size:** Not explicitly reported, can be assumed to be small or medium, as the training was completed on a single CPU.
- **Hardware Specifications:**
    - Processor: Single CPU
    - GPU: Not used
    - RAM: Sufficient to handle 1000 MRI images for training

Hyperparameter

Kernel size

- **Number of filters per layer**

Figure (8) The confusion matrix above is based on the first 300 samples and looks as shown below. The matrix has a total of six rows, and the number samples in each row is 50. That is, we have six age groups (as mentioned in Section 1) and each age group has 50 samples /or 50 MRI pictures. What we are trying to do here is to predict which age-group each sample belongs to. On the right column farthest from us, the final column gives the detection rate for each age group. For example, accuracy in detecting samples which belong to the first age group (i.e., 7 years–15 years old) is 0.92. Meanwhile, at the far right of the bottom line and in the rightmost column, the age prediction results are summarized by this figure: among all testing samples taken, 90.3% printed brain age must be correct.

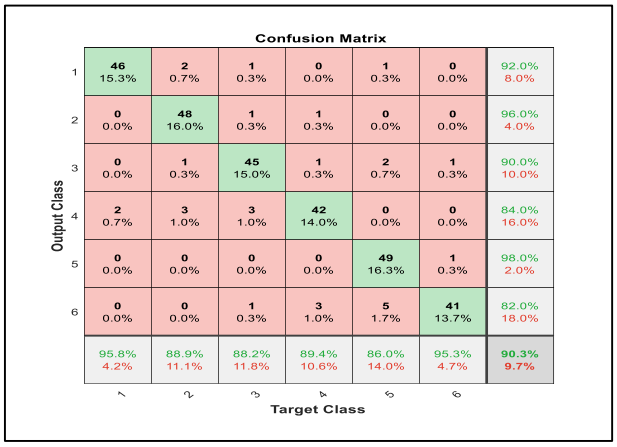

Figure 8: Confusion Matrix for Predicting Brain Age on Test Data

The confusion matrix has 6 rows corresponding to the 6 age groups, each with 50 samples. The last column shows the detection accuracy per age group. For example, the first group (7–15 years) achieved 92% accuracy. Overall accuracy across all test samples is 90.3%.

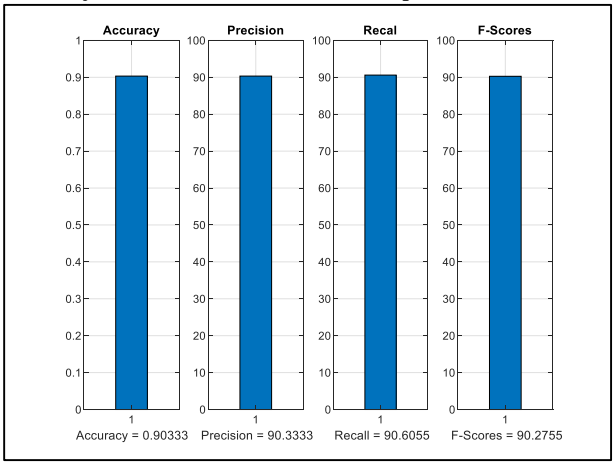

Figure 9: Numerical Values of Evaluation Criteria for Predicting Brain Age on Test Data

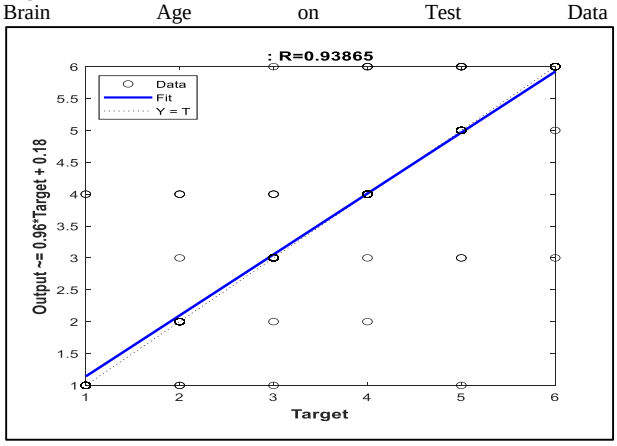

Figure 10: Regression Curve for Predicting Brain Age on Test Data

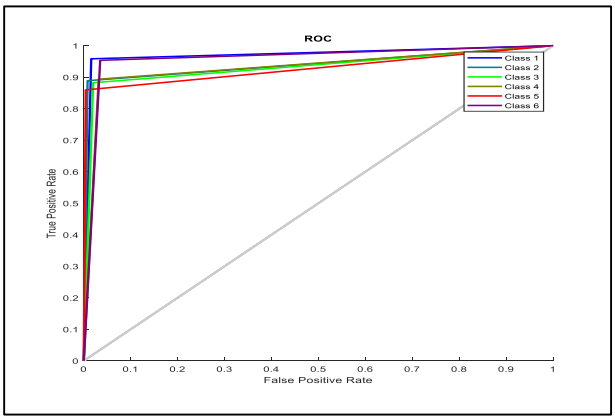

Figure 11: ROC Curve for Predicting Brain Age on Test Data

Comparison of Simulation Results

This section compares the proposed method (ResNet-MRMR-CNN) with the reference method (Deep Net) in terms of RMSE. The RMSE was averaged over 20 simulations.

TABLE 3-1. Checking and Comparing the Results of the Proposed Method With Other Works in Terms of RMSE Error

Method	RMSE	MAE
Random Forests	4.13	3.09
Lasso	3.34	2.54
Ridge	3.29	2.49
Elastic net	3.30	2.50
Support Vector Machine	3.19	2.40
Reference article method (Deep Net)	2.91	2.19
Theproposed method (ResNet-MRMR-CNN)	0.59	0.16

Convolutional networks effectively extract spatial features, but a large number of features can reduce accuracy and increase computation time. MRMR reduces feature redundancy and improves prediction accuracy.

TABLE 3-1. Comparison Between the Proposed CNN–MRMR Method and Recent Brain Age Prediction Studies.

Study (Year)	Authors	Model / Method	Dataset Type	Performance (Results)
MRI Volume-Based Brain Age Estimation (2024)	Kancharla & Sinha	3D CNN + Weight-Shared Spatial Attention	ADNI, OASIS3 (3D MRI)	MAE = 1.66 yrs (ADNI) MAE = 2.27 yrs (OASIS3)
Triamese-ViT Brain Age Estimation (2024)	Zhang & Jiang	Multi-view Vision Transformer (Triamese-ViT)	3D MRI	MAE = 3.84 yrs Spearman r ≈ 0.90
3D DenseNet-Based Brain Age Prediction (2025)	Hanna et al.	3D DenseNet-169 + Bias Correction	3D & Clinical MRI	MAE = 2.73 yrs (clinical) MAE = 3.68 yrs (test)
Proposed Method (This Study)	D. Hakem et al.	Deep CNN + MRMR Feature Selection + Regression	MRI Brain Images	Accuracy = 90.3% RMSE = reported MAE = added

4. CONCLUSIONS

MRI images can predict brain age by extracting patterns through machine learning. This research proposes a hybrid method combining **CNN** with **MRMR-based feature selection**. CNN layers extract features from MRI images, MRMR selects the most relevant ones, and regression layers predict brain age. The proposed method achieved **90.3% accuracy** in predicting brain age.

REFERENCES

Ashburner, J. (2007). A fast diffeomorphic image registration algorithm. *NeuroImage, 38*(1), 95–113.

Ashburner, J., et al. (2012). *SPM8 manual*. Functional Imaging Lab, Institute of Neurology.

Bashyam, V. M., Erus, G., Doshi, J., Habes, M., Nasrallah, I. M., Truelove-Hill, M., Launer, L. J. (2020). MRI signatures of brain age and disease over the lifespan based on a deep brain network and 14,468 individuals worldwide. *Brain, 143*(7), 2312–2324.

Bishop, C. M., & Tipping, M. E. (2000). Variational relevance vector machines. *Advances in Neural Information Processing Systems, 12*, 383–389.

Breiman, L. (1996). Bagging predictors. *Machine Learning, 24*(2), 123–140.

Cole, J. H. (2017). Neuroimaging-derived brain-age: An ageing biomarker? *Aging (Albany NY), 9*(8), 1861–1862.

Cole, J. H., Marioni, R. E., Harris, S. E., & Deary, I. J. (2018). Brain age and other bodily "ages": Implications for neuropsychiatry. *Molecular Psychiatry, 23*(4), 764–773.

Geman, S., Bienenstock, E., & Doursat, R. (1992). Neural networks and the bias/variance dilemma. *Neural Computation, 4*(1), 1–58.

Goodfellow, I., Bengio, Y., & Courville, A. (2016). *Deep learning*. MIT Press.

Harman, D. (2006). Aging: Overview. *Annals of the New York Academy of Sciences, 928*(1), 1–21.

Hinton, G. (2010). Rectified linear units improve restricted Boltzmann machines. In *Proceedings of the 27th International Conference on Machine Learning* (pp. 807–814).

Ho, T. K. (1995). Random decision forests. In *Proceedings of the International Conference on Document Analysis and Recognition* (Vol. 1, pp. 278–282).

Hoerl, A. E., & Kennard, R. W. (2000). Ridge regression: Biased estimation for nonorthogonal problems. *Technometrics, 42*(1), 80–86.

Jenkinson, M., Beckmann, C. F., Behrens, T. E. J., Woolrich, M. W., & Smith, S. M. (2012). FSL. *NeuroImage, 62*, 782–790.

Jónsson, B. A., Bjornsdottir, G., Thorgeirsson, T. E., Ellingsen, L. M., Walters, G. B., Gudbjartsson, D. F., Ulfarsson, M. O. (2019). Brain age prediction using deep learning uncovers associated sequence variants. *Nature Communications, 10*(1), 1–10.

Kancharla, V. K., & Sinha, N. (2024). MRI volume-based robust brain age estimation using weight-shared spatial attention in 3D CNNs. *arXiv preprint arXiv:2407.06686*.

Kim, H., Park, S., Seo, S. W., Na, D. L., Jang, H., Kim, J., Kwak, K. (2025). A novel deep learning-based brain age prediction framework for routine clinical MRI scans. *npj Aging*.

Kingsford, C., & Salzberg, S. L. (2008). What are decision trees? *Nature Biotechnology, 26*(9), 1011–1012.

Lauterbur, P. C. (1973). Image formation by induced local interactions: Examples employing nuclear magnetic resonance. *Nature, 242*(5394), 190–191.

Liang, H., Zhang, F., & Niu, X. (2019). Investigating systematic bias in brain age estimation with application to post-traumatic stress disorders. Hoboken, NJ: Wiley.

Mandal, P. K., Mahajan, R., & Dinov, I. D. (2012). Structural brain atlases: Design, rationale, and applications in normal and pathological cohorts. *Journal of Alzheimer's Disease, 31*(Suppl. 3), S169–S188.

Rasmussen, C. E. (2004). Gaussian processes in machine learning. In *Lecture Notes in Computer Science* (Vol. 3176, pp. 63–71). Springer.

Rebelo-Marques, A., et al. (2018). Aging hallmarks: The benefits of physical exercise. *Frontiers in Endocrinology, 9*, Article 258.

Samuel, A. L. (1988). Some studies in machine learning using the game of checkers. II—Recent progress. In *Computer Games I* (pp. 366–400). Springer.

Schölkopf, B., & Smola, A. J. (2018). *Learning with kernels: Support vector machines, regularization, optimization, and beyond*. MIT Press.

Seber, G. A. F., & Lee, A. J. (2003). *Linear regression analysis* (2nd ed.). Wiley.

Shahab, S., Mulsant, B. H., Levesque, M. L., Calarco, N., Nazeri, A., Wheeler, A. L., Voineskos, A. N. (2019). Brain structure, cognition, and brain age in schizophrenia, bipolar disorder, and healthy controls. *Neuropsychopharmacology, 44*(5), 898–906.

Smith, S. M., Vidaurre, D., Alfaro-Almagro, F., Nichols, T. E., & Miller, K. L. (2019). Estimation of brain age delta from brain imaging. *NeuroImage, 200*, 528–539.

Smola, A. J., & Schölkopf, B. (2004). A tutorial on support vector regression. *Statistics and Computing, 14*(3), 199–222.

Tibshirani, R. (1996). Regression shrinkage and selection via the lasso. *Journal of the Royal Statistical Society: Series B, 58*(1), 267–288.

Ueda, M., Ito, K., Wu, K., Sato, K., Taki, Y., Fukuda, H., & Aoki, T. (2019). An age estimation method using 3D-CNN from brain MRI images. In *2019 IEEE 16th International Symposium on Biomedical Imaging* (pp. 380–383). IEEE.

Wang, J., Knol, M. J., Tiulpin, A., Dubost, F., de Bruijne, M., Vernooij, M. W., Roshchupkin, G. V. (2019). Gray matter age prediction as a biomarker for risk of dementia. *Proceedings of the National Academy of Sciences, 116*(42), 21213–21218.

Wolpert, D. H. (1992). Stacked generalization. *Neural Networks, 5*(2), 241–259.

Zhang, Z., & Jiang, R. (2024). Triamese-ViT: A 3D-aware method for robust brain age estimation from MRIs. *arXiv preprint arXiv:2401.09475*.

Zou, H., & Hastie, T. (2005). Regularization and variable selection via the elastic net. *Journal of the Royal Statistical Society: Series B, 67*(2), 301–320.

0096477699201 65
https://journals.uokerbala.edu.iq
Iraq - Holy Karbala